FLORIDA STATE UNIVERSITY

FAMU-FSU COLLEGE OF ENGINEERING

VISUALIZATION STUDY OF THERMAL COUNTERFLOW TURBULENCE

IN SUPERFLUID ^{4}HE

By

JIAN GAO

A Dissertation submitted to the
Department of Mechanical Engineering
in partial fulfillment of the
requirements for the degree of
Doctor of Philosophy

2017

Jian Gao defended this dissertation on April 28, 2017.
The members of the supervisory committee were:

Wei Guo
Professor Directing Dissertation

Hui Li
University Representative

Emmanuel G. Collins
Committee Member

Kunihiko Taira
Committee Member

Sastry V. Pamidi
Committee Member

The Graduate School has verified and approved the above-named committee members, and certifies that the dissertation has been approved in accordance with university requirements.

To my parents, Hua Gao and Yuying Zhu
And
My wife Jingjing Lu

ACKNOWLEDGMENTS

First, I would like to express my sincere gratitude to my advisor, Dr. Wei Guo for accepting me as a graduate student in his group, for teaching me everything about the laser and cryogenics systems, and for supervising my doctoral research.

I would like to thank my dissertation committee members- Dr. Hui Li, Dr. Emmanuel G. Collins, Dr. Kunihiko Taira and Dr. Sastry V. Pamidi for their valuable guidance and comments on my prospectus and thesis.

I am also very grateful to Dr. Steven Van Sciver for allowing me to conduct experiments in his lab and providing cryogenics equipment. Special thanks to Dr. Daniel Mckinsey for providing laser equipment. Many thanks for a lot of support and valuable discussions from Dr. William Frank Vinen. Many thanks to Dr. Alexander Marakov for assisting with experimental setup and testing the equipment during the early days of this experiment. Enormous thanks to Emil Varga for helping build and test the grid towing system.

I would also like to thank the past and present Cryolab members- Dr. Ernesto Bosque, Dr. Mark Vanderlaan, Dr. Ram C. Dhuley, Joseph A. Hurd, Brian Mastracci, Andrew Wray, Jacob Ross, Hamid Sanavandi, Nathaniel Garceau and Daniel Tamayo for sharing their valuable cryogenics knowledge and their friendship.

None of these could happen without the endless love and support of my parents, my wife and my little brother, who believe in me and support me for all the time. Xiexie.

TABLE OF CONTENTS

LIST OF FIGURES

xi

ABSTRACT

Superfluid ^{4}He (He II) has been widely used as a coolant material in many engineering applications. Its unique heat transfer mode is the so-called thermal counterflow. The study of thermal counterflow will contribute to the design of He II based cooling devices and our understanding of quantum turbulence. However, due to the lack of effective visualization and velocimetry techniques, studying the fluid dynamics in superfluid ^{4}He is very challenging. In this dissertation, we discussed the development of a novel flow-visualization technique in He II based on the generation and imaging of thin lines of metastable He_2^* tracer molecules. These molecular tracers are created via femtosecond-laser field-ionization of helium atoms and can be imaged using a laser-induced fluorescence technique. In steady state thermal counterflow measurement, we demonstrated that such tracer molecules are entrained by the normal fluid component. We revealed for the first time a laminar to turbulent transition in the normal fluid component. We found that the profile of the normal fluid in the laminar flow can exhibit quite different velocity profile compared to the laminar Poiseuille profile of classical fluid in a channel. In the turbulent flow state, the turbulence intensity is found to be much higher than that in classical channel flow. This turbulence intensity appears to depend primarily on temperature. We also found that the form of the second order transverse structure function deviates more strongly from that found in classical turbulence as the steady state heat flux increases, suggesting novel energy spectrum. In decaying counterflow turbulence, we studied the normal fluid flow via flow visualization and measured the quantized vortex line density using 2nd sound attenuation. Comparing the decay behavior of both fluids, we were able to produce a theoretical model to explain the puzzling decay behavior of the vortices. We were also able to determine the effective kinematic viscosity in a wide temperature range. Some preliminary results in the study of decaying grid turbulence were obtained, which allows us to examine the intermittent behavior of superfluid turbulence.

CHAPTER 1

INTRODUCTION

This chapter introduces some interesting properties of liquid helium-4 and defines the scope and organization of the dissertation.

1.1 Introduction of liquid helium-4

1.1.1 Liquid helium

Helium was first liquefied by Kamerlingh Onnes at the University of Leiden in the Netherlands in 1908 [1]. Twenty years later, Onnes's student, Willem Keesom, discovered two different states of liquid helium: He I, above the so-called λ transition ($T_\lambda = 2.178\ K$), and He-II, below the λ transition (more details will be presented later). Onnes discovered that He II can flow through tiny pores [2]. Subsequently, Mclennan, Smith, and Wihelm, based on light scattering studies of liquid helium, found that liquid helium ceased boiling below the λ transition [3]. A series of experiments conducted by Keesom suggested that the thermal conductivity of He II was 3 million times higher than that of He I. These strange behaviors of He II led to Fritz London's idea of Bose-Einstein condensation [4], which Laszlo Tisza and Lev Landau then extended [5,6]. Although liquid helium-4 has been studied for more than 100 years, understanding it still remains an active field that requires more investigation.

Liquid helium has several unique features that are shown in the p-T phase diagram in Figure1.1 [7]. Unlike all other substances, helium-4 remains in the liquid phase at temperatures down to zero Kelvin. Its solid phase exists only with an externally-applied pressure of about 25 bars or higher. Another interesting feature of helium is that it does not have a triple point of coexistence among gas, liquid and solid. Its critical point occurs at $P_c = 0.22\ MPa$, a point which is much easier to obtain for helium than for any other fluids. Besides the gas phase and the normal liquid phase (He I), when helium-4 is cooled to below the λ transition temperature along its saturated vapor pressure curve, it undergoes a phase transition to a superfluid phase (He II). He I is a classical Navier-Stokes viscous fluid. He II, on the other hand, is a quantum fluid, the motion
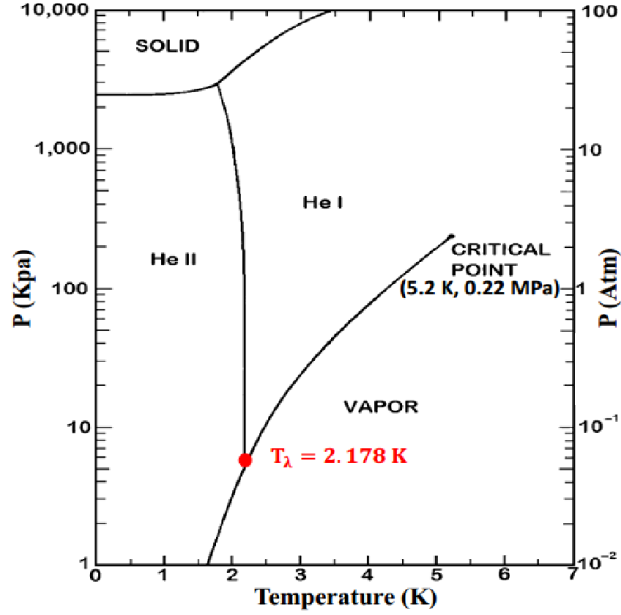
Figure 1.1 Helium-4 p-T phase diagram.

of which is governed by quantum physics. Due to its well-known, extremely high thermal conductivity, He II has been used widely as a coolant material in many large-scale superconducting magnets and infrared detectors [8]. For instance, 120 tons of helium are used to cool the magnets in a Large Hadron Collider at 1.9 K so that its niobium-titanium coils can achieve a superconducting state. Hence, studying the heat transport properties of He II is very important for the design of such large-scale cooling system.

1.1.2 Two fluid model

Based on a two-fluid model [9], He II can be considered as consisting of two interpenetrating fluid components: 1) the normal fluid component, which includes the thermal excitations and which can be regarded as a viscous fluid carrying the entire entropy content of the liquid and 2) the superfluid component, which is inviscid and has no entropy ($S = 0$). The total density (ρ) of He II is the sum of the superfluid density (ρ_s) and the normal fluid density (ρ_n),

$$\rho = \rho_s + \rho_n.$$ (1.1)

The total density of He II depends only weakly on the temperature, but the normal fluid fraction is strongly temperature dependent:

2
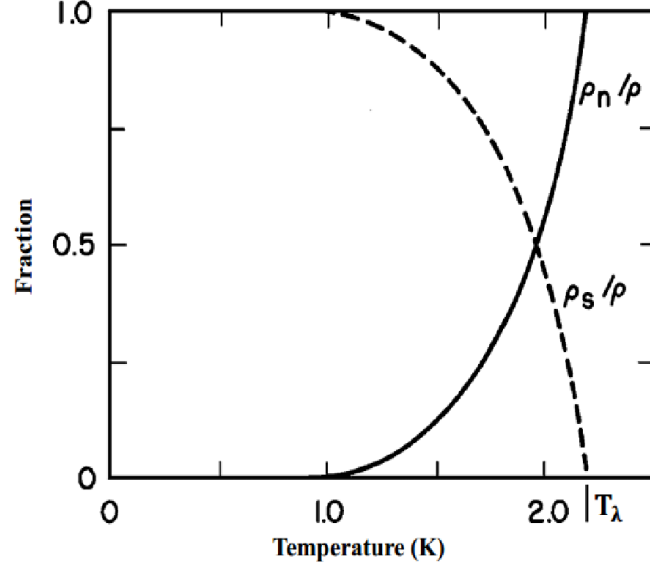
Figure 1.2 The fraction of the normal fluid drops from unity to zero as its temperature decreases from T_λ to zero.

$$\frac{\rho_n}{\rho} = \left(\frac{T}{T_\lambda}\right)^{5.6} \quad \text{for } T \leq T_\lambda. \tag{1.2}$$

According to the two-fluid model, the motion of He II can be represented by two fluid components separately. In terms of the gradient of the chemical potential g, the equation of the motion for the superfluid component is given by,

$$\frac{\partial \vec{v_s}}{\partial t} = -\nabla g = s\nabla T - \frac{1}{\rho}\nabla p. \tag{1.3}$$

On the other hand, the Navier-Stokes equation can describe the momentum equation for He II:

$$\frac{\partial \vec{j}}{\partial t} = -\nabla p + \mu\nabla^2 v, \tag{1.4}$$

where the momentum density of He II is $\vec{j} = \rho_s\vec{v_s} + \rho_n\vec{v_n}$. Since the superfluid component has no viscosity, we can rewrite equation (1.4) as follows:

$$\rho_s\frac{\partial \vec{v_s}}{\partial t} + \rho_n\frac{\partial \vec{v_n}}{\partial t} = -\nabla p + \mu_n\nabla^2 \vec{v_n}. \tag{1.5}$$

Combining the motion of the superfluid component shown in equation (1.3), one can derive the momentum equation for the normal fluid component:

3

$$\rho_n \frac{\partial \vec{v_n}}{\partial t} = -\rho_s s \nabla T - \frac{\rho_n}{\rho} \nabla p + \mu_n \nabla^2 \vec{v_n}. \tag{1.6}$$

Furthermore, due to its two-fluid nature, He-II possesses more than one sound wave model: the first sound and the second sound. The first sound is a wave model in which the two fluids move in phase, which results in pressure and density oscillations in He II similar to normal sound waves moving through air. The second sound presents as a wave model in which the two fluids move completely out of phase. Since the two fluids flow in opposite directions, regions in which the local density of the normal fluid is higher have a higher temperature and entropy. Therefore, second sound waves can result in temperature and entropy oscillations in He II. Based on equation (1.3) - (1.6), we can derive the expressions for the speed of the first sound (c_1) and the second sound (c_2) by eliminating v_n and v_s, and dropping the higher order terms:

$$c_1^2 = (\frac{\partial p}{\partial \rho})_s \text{ and } c_2^2 = \frac{s^2 \rho_s}{\rho_n} (\frac{\partial T}{\partial s})_\rho. \tag{1.7}$$

In Figure 1.3, the dependence of the first sound and the second sound velocities on temperature is shown. The speed of the second sound is around 20 m/s in the temperature range 1 K to 2 K, about an order of magnitude smaller than that of the first sound.
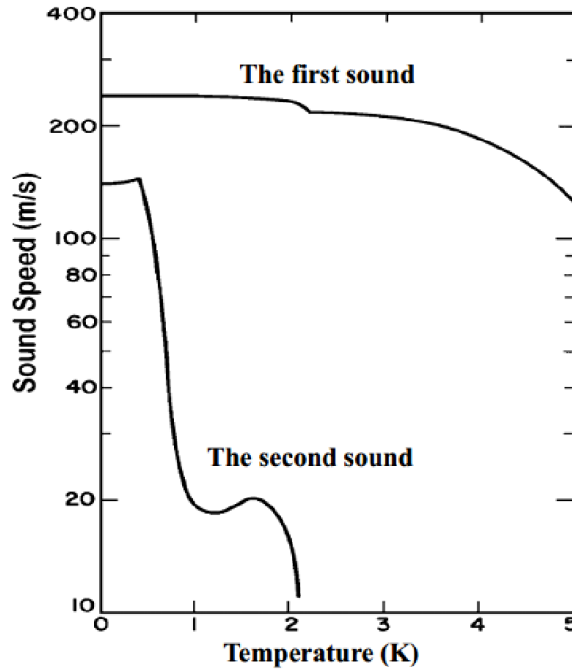
Figure 1.3 The speeds of two sound waves in helium-4.

4

1.1.3 Quantum Turbulence

In the two-fluid model, the superfluid component is assumed to be inviscid. This assumption leads to the conclusion that the superfluid velocity field must be irrotational—that is, $\nabla \times \vec{v}_s = 0$. However, in 1950, Osborne measured the vertical height of a single rotating bucket of He II and concluded that He II behaves as a viscous fluid in a rotating bucket [10]. To resolve the contradiction between the experiment and the two-fluid model, an array of vortex lines has been introduced in rotating He II [10,11]. The circulation of each vortex core (radius ~ 1 Å) is quantized and not arbitrary, as it is in classical fluids. Further, the circulation Γ along closed path L in He II is defined as

$$\Gamma = \oint \vec{v}_s d\vec{l} = n \frac{h}{m} = n\kappa ,$$
(1.8)

where n is an integer, h is Planck's constant, m is the mass of a helium atom, and κ is the circulation quantum. Each vortex line carries a single of quantum of circulation ($n = 1$). The existence of quantized circulation was first observed by Vinen [12]. One can image that the superfluid component circulates around an angstrom-sized hole. In case of one straight singly vortex line, the superfluid velocity can be shown as

$$v_s = \frac{\kappa}{2\pi r} ,$$
(1.9)

where r represents radius distance from the core.

1.1.4 Mutual friction

Early studies by Vinen demonstrated that when the superfluid velocity exceeds a critical velocity v_{sc}, turbulence appears spontaneously in the superfluid component as a tangle of quantized vortices [13]. A mutual friction between the two fluids then arises through the interaction between the quantized vortices and the normal fluid. Based on a dimensional analysis, the force per unit length of the vortex line would be as follows:

$$\vec{f} = \frac{\rho_s \rho_n}{\rho^2} \mu_n \left| \vec{v}_n - \vec{v}_s \right| .$$
(1.10)

The term, vortex line density, represented by L, is normally used to characterize the length of quantized vortices per unit volume. Therefore, one expects that the total mutual friction force per unit volume of He II will be

$$\vec{F}_{ns} = L\vec{f} = \frac{\rho_s \rho_n}{\rho^2} \mu_n \left| \vec{v}_n - \vec{v}_s \right| L \,. \tag{1.11}$$

Taking into account the quantized vortices via additional mutual friction force, and assuming the incompressible flow of two fluid components, one can modify the two-fluid hydrodynamic equations (1.5) and (1.6), which are

$$\rho_s \frac{\partial \vec{v}_s}{\partial t} = \rho_s s \nabla T - \frac{\rho_s}{\rho} \nabla p - \frac{\rho_s \rho_n}{\rho^2} \mu_n \left| \vec{v}_n - \vec{v}_s \right| L \,, \tag{1.12}$$

$$\rho_n \frac{\partial \vec{v}_n}{\partial t} = -\rho_s s \nabla T - \frac{\rho_n}{\rho} \nabla p + \mu_n \nabla^2 \vec{v}_n + \frac{\rho_s \rho_n}{\rho^2} \mu_n \left| \vec{v}_n - \vec{v}_s \right| L \,. \tag{1.13}$$

1.1.5 Heat transfer in He II

Another unique property of He-II is that its heat transfer occurs via so-called thermal counterflow instead of via classical convection. When a heat current is applied in the closed end of a flow channel, as shown in Figure 1.3, the normal fluid carries the heat away from the heat source and a counterflowing superfluid serves to eliminate the net mass flow. Landau [14] related the heat flux, q, to the normal fluid velocity, v_n, with the following equation:

$$q = \rho s T v_n \,. \tag{1.14}$$

For instance, consider a steady state heat transfer problem in a flow channel with a hydraulic diameter of d. If the applied heat flux q is less than the critical heat flux q_c, there would be no vortices in the flow. Equation (1.5) and equation (1.6) can be simplified to the Poiseuille equation,

$$\frac{dp}{dx} = \rho s \frac{dT}{dx} = -\frac{\beta \mu_n \vec{v}_n}{d^2} \,, \tag{1.15}$$

where x is along the channel axis and β is a geometrical constant. Eliminating the v_n based on the thermal counterflow equation (1.14), we can solve the heat transfer problem in a steady state, which yields

$$\frac{dT}{dx} = -\frac{\beta \mu_n q}{d^2 (\rho s)^2 T} \quad (q < q_c) \,. \tag{1.16}$$

This heat transfer mode, which is much more efficient than classical convection, can lead to an effective thermal conductivity higher than that of any other materials. However, the superfluid component can become turbulent, which limits the heat and mass transfer properties of He II.
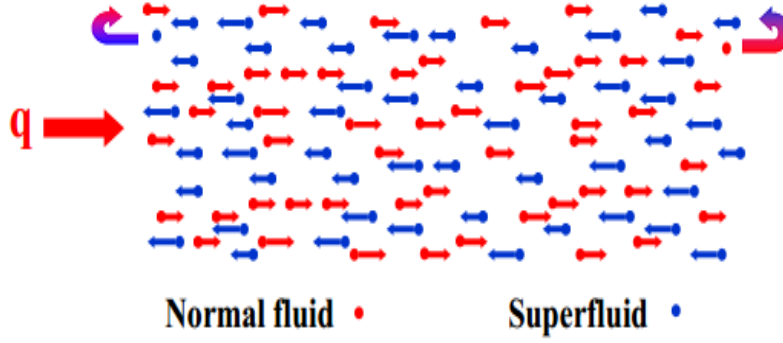
Figure 1.4 A schematic showing He II thermal counterflow.

In the early 1950s, Vinen has proposed a phenomenological model to describe variations of the vortex line density in the thermal counterflow [12]. Assuming that the vortex tangle is random and homogeneous, Vinen's model states,

$$\frac{dL}{dt} = \left(\frac{dL}{dt}\right)_{gen} - \left(\frac{dL}{dt}\right)_{decay} = \frac{\rho_n B}{2\rho}\chi_1 v_{ns}L^{3/2} - \frac{\kappa}{2\pi}\chi_2 L^2 . \tag{1.17}$$

Here, $v_{ns} = |v_n - v_s|$ is the counterflow velocity, κ is the quantum circulation, and χ_1, χ_2 and B are temperature dependent and can be determined experimentally. Equation (1.17) can yield the following steady state vortex line density:

$$L = \alpha(T)(\frac{\rho_n}{\rho}\vec{v}_{ns})^2 . \tag{1.18}$$

In this equation, $\alpha(T)$ is a function of temperature. Assuming that the normal fluid flow is laminar and that quantized vortices occur in the flow channel, one-dimensional heat conductivity problems can be solved based on equation (1.12), (1.13), (1.14), and (1.18) with the formula,

$$\frac{dT}{dx} = -\frac{\beta \mu_n q}{d^2(\rho s)^2 T} - \frac{A_{GM}\rho_n}{\rho_s^3 s^4 T^3}q^3 \ (q > q_c), \tag{1.17}$$

where $A_{GM} \approx \frac{\rho_n^2}{\rho^3}$ is the experimentally-estimated Gorter-Mellink mutual friction coefficient. Here, the mutual friction between the resulting quantized vortices in the superfluid and the normal fluid states leads to an additional term that is proportional to q^3.

1.2 Motivation

Normally, engineers use Equation (1.16) and Equation (1.19) to estimate the heat flux in He-II based on a measured temperature gradient. However, this provides information only about the mean heat flux. The derivation of these equations assumes that the normal-fluid flow is always laminar and that there are no fluctuations in the velocity field. In reality, like the turbulence in the superfluid, the normal fluid can also become turbulent, as revealed in recent experiments [15]. Turbulent normal fluid in the thermal counterflow will lead to temporal and spatial fluctuations of the temperature and the local heat flux. A careful characterization of these fluctuations could be vitally important for systems that require high thermal stability. In addition, He II has a very small kinematic viscosity, which allows the generation of flows with extremely high Reynolds numbers that can barely be achieved with other conventional fluid materials [16]. Thus, a reliable determination of the effective kinematic viscosity is needed in many high-Reynolds-number turbulence experiments that use He II as the testing fluid.

Besides its practical application in engineering, studying the hydro-dynamics of He II is important in fundamental science. Although the normal fluid behaves like a classical viscous fluid, its turbulence in the counterflow cannot be characterized using existing knowledge obtained from classical fluids. This is because, due to the mutual friction between the two fluid components, dissipation occurs at all length scales in the normal fluid, in contrast to classical turbulence, where dissipation takes place only below a small length scale called the Kolmogorov length scale [14]. Moreover, turbulence in the superfluid takes the form of a tangle of quantized vortices, a phenomenon normally called quantum turbulence [17,18]. The coupling and de-coupling between quantum turbulence and classical turbulence in the normal fluid has been subject to a detailed investigation [17]. As a consequence, conducting fluid research in He II will broad our understanding of turbulence in general and contribute to the theoretical study of quantum turbulence.

1.3 Challenges of fluid research in He II

Despite the great potential of He II as a working fluid, the lack of quantitative flow measurement tools has hampered its application in both engineering and fundamental science. Normally, for common test fluids, researchers use Pitot tube pressure measurements and hot-wire

anemometry. However, in He II, the motion of both fluid components can contribute to the sensor response, which leads to difficulty in the data analysis. One powerful method to study fluid dynamics is direct flow visualization. However, visualizing flows in He II is still very challenging, in part due to helium's extremely low temperature and density [19]. In the past, efforts have been made to visualize fluid dynamics in superfluid helium by using microscopic tracers. For instance, researchers have tried neutron absorption tomography using ^3He particles [20] and acoustic cavitation imaging with electron bubbles [21]. Since Stokes drag dominates other forces, these microscopic particles are expected to follow the motion of the normal fluid component. However, the neutron absorption tomography method, due to its need to raster the neutron beam through the experimental volume, has limited spatial resolution due to a finely-collimated neutron beam and time resolution. Acoustic cavitation imaging requires the generation of strong ultrasonic sound waves that can cause disturbances to the flow.

Recently, particle image velocimetry (PIV) and particle tracking velocimetry (PTV) using micron-sized solidified particles (hydrogen or deuterium) as tracers have been developed and applied to the study of flows in He II [22,28]. An early PIV technique has been applied to the study of the thermal counterflow in He II with measurements showing a significant discrepancy between the measured particle velocity and the theoretical normal fluid velocity [23]. Later, using the PTV technique, Paoletti et al. observed that, at relatively low velocity, the tracer particles can be trapped by the quantized vortices while also moving with the normal fluid via Stokes drag [25]. Their experiments provide a direct confirmation of the two-fluid mode. More recently, Chagovets and Van Sciver [26] studied thermal counterflow using the PTV technique and showed that, below some transition velocities, particles are trapped on individual vortex lines. Above the transition velocity, the trapped particles are dislodged from the vortex core and follow the direction of the normal fluid with a lower velocity. Since such micron-sized particles interact with both fluid components, making it difficult to quantify clear information on the behavior of the individual fluid components, developing a more advanced flow visualization technique in He II is urgent. For this study, our new tracer candidate was metastable He_2^* triplet molecules, the properties of which will be discussed in Chapter 2.

1.4 Scope and organization of the dissertation

Three research objectives were achieved in this project. First, a novel tracer-line tracking technique based on the use of thin lines of metastable He_2^* molecules was developed [29]. Second, this flow visualization technique was applied to study the steady state thermal counterflow at five different bath temperatures: 1.45, 1.65, 1.85, 2.0, and 2.1 K [30]. Systematic measurements of the mean normal fluid velocity, turbulence intensity, and structure functions were conducted. Studying the novel form of turbulence in thermal counterflow [31] with the aid of flow visualization in He II can contribute to our theoretical understanding of turbulence in general. Finally, the precise values of an effective kinematic viscosity in decaying counterflow turbulence have been determined at 1.35, 1.45, 1.55, 1.65, 1.735 and 1.85 K [32]. This is of fundamental importance to understanding the dissipation mechanism in He II [33] and is beneficial to many high Reynolds number turbulence experiments and model tests that use He II as the working fluid.

This dissertation comprises seven chapters. Chapter 2 introduces the flow visualization technique based on the generation and imaging of thin lines of metastable He_2^* tracer molecules and the 2nd sound attenuation technique commonly used to measure vortex line density. That chapter includes detailed information about the experimental setup and data analysis method. Chapter 3 presents the experimental results of steady state thermal counterflow measurement, in which the laminar to turbulent transition in the normal fluid component is observed. The heat flux- and temperature-dependence of the mean normal fluid velocity and its turbulence intensity across the channel are measured. We find the structure functions in the normal fluid turbulence differ significantly from that in classical fluid turbulence, indicating a novel form of turbulence. The experimental observations of both second sound attenuation and flow visualization measurements in decaying counterflow turbulence are reported in Chapter 4. A new theoretical model is developed to explain the complex vortex line density decay behavior. In Chapter 5, a reliable determination of the effective kinematic viscosity for the decay of counterflow turbulence in He II is reported. Chapter 6 discusses some preliminary results of grid-generated turbulence in He II. Chapter 7 concludes the present work and proposes suggestions for future experiments.

The content of Chapter 2 has been peer reviewed and published in Review of Scientific Instruments. The results of Chapter 3 have been peer reviewed and published in Physical Review B and Journal of Low Temperature Physics. Sections of Chapter 4 have been peer reviewed and

published in Journal of Experimental and Theoretical Physics Letters. The results of Chapter 5 have been peer reviewed and published in Physical Review B. The proposed future work of Chapter 7 has been peer reviewed and published in Review of Scientific Instruments.

CHAPTER 2

EXPERIMENTAL METHODS

This chapter introduces the experimental method in detail. In Section 2.1, the properties of our tracer molecules are discussed. Section 2.2 presents the experimental equipment and setup including the tracer line imaging experiment and the 2nd sound measurement. Section 2.3 focuses on the method of data analysis.

2.1 Properties of metastable helium triplet molecules

Metastable He_2^* molecules can be created in helium as a result of ionization or the excitation of ground-state helium atoms [34,35]:

$$He^+ + e^- + He \rightarrow He_2^* \text{ and } He^* + He \rightarrow He_2^*. \tag{2.1}$$
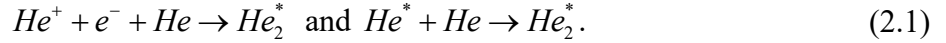
In this equation, "*" denotes the excited electronic state, and there is no need to seed the fluid with foreign particles. Depending on the total electron spins, these excited He_2^* molecules can be in either spin singlet states or triplet states. As these molecules quench from higher excited electronic states to their singlet ground states ($A^1 \Sigma_u^+$) and triplet ground states ($a^3 \Sigma_u^+$), visible scintillation photons are emitted [36]. The singlet molecules $A^1 \Sigma_u^+$ then radiatively decay in a few nanoseconds [37]; however, because a radiative transition to the ground state of two free helium atoms requires a strongly forbidden spin flip, the triplet state molecules $a^3 \Sigma_u^+$ are metastable. The radiative lifetime of He_2^* triplet molecules has been measured to be about 13s [38]. In liquid helium, He_2^* molecules form little bubbles with radii of about 6 Å [39], which leads to an extremely short viscous relaxation time. The viscous relaxation time τ is defined as how quickly the molecule adjusts its motion to the viscous flow, which has the following expression [40]:

$$\tau = \frac{2\left(\rho_m + \dfrac{\rho}{2}\right)a_m^2}{9\mu_n}. \tag{2.2}$$

Here, ρ_m is the density of the tracer molecule and a_m is the radius of the molecule. For instance, at 1.65 K in superfluid helium, the viscous relaxation time is only 4.5 ps. Due to their tremendously short viscous relaxation time, the excited molecules are completely entrained by the normal fluid and therefore are ideal tracers of the normal fluid flow. It has been found that, at sufficient low temperature when the normal fluid is effectively absent, the He_2^* molecules can bind to quantized vortices, which allows direct visualization of quantized vortices [41]. In our experiment, we focus on the two-fluid regime (i.e. above 1 K) where the He_2^* tracers track only the normal fluid.

In order to image the He_2^* molecules, a cycling-transition laser-induced fluorescence (LIF) technique has been developed [42,43]. A schematic diagram of the optical transitions of the He_2^* molecules is shown in Figure 2.1. These molecules can be excited by two infrared photons at 905 nm from their triplet ground state $a^3\Sigma_u^+$ to the excited electronic state $d^3\Sigma_u^+$. Over 90% of the molecules in the d state decay to the $b^3\Pi_g$ state in about 10 ns, emitting red photons at 640 nm [Rellergert2008], which can be detected by an intensified charge-coupled device (ICCD) camera. From the $b^3\Pi_g$ state, molecules quench back to the $a^3\Sigma_u^+$ state. The time scale of this $b \rightarrow a$ quenching can be affected strongly by the vibrational and rotational levels that lie between these two energy states. For instance, some molecules may fall to excited vibrational levels of the $a^3\Sigma_u^+$ state and become trapped in off-resonant $a(1)$ and $a(2)$ vibrational levels due to the long vibrational-relaxation time (about 1 s) [44]. Re-pumping lasers set at 1073 nm and 1099 nm can be used to improve cycling-transition efficiency by exciting these molecules to the c states, where they essentially fall back to the $a(0)$ state in a few nanoseconds and can be reused. This re-pumping method can reduce the $b \rightarrow a$ quenching time down to about 1 ms. Additional lasers for re-pumping the molecules in the excited rotational levels of the $a^3\Sigma_u^+$ state are likely needed if one wants to reduce the quenching time further [44].
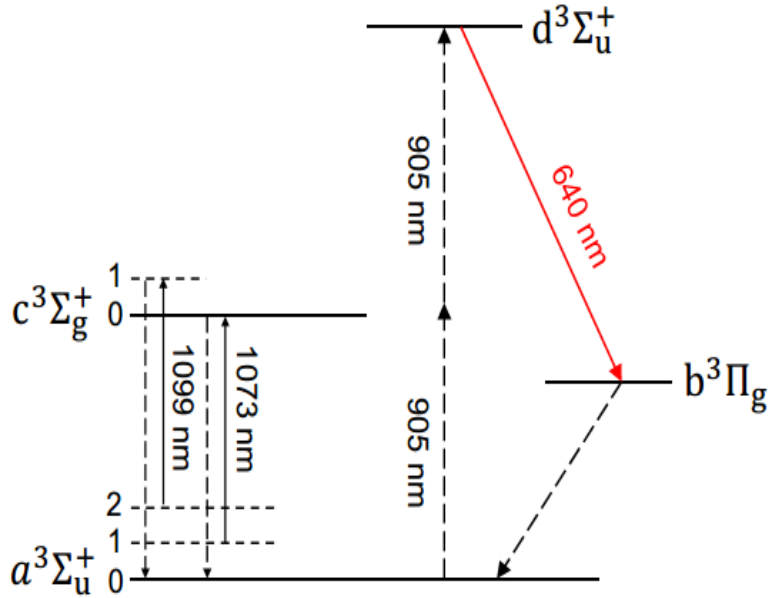
Figure 2.1 Schematic diagram showing the cycling transitions for imaging the He_2^* triplet molecules. The levels labeled 0, 1, and 2 for each electronic state are its vibrational levels.

2.2 Experimental techniques

2.2.1 Tracer line tracking technique

So far, the sensitivity of the fluorescence imaging has not yet been pushed to the limit for the purpose of tracking individual He_2^* molecules. Instead, we choose to develop techniques to extract quantitative information of the flow field by examining the density profile evolution of a large number of molecules. One method of accomplishing this is to create a line of molecules via laser-field ionization in helium and then to study the distortion and dispersion of the line. Laser field ionization in liquid helium is feasible as demonstrated by Benderskii et al. [36]. The light intensity used in their experiment is on the order of $10^{13}\ W/cm^2$.

We study laser-field ionization in our Cryogenics Lab. Figure 2.2 shows the experimental setup designed for this project. An optical helium cryostat (outer diameter $\sim 40\ cm$), manufactured by American Magnetics Inc., is installed on a stainless-steel movable frame. A schematic of the cryostat is shown in Figure. 2.3. Inside the vacuum can of the cryostat, there is a liquid helium bath and a liquid nitrogen shield. The bottom tail sections are detachable, which allows us to access the helium bath. The side windows on both vacuum can and liquid nitrogen shield are installed to
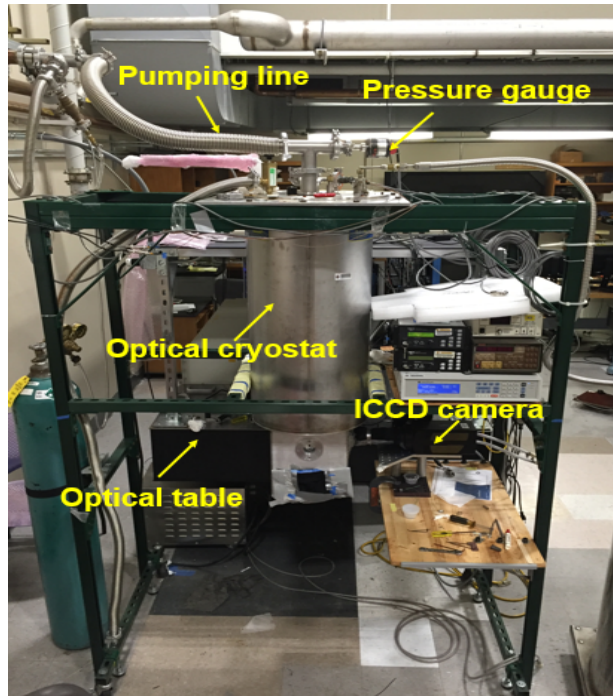
Figure 2.2 Experimental setup that is used in the experiments described in this thesis.
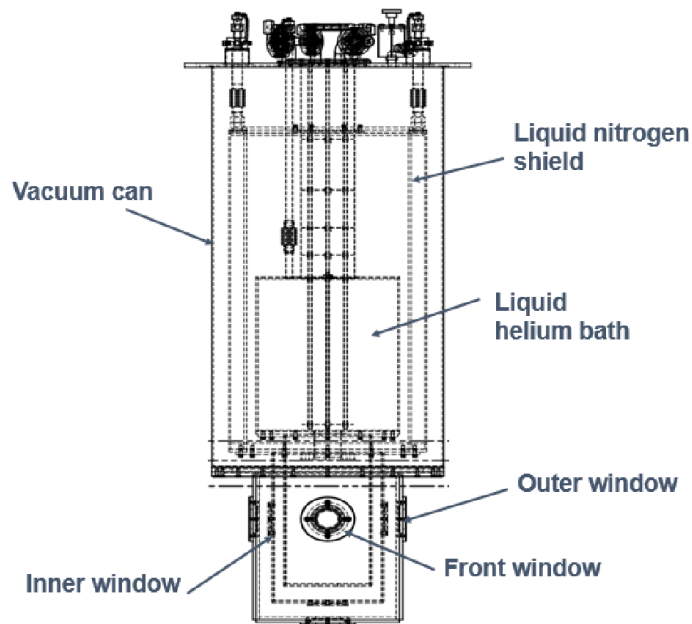
Figure 2.3 A schematic of the cryostat.

allow laser beams pass through. The front windows are used to allow an ICCD camera (PI-MAX3 camera system from Princeton instruments) siting on a fixed plate to visualize the flow inside the

15

cryostat. In addition, the helium bath is connected to a powerful pumping system, and a pressure gauge (MKS instrument) is installed to monitor the bath pressure.

An optical table (5 ft × 10 ft) is installed behind the optical cryostat. A schematic of the layout of the optical components on the optical table is shown in Figure 2.4. In our experiment, we use a commercial femtosecond regenerative amplifier laser system to produce He_2^* molecules. This system includes a Spitfire Ace amplifier seeded by a Mai Tai pulsed laser and pumped by an Empower-45 laser [45]. The output of the amplifier is 35-fs pulses with an adjustable repetition rate up to 5 KHz. The output pulse energy is adjustable with a maximum of about 4 mJ. The imaging laser used in our experiment is an EKSPLA Nd:YAG pulsed laser with a fixed wavelength of 905 nm, and it is operated at 500 Hz. Its pulse duration is about 5 ns and its pulse energy is adjusted so that the laser intensity is about 2.5 mJ/cm^2 per pulse in the flow channel, which is sufficient to saturate the optical transition of the He_2^* molecules [44]. Two fiber diode continuous wave (cw) lasers, at wavelengths of 1073 nm and 1099 nm, are aligned with the imaging laser for enhancing the He_2^* cycling transition efficiency. The output power of these cw lasers is about 1 W. An electronic shutter is used to control the illumination time of the imaging and fiber lasers. We then overlap the imaging laser beams with the femtosecond laser using a thin-film polarizer based beam combiner. This optical setting is used in our subsequent flow visualization experiment.
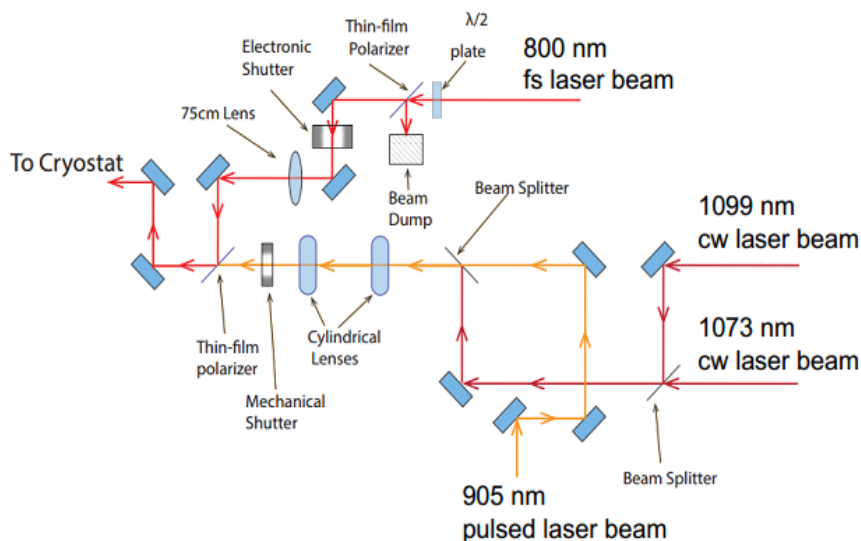
Figure 2.4 A schematic showing the optical layout.

All the combined laser beams are then guided to pass through an optical channel, shown schematically in Figure 2.5(a). The stainless-steel channel (with an inner side width of 9.5 mm and a total length of 300 mm) is mounted at the bottom of the pumped helium bath. This channel can be filled with liquid helium at an adjustable temperature as low as about 1.3 K. The channel runs through a stainless-steel cube, where the flow visualization is performed. The cube has two cylindrical side flanges with indium-sealed sapphire windows. A pair of vertical slots (height ~ 4 mm and width ~ 1.5 mm) is cut through the cube (shown in Figure 2.5(b)) and the channel wall so that the laser beams can pass through. This design helps to avoid laser light scattering in the channel and laser-induced damage to the windows. A sapphire view-window is installed on the front side of the visualization cube, which allows the ICCD camera to view the molecules perpendicular to both the laser beams and the channel axis. A pair of 2nd sound transducers are installed below the visualization cube, the detailed design of which will be discussed in Section 2.2.2. A 640 nm bandpass filter with a full-width half maximum (FWHM) bandwidth of 20 nm is installed on the camera to block unwanted laser light and to minimize the background. The femtosecond laser beam is first expanded to have an appropriate entrance beam diameter and is then focused to pass through the channel using a convex lens. Figure 2.6(a) shows a schematic of the spatial profile ($1/e^2$ intensity contour) of the femtosecond laser beam inside the channel.
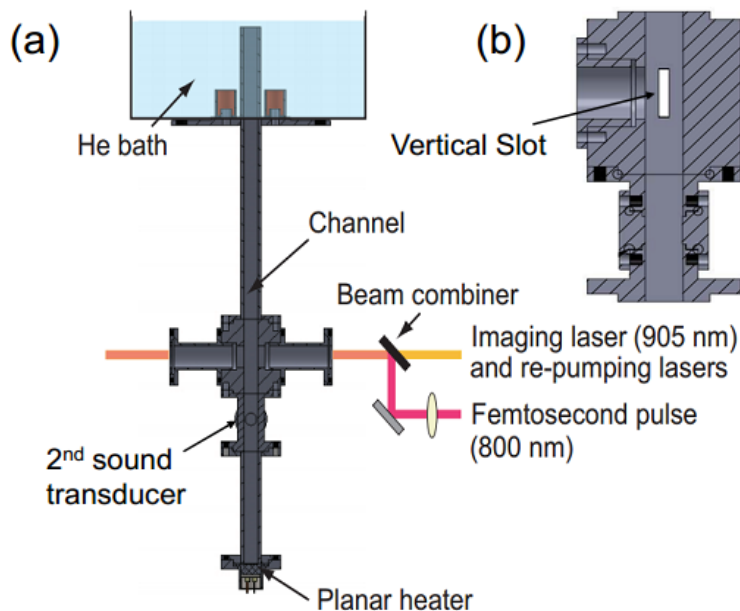
Figure 2.5 (a) Schematic diagram showing the optical channel. (b) Cross section view of the visualization cube.

For an ideal Gaussian beam, if we denote ω_0 as the radius of the $1/e^2$ irradiance intensity contour at the focal plane where the wave front is flat, then the $1/e^2$ intensity contour radius $\omega(z)$ at a distance z from the focal plane is given by [46]

$$\omega(z) = \omega_0 \left[1 + (\frac{\lambda z}{\pi \omega_0^2})^2 \right]^{1/2}, \tag{2.3}$$

where λ is the wavelength of the beam (about 800 nm). One can define a distance called the Rayleigh range (Z_R) over which the beam radius spreads by a factor of $\sqrt{2}$ as $Z_R = \pi \omega_0^2 / \lambda$. The laser intensity only drops from the focal plane to the Rayleigh range boundary by a factor of 2, and the He_2^* molecules are, therefore, expected to be produced essentially within the Rayleigh range from the focal plane. In order to characterize the profile of our femtosecond laser beam near the focal plane, we measured the beam cross-section intensity profile using an infrared camera. The beam cross-section intensity profile, measured at the focal plane, is nearly Gaussian, with a typical M^2 factor of 1.04 (M^2 values close to 1 indicate that the beam profile is very close to a Gaussian profile [47]). The beam radius ω_0 can be determined from a Gaussian fit of the profile. We repeat the measurement at a different location (z) along the beam propagation direction. The variation of the beam radius ω with z is shown in Figure 2.6 (b), which agrees with the profile given by equation (2.5) (the red solid line in Figure 2.6(b)).

The thickness of the molecular tracer line is expected to be controlled by the width of the femtosecond laser beam ω_0. One can easily derive that ω_0 is related to the focal length f of the lens and to the incident beam radius on the lens ω_f via $\omega_0 = \lambda f / \pi \omega_f$. As a consequence, by using a lens with an appropriate focal length f, or by adjusting the incident beam radius ω_f, any desired thickness of the tracer line can be achieved. In principle, the line thickness, which sets the spatial resolution in our flow visualization experiment, is only limited by optical diffraction, which occurs when the femtosecond laser beam diameter $2\omega_0$ becomes comparable to its wavelength (about 800 nm).

In our experiment, the intensifier of the camera is synchronized with the imaging laser and is turned on for 14 μs following every imaging laser pulse in order to collect the induced fluorescent
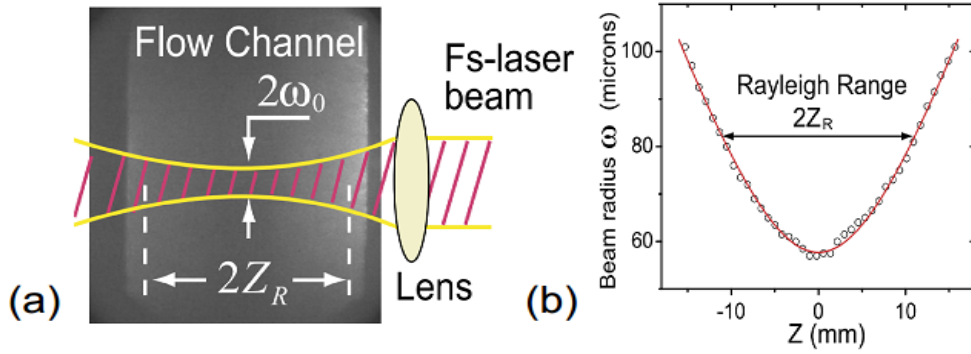
Figure 2.6 (a) Schematic diagram showing the femtosecond beam profile in the channel. (b) A measurement of the $1/e^2$ intensity contour radius $\omega(z)$ as a function of position z along the beam propagation direction.

light. The quality of the tracer-line images depends on the density of the He_2^* molecules and the number of the imaging laser pulses applied. The saturation molecule density is controlled by the balance between the generation resulting from the femtosecond laser illumination and decay due to bi-molecular Penning ionization reaction [48]. Our femtosecond laser system is usually operated at 5 KHz. Its illumination time is limited by the minimum open time of the electronic shutter, which is around 5 ms. Under these conditions, we determine that 6 pulses (~ 10 ms) from the 905 nm imaging laser could provide a satisfactory fluorescence signal.

In a typical experiment, we first generate a flow in the channel. Then sending in femtosecond laser pulses allows to create a tracer line. The tracer line is allowed to move with the normal fluid with a certain "drift time", t_{drift}, and can be imaged with the 905 nm imaging laser pulses. When the image is taken in a static flow with zero drift time, we call it the baseline image. A typical baseline image of the He_2^* tracers created in superfluid helium is shown in Figure 2.7 (a). As expected, the thickness of the He_2^* tracer line matches the diameter of the femtosecond laser beam in the focal region, and the length of the line is comparable to twice the Rayleigh range of the beam. The images are created using a lens with $f = 75$ cm. In this case, the tracer line has a length of about 2.2 cm, and it extends across the whole channel and into the side flanges. This imaged portion of the tracer line inside the follow channel exhibits a fairly uniform thickness. We find that, above the threshold laser intensity at which dielectric breakdown occurs in liquid helium,

19

diffuse clouds of He_2^* molecules are formed, compromising the quality of the tracer line (as illustrated in Figure 2.7 (b)). This threshold laser intensity corresponds to a femtosecond laser pulse energy of about 60 μJ, similar to what Benderskii et al. [36] reported. Due to the short illumination time of the laser beams and their high transmission through the coated windows in the flow channel, we do not observe any noticeable laser heating in our experiments. As shown in Figure 2.8, the width of the tracer line broadens, but no relative motion is observed in the static helium. The estimated diffusion coefficient at 1.85 K is only 3×10^{-4} cm^2/s [42]. The expected width broadening due to molecular diffusion in 20 ms is around 4 μm, which is consistent with our observation.
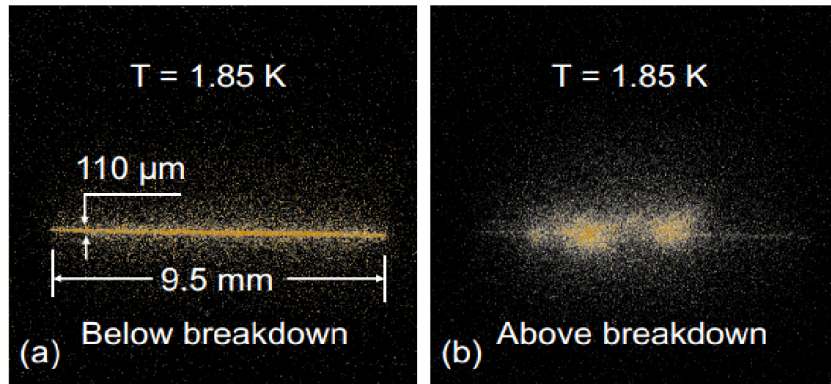
Figure 2.7 (a) With femtosecond laser pulse energy slightly below 60 μJ, a thin line of He_2^* tracers across the full width of the channel can be produced. (b) Above the breakdown pulse energy, dielectric breakdown occurs in He II, and isolated clusters of He_2^* tracers are produced.
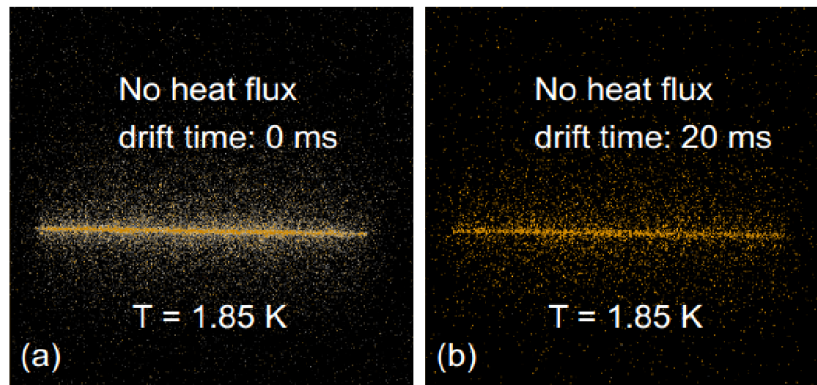
Figure 2.8 (a) A baseline image obtained in static helium at 1.85 K. (b) A tracer line image with 20 ms drift in static helium at 1.85 K.

2.2.2 2nd sound attenuation technique

In addition to flow visualization of the normal fluid, we have adopted the standard second-sound attenuation method to measure the quantized vortex line density in the superfluid component. The combination of these two techniques allow us to probe both fluids in the same experiment, which yields unprecedented quantitative information about the complex hydrodynamics of the two-fluid system.

A pair of 2nd sound transducers has been made and installed in the flow channel (shown in Figure 2.4(a)). The detailed structure of the transducers is shown schematically in Figure 2.9(a). A porous membrane with a 0.2 μm pore size and a 3×10^8 pores/cm^2 pore density is stretched over a plastic membrane holder and attached to the surface of a brass disc electrode. The channel-facing side of the membrane is coated with gold of about 500 Å in thickness. Stycast that is contained by a G10 cylinder is used to seal the electrical pin. The electrode and the membrane forms a capacitor. When a biased DC voltage is applied to the brass electrode, the gold coated membrane is pulled tightly toward the brass disc surface. We then apply a sinusoidal AC voltage to the brass disc to cause the membrane to vibrate. In He II, the superfluid component can flow through the porous membrane, but the normal fluid component is blocked due to its viscosity [49]. As a consequence, the two-fluid components move out of phase and 2nd sound waves are generated in the channel (shown in Figure 2.9(b)). When the 2nd sound waves propagate across the channel, they become attenuated as they scatter along the vortex lines. The attenuated 2nd sound waves can be received by the other transducer on the opposite side of the channel and detected as an AC signal. The attenuation of the 2nd sound provides us with information about the average vortex density in the flow channel.

Figure 2.10 shows a diagram of the electronics used for the 2nd sound attenuation measurement. Normally, a 100 - 150 V DC voltage is applied to the transducer. Then, the function generator outputs a sinusoidal voltage waveform with a 6 V peak that can drive the emitter transducer. As a consequence, the 2nd sound wave can be excited in the channel. Two capacitors are added to isolate the function generator and the lock-in amplifier from the high voltage sources. The Stanford Research Systems 830 lock-in amplifier is synchronized with the function generator to detect the small pickup oscillating voltage from the receiver transducer.

(a)

(b)
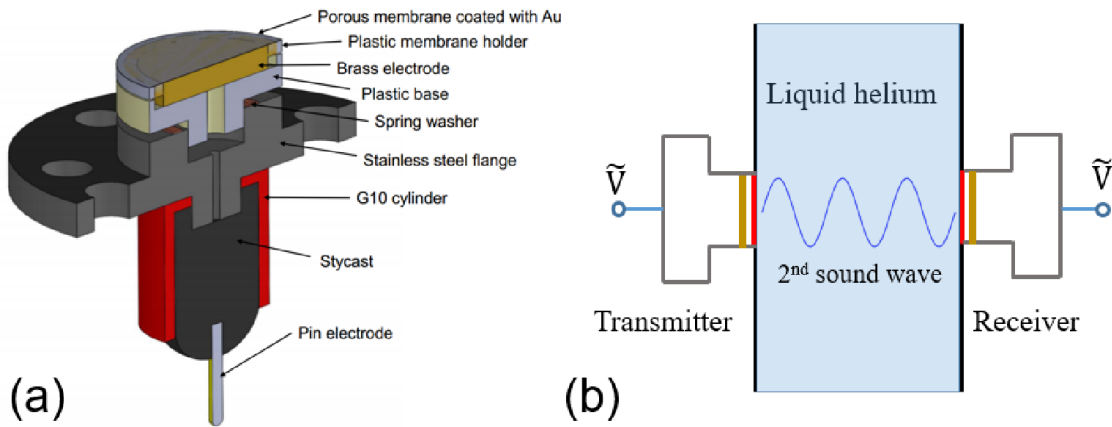
Figure 2.9: (a) The 2nd sound transducer design. (b) Schematic showing the arrangement of transducers in the flow channel.
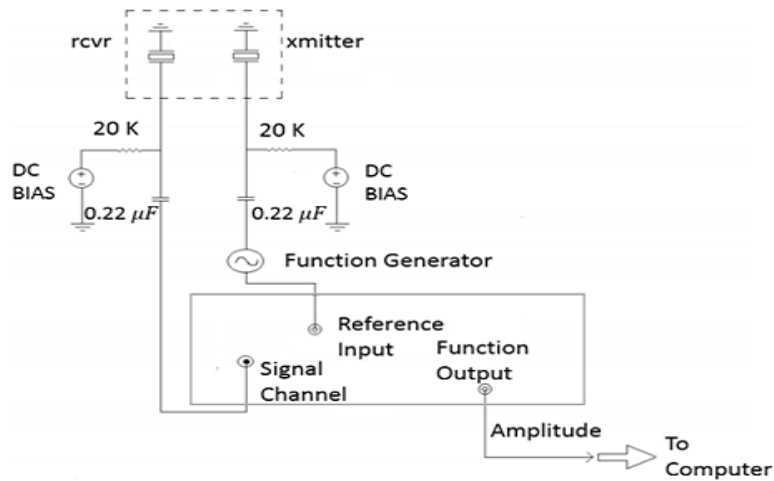
Figure 2.10 Schematic electric diagram showing the electronics setup for 2nd sound measurement.

2.3 Data analysis method

2.3.1 Image data analysis

In order to extract the flow velocity field information based on the tracer line images, a reliable algorithm for image processing is needed. All data analyses are based on self-made code written in FORTRAN. A Gaussian profile-fitting method is implemented in the image data analysis [50].

22

As shown in Section 2.2, our femtosecond laser beam had a Gaussian intensity distribution profile, so it is reasonable to assume that the light intensity distribution of the tracer line would also have a Gaussian profile. An ICCD camera image consists of 1024×1024 pixels, with the value associated with each pixel representing the light intensity. Normally, a line segment is selected, as shown in Figure 2.11(a). The width of the segment is chosen to be greater than the typical width of the molecular line but much smaller than the typical drift distance of the line. In order to determine the position of the segment center, the light intensity is integrated along the horizontal direction (x axis) and is then plotted as a function of the vertical position (y axis). An example is shown in Figure 2.11(b). The integrated light intensity peaks at about $y = 6.8$ mm. Assuming the presence of a Gaussian fluorescence intensity profile, a least square fitting method is used, which yields a subpixel resolution and accurate velocity measurement. We generate a least square fitting routine to find four unknown parameters (y_0 = background intensity, A = height, y_c = line center position, and σ = width), describing the intensity profile as follows:

$$I(y) = y_0 + Ae^{(\frac{-(y-y_c)^2}{2\sigma^2})}. \tag{2.4}$$

The accuracy of this method is around 0.5-1 pixel, corresponding to 5-10 microns. However, some bright spots far from the line region may occur due to dark current in the ICCD cameras or reflection light from the back of the channel. Such bright pixels have discrete distribution, especially the extremely bright spots, which can easily fool the fitting routine. We discard these bright pixels before any further processing. Moreover, the line segment will be eliminated if its light intensity is too low to produce a reasonable Gaussian fit. The fraction of omitted line segments is less than 1 % in typical set of 200 images. Figure 2.12 shows an example of the line center position determined using our image-processing algorithm.

In a typical experiment, a baseline image in a static flow is acquired with zero drift time first, which allows us to determine the initial location of the tracer line. An image of the line at a given drift time t in a turbulent flow is then taken and the center locations of the line segments are determined (as shown in Figure 2.13). The displacement of each line segment can be calculated and the vertical flow velocity can be computed as the vertical displacement divided by the drift time. This way, we are able to compute the flow velocity at every segment perpendicular to the molecular line. Normally, we take one baseline image after taking 10 drifted-line images.
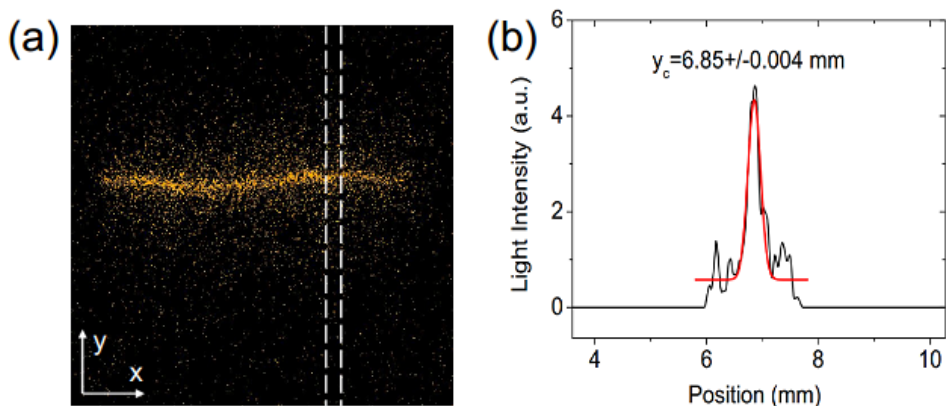
Figure 2.11 (a) A fluorescence image of a He_2^* molecular line. The region between the two dashed lines represents one line segment. (b) The light intensity integrated along the x axis for the stripe shown in (a) is a function of the y location. The red solid line is a Gaussian fit to the integrated light intensity profile.
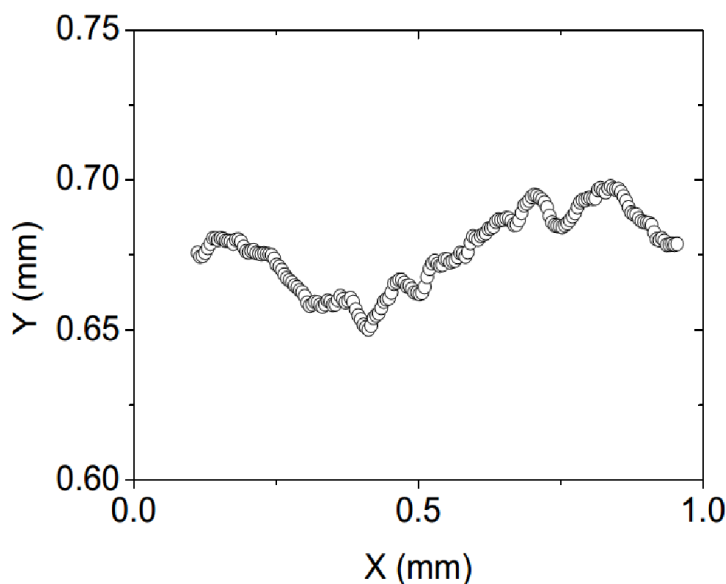
Figure 2.12 Typical line center position determined by our image processing algorithm. The raw image data is shown in Figure 2.12 (a).

In a typical experiment, a baseline image is acquired with zero drift time first, which allows us to determine the initial location of the tracer line. An image of the line at a given drift time t is then taken and the center locations of the line segments are determined (as shown in Figure 2.13). The displacement of each line segment can be calculated. Then the vertical flow velocity can be

24

computed as the vertical displacement divided by the drift time. This way, we are able to compute the flow velocity at every segment perpendicular to the molecular line. Normally, we take one baseline image after taking 10 drifted-line images.

Conducting this measurement many times under the same experimental condition allows us to investigate the statistical properties of the flow of the normal fluid component. By averaging a number of deformed line images, we are able to calculate the local mean and standard deviation of the velocity. Also, a probability density function (PDF) for the velocity can be generated if we have large enough velocity samples. Further, by correlating the streamwise velocities of the two line segments (see schematic in Figure 2.13), we can compute the second order transverse structure function, $S_2^{\perp}(R,r)$, defined as,

$$S_2^{\perp}(R,r) = \overline{\left\langle u(R+r/2) - u(R-r/2)^2 \right\rangle},$$ (2.5)

where $u(R+r/2)$ and $u(R-r/2)$ are velocities of two line segments that are $r/2$, either left or right from the reference point, R, and the bar denotes ensemble averaging. The results will be presented in subsequent chapters.
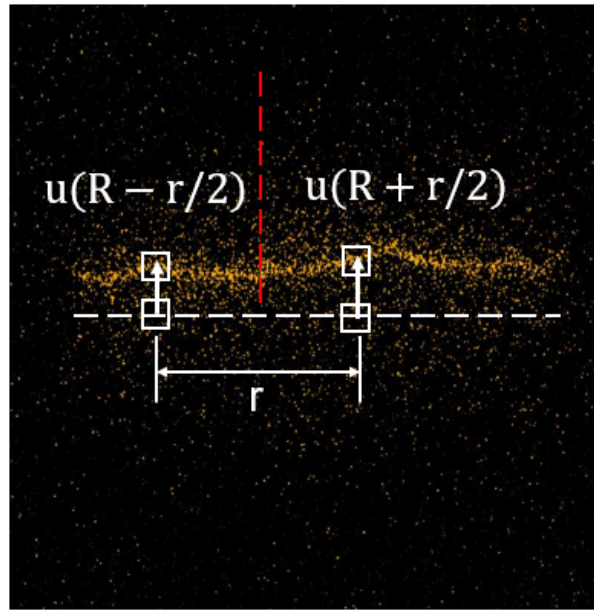
Figure 2.13 A schematic showing the process of the second order transverse structure function calculation. The white-dashed line represents the initial straight tracer line. The red-dashed line donates the reference position, R.

2.3.2 2nd sound data analysis

The 2nd sound attenuation measurements are conducted as follows. First, the function generator is set to sweep from 1 KHz all the way to 30 KHz (shown in Figure 2.14) so that the complete spectrum of the 2nd sound modes can be obtained. We then pick a candidate resonance peak with a high-quality factor and good symmetric profile. For instance, at 1.65 K , a candidate resonance peak around 12.3 KHz is selected. Next, we set the function generator to scan 1000 Hz centered around the resonance peak so that we can make an accurate measurement of the peak amplitude. When there are vortices in the flow channel, the 2nd sound resonance peak amplitude is reduced. Figure 2.15 shows an example of the attenuation of the 2nd sound resonance peak in a counterflow with a heat flux of 426 mW/cm^2 applied. The full width at the half maximum height of the zero heat flux resonance peak, Δf_0, is measured to be around 45 Hz . Assuming that the vortex tangle is homogeneous and isotropic, the vortex line density L, (i.e., the vortex line length per unit volume of He II) can be calculated as [51]

$$L = \frac{6\pi\Delta f_0}{B\kappa}(\frac{\overline{A_0}}{\overline{A}}-1),\tag{2.5}$$

where B is the mutual friction coefficient (tabulated in Ref. [52]), κ is the quantum circulation, $\overline{A_0}$ and $\overline{A}$ are the mean heights of the resonance peak at zero and finite heat flux, respectively.
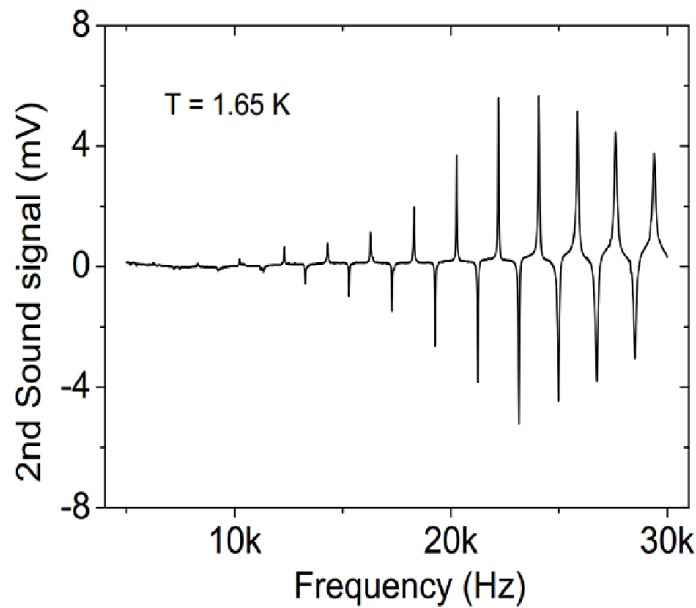
Figure 2.14 A complete 2nd sound spectrum from 1 KHz to 30 KHz .
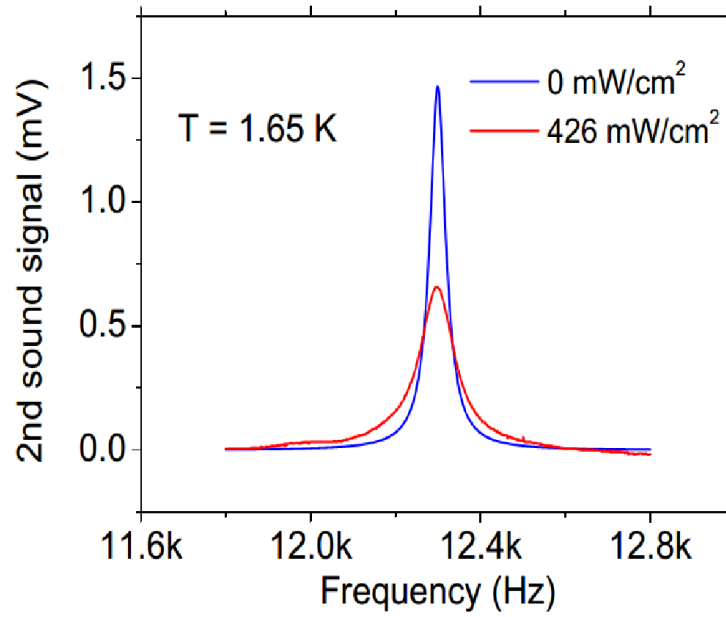
Figure 2.15 Typical trace showing the attenuation of the 2nd sound resonance peak. The blue curve is obtained without any heat flux. The red curve is obtained with 426 mW/cm^2 heat flux.

CHAPTER 3

STEADY STATE THERMAL COUNTERFLOW

We have applied the recently developed tracer line imaging technique to the study of steady state thermal counterflow measurement. We show that the tracer molecules do follow the motion of the normal fluid component in both laminar and turbulent flow regimes. At relatively small velocities, where the superfluid is already turbulent, the flow of the normal fluid remains laminar, but with a distorted velocity profile, while at a higher velocity there is a transition to turbulence. A spatially non-uniform mean normal fluid velocity profile across the flow channel has been observed. The extremely high normal fluid turbulence intensity has been measured, which appears to be controlled primarily by temperature. The form of the second order transverse structure function in this turbulent state deviates from that found in classical turbulence as the heat flux increases.

3.1 Overview

In the 1950s, Vinen revealed that the thermal counterflow can generate turbulence in the superfluid component [13]. As discussed in Chapter 1, Vinen proposed a phenomenological model to describe the variation of the vortex line density in thermal counterflow. Based on the assumption that the vortex tangle is random and homogeneous, Vinen's model states that

$$\frac{dL}{dt} = \left(\frac{dL}{dt}\right)_{gen} - \left(\frac{dL}{dt}\right)_{decay} = \frac{\rho_n B}{2\rho}\chi_1 v_{ns}L^{3/2} - \frac{\kappa}{2\pi}\chi_2 L^2 . \tag{3.1}$$

In the steady state thermal counterflow $dL/dt = 0$, the vortex line density is related to the relative velocity between the two fluids by

$$L = \gamma^2 (v_s - v_n)^2 , \tag{3.2}$$

where the line density coefficient γ is temperature dependent. Vinen first observed this behavior in a steady state thermal counterflow experiment. The coefficient γ has been measured in many experiments, as shown in Figure 3.1. The mechanism by which the superfluid turbulence is generated in thermal counterflow was elucidated in pioneering computer simulations by Schwarz [53]. He implemented the vortex filament model and the local induction approximation (LIA) to simulate the quantized vortices. His simulation showed that the force of mutual friction can lead

to the stretching of the vortex lines and that this, in turn, can lead to self-sustaining turbulence in the superfluid component, provided that the vortex lines are allowed to reconnect. New vortex lines can be generated via reconnection, and the vortices are simply pushed by mutual friction to the container wall if there are no reconnections. It is also assumed that the flow is spatially uniform and that the flow of the normal fluid remains laminar. In this model, the turbulence in the superfluid component takes the form of a random tangle of vortex lines, so that there is little turbulent energy on the length scales significantly larger than the average spacing of $l = L^{-1/2}$ between vortex lines. Significant polarization of these vortex lines, which would lead to the existence of turbulent energy on lager scales, is missing. Although, in this case, the theory of thermal counterflow has been simplified, the calculated vortex line density shows good agreement with Vinen's prediction. The solid line in Figure 3.1 is the simulated value γ as a function of temperature, which agrees very well with these experimental observations.

It seemed we had a good understanding of thermal counterflow turbulence based on Vinen's model. Later, however, K.P. Martin and J.T. Tough [54] found that this picture was incomplete. By using second sound measurements, their experiment revealed two different regimes of quantum turbulence in a circular counterflow tube with a diameter d of 1 mm. Their results are shown in Figure 3.2. The initial vortex line density was zero until the counterflow velocity reached the first critical velocity v_{c1}. Then, the vortex line density increased slowly until the second critical velocity v_{c2} was reached, after which the vortex line density jumped higher and followed Vinen's prediction. There seemed to be two different regimes as the heat flux was increased, characterized
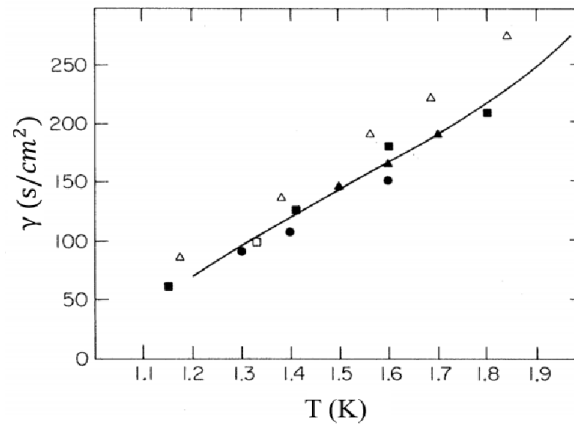
Figure 3.1 Figure reproduced from Ref [54] showing the measured γ from a number of experiments: black triangles [54], black circles [55], black squares [56], while triangles [57] and while squares [58]. Solid line is the calculation of Schwarz [59].

by TI and TII. This observation led Melotte and Barenghi [60] to suggest that the TI to TII transition could relate to the transitions to turbulence in the normal fluid. They proposed that, in the TI state, the superfluid is turbulent while the normal fluid is still laminar and that both fluid components become turbulent in TII state. Previous second sound experiments with large channels only showed the existence of the TII transition in the superfluid.
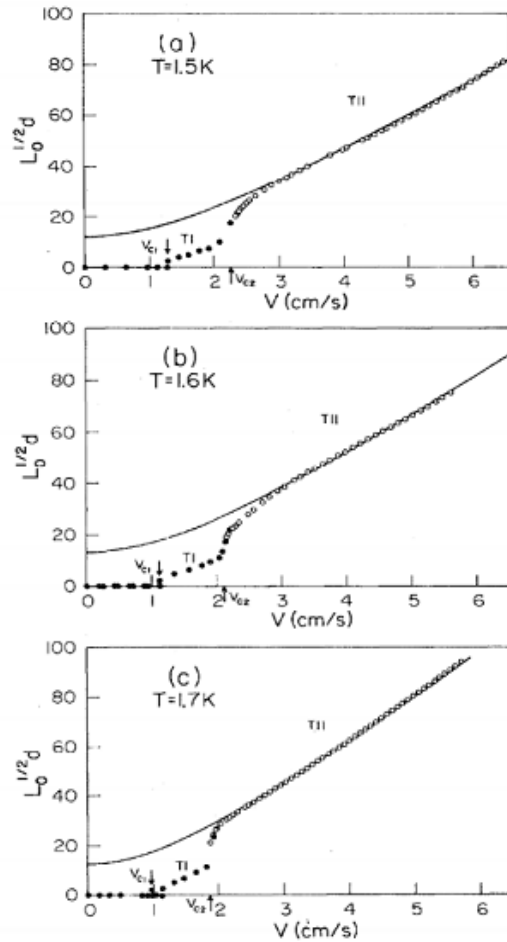
Figure 3.2 Figure reproduced from Martin's plot of the vortex line density [54]. It is shown as the dimensionless number $L_0^{1/2}d$, as a function of counterflow velocity at 1.5, 1.6, and 1.7 K. The initial vortex line density was zero until the counterflow velocity reached the first critical velocity v_{c1}. Then the vortex line density increased slowly until the second critical velocity v_{c2} was reached, after which the vortex line density jumped up and followed Vinen's prediction.

In a recent experiment conducted by Guo et al. [15], it was revealed that the normal fluid can also become turbulent in thermal counterflow. For their experiment, they produced He_2^* molecules

via field emissions from the tungsten needle. A focused pump laser pulse was used to tag the He_2^* molecules. At a given delay time, an expanded probe laser pulse was then used to selectively image the tagged line of the molecules. However, due to low tagging efficiency ($\sim 4\%$), at each given pump-probe delay time, a large number of images of the tracer line need to be averaged, which prohibits the study of line distortion. As a consequence, the quantitative information of the normal-fluid velocity is lost. Our tracer line imaging technique, with high quality single-shot images, offers a unique way to extract quantitative information about the motion of the normal fluid component. Combining the second sound measurement, we can examine how the normal fluid component behaves while the superfluid flow undergoes TI and TII transitions, and we can test these predictions experimentally. In addition, normal fluid turbulence in thermal counterflow is a novel form of turbulence since dissipation occurs at all length scales. Studying this novel form of turbulence in counterflow can broad our understanding of turbulence in general. Turbulent normal-fluid flow in thermal counterflow can lead to heat-flux fluctuations in both the space and time domains. Thus, characterizing the velocity fluctuations and, hence, determining heat flux fluctuations can be vitally important for systems that require high thermal stability.

3.2 Experimental setup

A schematic diagram of the experiment is shown in Figure 3.3. A stainless steel counterflow channel (square cross section: 9.5 mm; length 300 mm) is attached to a pumped helium bath. A solenoid valve (MKS instrument) is used to control the pumping rate and, hence, to adjust the pressure in the bath. A desired pressure value can be set in the proportional-integral-derivative (PID) pressure controller, the resolution of which is 1 $mtorr$. Then, the open percentage of the solenoid value can be adjusted based on the difference between the measured and the desired bath pressure. By carefully tuning of the P, I, and D parameters, the bath pressure fluctuation can be controlled within 1 $mtorr$. Consequently, the bath temperature fluctuation is maintained within 0.1 mK. A planar heater made of a series of four thick film resistors (the resistance of each is 100 Ω) placed at the lower end of the channel is used to drive the counterflow. A pair of porous membrane second sound transducers installed below the visualization regime allows the measurement of the vortex line density.

31
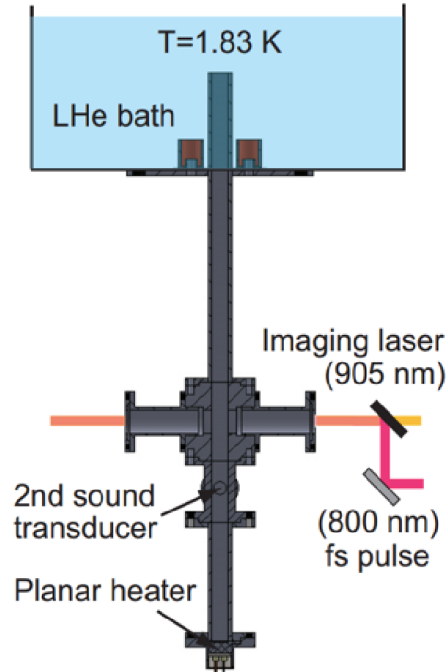
Figure 3.3 Schematic diagram of the experimental setup. A stainless steel counterflow channel (square cross section: 9.5 mm; length 300 mm) was attached to a pumped helium bath, the temperature fluctuation of which was maintained within 0.1 mK for the experiment. A planar heater at the lower end of the channel was used to drive the counterflow. A pair of porous membrane second sound transducers was installed below the visualization regime.

In a typical steady state thermal counterflow experiment, we first activate the heater for about 20 s and then send in femtosecond-laser pulses to create a tracer line. The tracer line is allowed to move with the normal fluid for a certain drift time and is then imaged with the 905 nm imaging laser pulses. At relatively low heat flux, t_{drift} can be as large as 100 ms. For high heat flux measurements, t_{drift} needs to be less than the eddy turnover time in order to extract quantitative information about the turbulent flow. The eddy turnover time represents the eddy's lifetime, which is defined as eddy size divided by velocity increment across the eddy. For instance, at 1.85 K with heat flux 330 mW / cm^2, the eddy turnover time is about 50 ms on a length scale around 200 μm. The ICCD camera is synchronized with each imaging laser pulse and its exposure time is set to be around 14 μs to minimize background noise and to achieve a better signal-to-noise ratio. Figure 3.4 shows typical tracer line images obtained at various heat fluxes for a temperature of 1.83 K. At heat fluxes below about 50 mW / cm^2, an initially straight tracer line deforms to a

nearly parabolic shape. As the heat flux increases, the tail part of the tracer line becomes flattened. Above about 80 mW/cm^2, the tracer line becomes distorted randomly. More discussion will be presented in Sections 3.3 and 3.4. An example of mean flow velocity as a function of heat flux is shown in Figure 3.5. The heat flux is scanned from 10 mW/cm^2 all the way to 400 mW/cm^2. The mean flow velocity in the turbulent flow regime is obtained by averaging the velocity over 200 single shot images and over the length of the line of tracers. The solid line is the velocity given by equation (1.14). In our results, good agreement between the theoretical prediction and the measured results indicates that the He_2^* tracers follow the motion of the normal fluid.
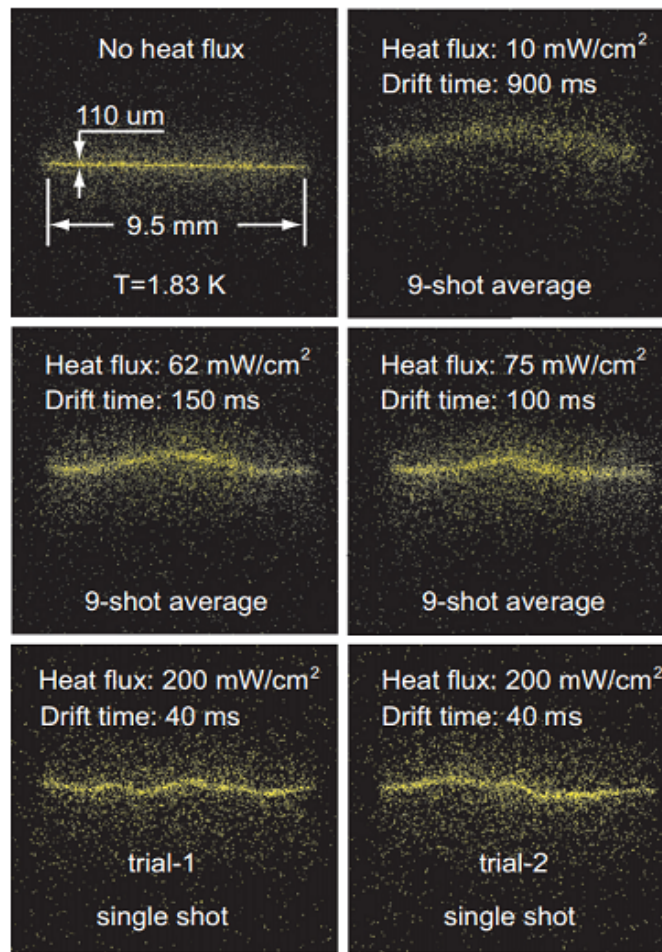
Figure 3.4 Typical fluorescence images showing the motion of He_2^* tracer lines in the thermal counterflow. At heat fluxes below about 50 mW/cm^2, an initially straight tracer line is deformed to a nearly parabolic shape, indicating the laminar Poiseuille velocity profile of the normal fluid. As the heat flux increases, the tail part of the tracer line becomes flattened. Above about 80 mW/cm^2, the tracer line distorts randomly, indicating turbulent flow in the normal fluid. The images shown in the laminar flow regime are averaged over single shots.

33
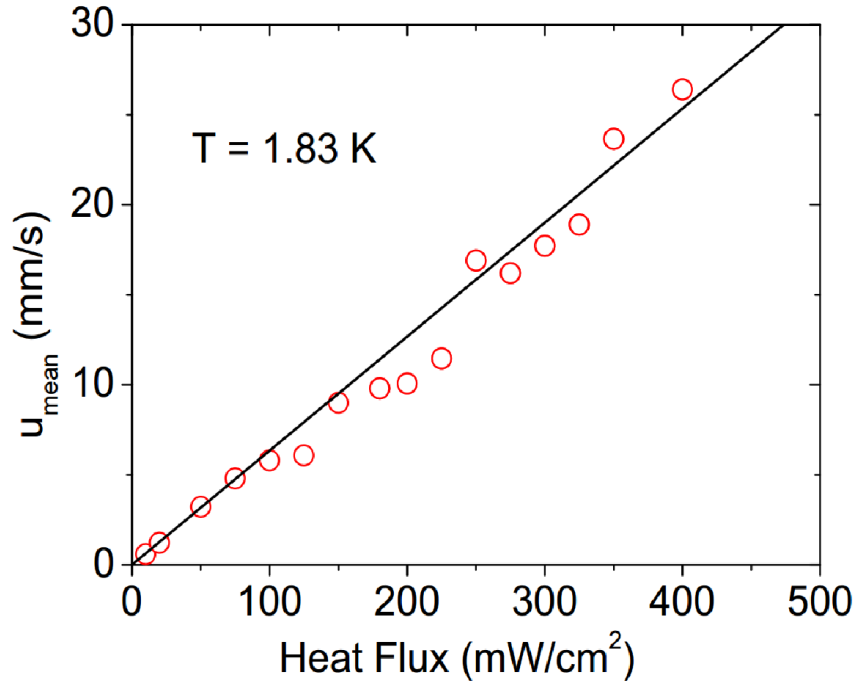
Figure 3.5 The observed mean normal fluid velocity as a function of heat flux. The solid line shows the calculated velocity based on equation (1.14).

3.3 Laminar flow

Although the laminar velocity profile in a square channel is not an exact parabolic shape, like in a circular channel flow, the difference is quite small [61]. For $q < \sim 50 \ mW/cm^2$, we observe that a straight excimer line deforms to a nearly parabolic shape, indicating the Poiseuille laminar-flow velocity profile of the normal fluid in our square flow channel. An example is shown in Figure 3.4. To show a large deformation of the tracer line, a $900 \ ms$ drift time at $10 \ mW/cm^2$ is used. To enhance the image quality, 9 single shot images are averaged. From such an image, we can then compute the velocity profile. Figure 3.6(a) shows an averaged image taken with $20 \ mW/cm^2$ at $1.83 \ K$. The calculated velocity profile pertinent to Figure 3.6(a) is shown in Figure 3.6(b). Since there are two narrow slots cut into the channel to allow laser beams to pass through it, the normal fluid velocity near the slots is not precisely zero. The velocity profile can be fitted by a parabolic profile represented by the red curve in Figure 3.6(b). We also find that the velocity at the center of the channel is about twice as large as that of the expected mean, which is consistent with Poiseuille flow.
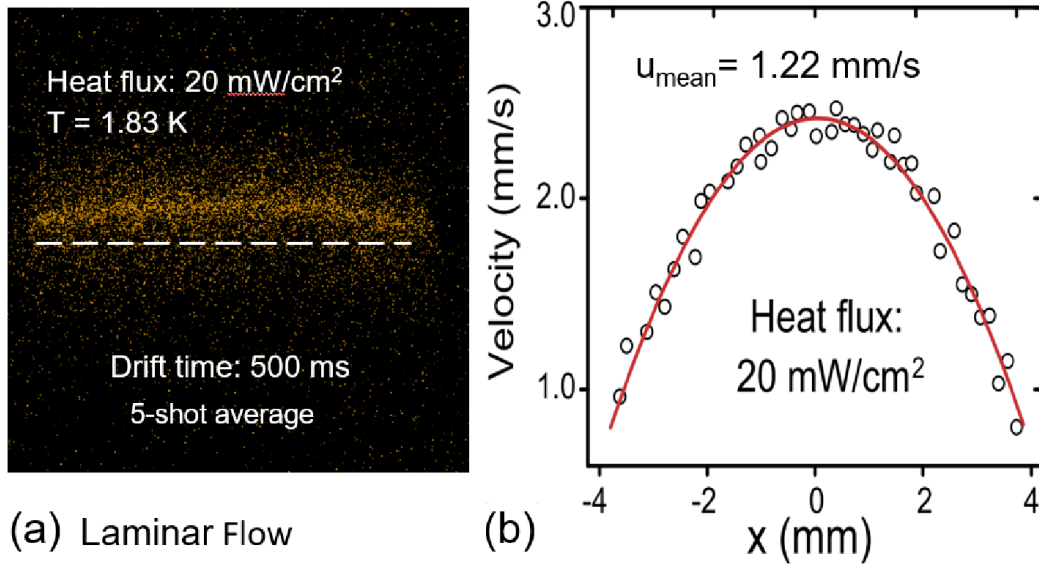
(a) Laminar Flow
(b)

Figure 3.6 (a) A typical 5-shot averaged image of the tracer line in thermal counterflow when the hrat flux is small. (b) The calculated normal-fluid velocity profile for laminar normal-fluid flow. The red solid curve is a parabolic fit to the data.

As we gradually increase the heat flux to $\sim 50~mW/cm^2 < q < \sim 80~mW/cm^2$, the outer part of the tracer line becomes flattened, and only the center part of the line remains curved. However, for a given q, this flattening is reproducible from one trial to another, suggesting that the flow is still laminar. In addition, any turbulence on a scale less than about 0.1 mm leads to an anomalous broadening of the line of molecules. The tracer line width analysis based on single shot images in laminar (40 mW/cm^2), distorted laminar (70 mW/cm^2), and turbulent flows (150 mW/cm^2) with the same drift time (100 ms) shows that the width of the tracer line increases by less than 5 % from the laminar flow regime to the distorted laminar flow regime, but more than 14 % from the distorted laminar regime to the turbulent flow regime. This also suggests that for $q < \sim 80~mW/cm^2$, the flow is still in laminar with no detectable small-scale turbulence. For $q > \sim 80~mW/cm^2$, we observed random distortions of the lines, indicating large-scale turbulent flow in the normal fluid. If the change of the normal fluid velocity profile is due to mutual friction with quantized vortices, our observation might suggest that, in this heat flux regime, the quantized vortices could accumulate near the channel wall and, therefore, more strongly affect the tail part of the tracer line.

Indeed, several computer simulations have shown that the density profile of the vortex lines can be modified substantially by realistic forms of the normal fluid flow, both laminar and turbulent [62,63]. For instance, Arts and Waele [62] have done computer simulations of counterflow using the vortex filament model with a LIA. They assumed a parabolic normal fluid velocity profile, finding that the resulting vortex line density was non-uniform and appeared to be greater near the walls than at the center of the channel. Recently, Baggaley et al. adopted the full Biot-Savart law in their simulations [63]. Figure 3.7 represents snapshots from their simulation of the vortex tangle with a laminar (left) and turbulent (right) normal fluid at $1.9 \ K$. The flow direction is perpendicular to the plane. Their results revealed that if a parabolic velocity profile of the normal fluid was assumed, the vortices tended to accumulate near the channel wall, whereas if a turbulent velocity field, obtained by numerically solving the incompressible Navier-Stokes equations, was assumed then the vortices distributed in the channel uniformly. They also predicted that the transition to the normal fluid turbulence would correspond to an abrupt increase of the vortex line density.
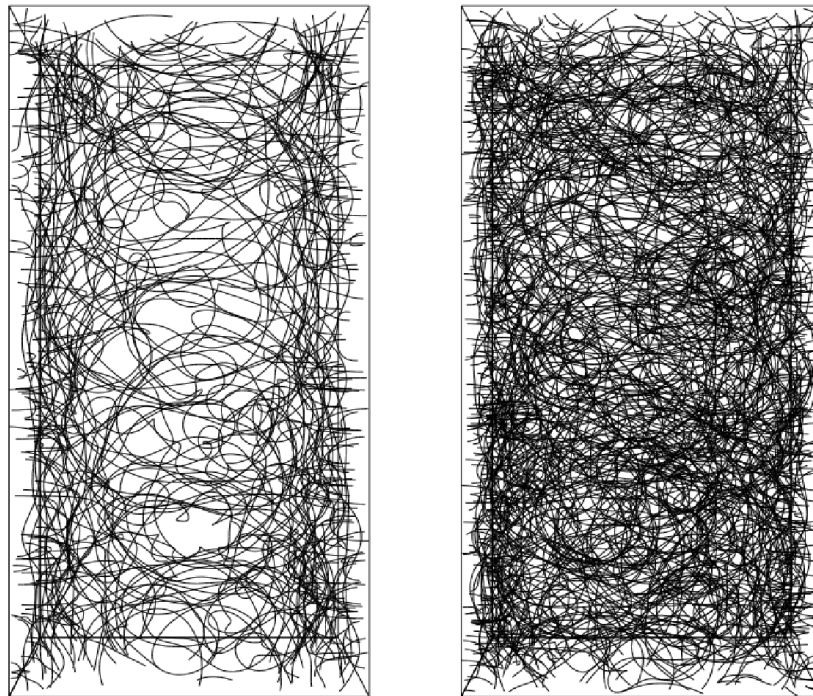
Figure 3.7. Reproduced from Ref [63]. Snapshots of the vortex configuration with prescribed laminar (left) and turbulent (right) flow of the normal fluid at $1.9 \ K$. The flow direction is perpendicular to the plane.

To investigate the behavior of the superfluid as the normal fluid undergoes a transition to turbulence, we have measured the vortex line density L using second sound attenuation. The result is shown in Figure 3.8. Below about 50 mW/cm^2, L is too small to be measurable. Above about 80 mW/cm^2, $L^{1/2}$ grew linearly with the heat flux. The line density coefficient γ is found to be 166 s/cm^2, which is consistent with the reported value found in the fully turbulent TII state [54]. At the transition to normal fluid turbulence around 80 mW/cm^2, we find no abrupt increase of the vortex line density, which is in disagreement with Baggaley's simulations [63].

Similar results have been observed at other temperatures. For instance, at 1.65 K, we observed the distorted laminar normal fluid velocity profile for $\sim$ 30 $mW/cm^2 < q < \sim$ 60 mW/cm^2. Above about 60 mW/cm^2, $L^{1/2}$ grows linearly along with the heat flux and the line density coefficient γ is around 156 s/cm^2.

Figure 3.8 The square root of the measured vortex line density as a function of heat flux in the channel. The solid blue line is a fit to data above 80 mW/cm^2.
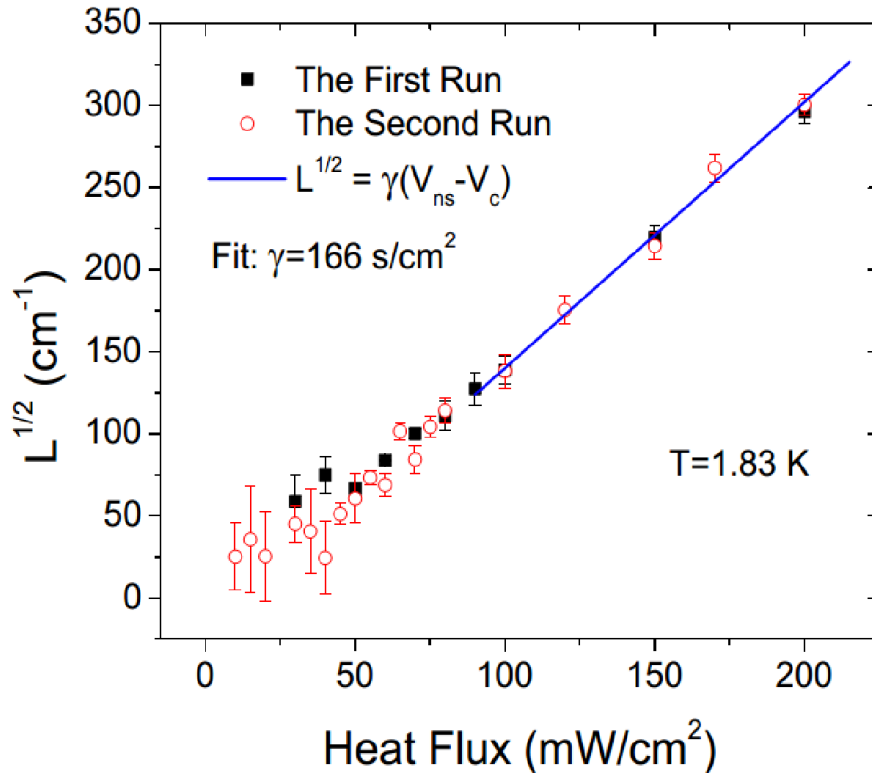
Recently, Yui and Tsubota [64] simulated the behavior of quantized vortices with a prescribed tail-flattened normal fluid velocity profile in the thermal counterflow. Their simulation results suggested that there was no abrupt jump in vortex line density at the transition from tail-flattened flow to turbulent flow, which agrees with our experimental observations.

However, none of the above-discussed simulations are self- consistent. These simulations of quantum turbulence are based on prescribed forms of normal fluid flow without taking into account the back reaction from the vortex tangle. Due to the wide range of scales in the problem, self-consistent methods are challenging to develop. More recently, Khomenko et al. [65] studied the back-reaction of the quantized vortices on the mean laminar normal fluid velocity profile in the TI state of thermal counterflow. Their results showed that the normal fluid velocity profile became flatter in the center of the channel. Their simulations were set up between two parallel plates with boundary conditions that are different from those in our experiment. In another related study, Galantucci et al. [66] performed two-dimensional, self-consistent, coupled numerical simulations of He II thermal counterflow in a channel. Taking into account the back reaction of the superfluid vortices on the normal fluid and the presence of solid boundaries, their model simulated the normal fluid and superfluid velocity profiles in the channel, predicting the tail flattened normal fluid velocity profile that is observed in our experiment.

3.4 Fully developed turbulent flow

3.4.1 Experimental results

We also conduct experiments in the fully developed turbulent flow. The drift time that we typically use is around 10-20 ms, and 30-200 images are collected for a given heat flux and temperature. Figure 3.9 shows the temperatures and heat fluxes at which we conduct our measurement. By averaging these line images, we can calculate the local mean and standard deviation of the velocity component across the channel. Figure 3.10 shows an example at 1.65 K (the results are similar at other temperatures). A spatially non-uniform profile of mean normal fluid velocity is observed, which is more obvious for the high heat flux case (Figure 3.10(a)). Its fluctuation, shown in Figure 3.10(b), is more or less flat near the center of the channel. Both the mean velocity and the standard deviation increase when the applied heat flux increases. The results at other temperatures and heat fluxes are quite similar.
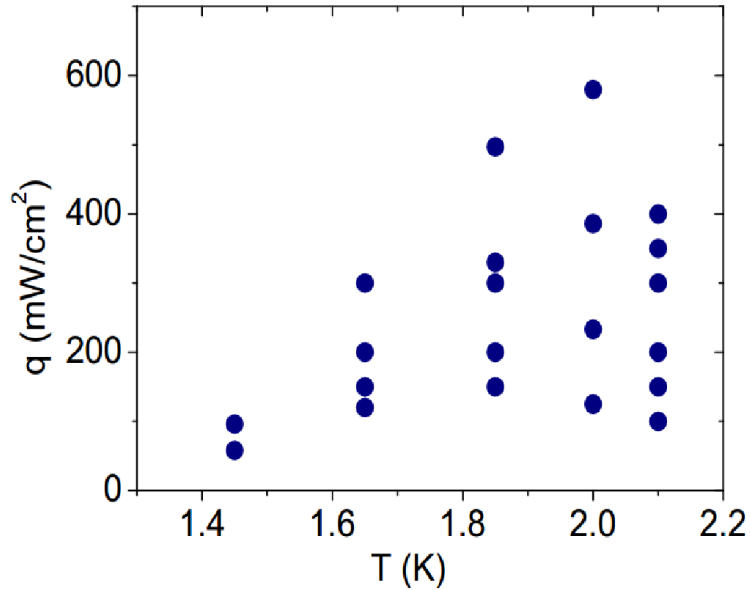
Figure 3.9 Temperatures and heat fluxes at which measurements take place.
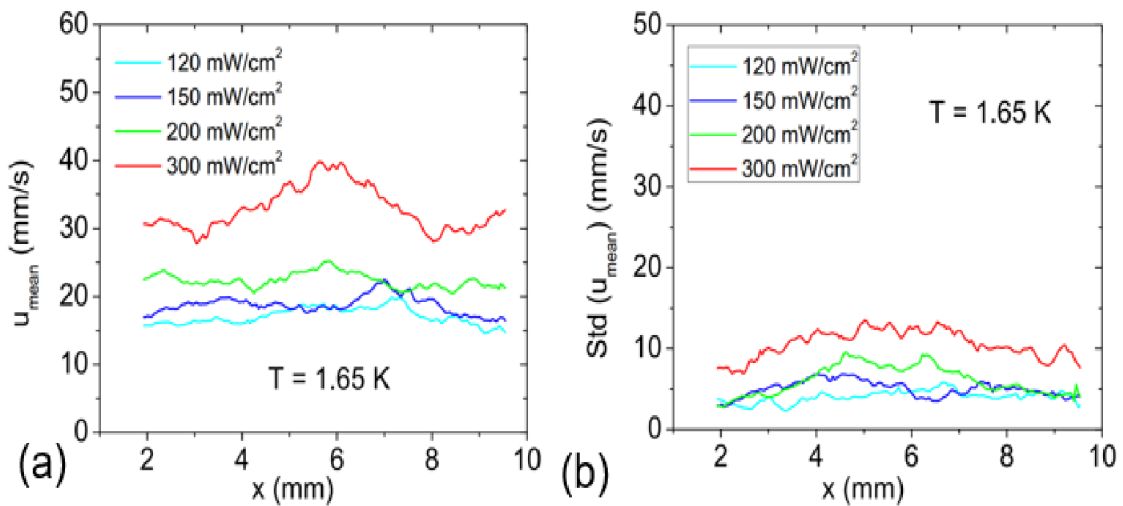
Figure 3.10 Spatial profile of the mean normal fluid velocity and turbulent fluctuations across the channel obtained at 1.65 K for various heat fluxes.

A molecular line can be divided into (e.g.) 50 segments, and the center position of each segment is determined with a Gaussian fit of its fluorescence intensity profile. Then, the velocity of each segment is obtained using the displacement divided by the drift time. The analysis of 200

images using this method generated 10000 velocity samples at a given heat flux, which is sufficient to produce a plot of the turbulence velocity probability density function (PDF). The results are shown in Figure 3.11. In each case, the red line represents a Gaussian function, and it is clear that the velocity PDF, with a given heat flux and temperature, exhibits a Gaussian distribution. This result is different from the observations in typical PTV experiments using hydrogen particles. In the early experiments, conducted by Paoletti et al. [25], power law tails of the form u^3 in the velocity PDFs were observed. These high-velocity tails were interpreted as micron-sized particles that were trapped on vortex lines experiencing a high velocity due to reconnections between quantized vortices. Recent experiments from Skrbek's group [28] also showed the u^3 tails in the PDFs of velocity for micron-sized deuterium particles in counterflow without distinguishing between trapped and up-trapped particles. They proposed that the results could also be obtained without vortex reconnections. The injected particles getting close to a quantized vortex line could experience a high velocity field, which could account for the observed u^3 tails in the velocity PDFs. Our excimer molecules remain un-trapped and may scatter by quantized vortices above $1\ K$. However, this scattering takes place in a very short time, and any momentum gained from such a scattering quickly loses to the normal fluid due to a very small viscous relaxation time [40]. Nevertheless, an excimer molecule entrained by the normal fluid can gain high velocity as it gets close to a quantized vortex. However, this only occurs on a time scale that is much less than the drift time (typically $\sim 10\ ms$) that we use to probe the fluid. Therefore, we do not expect to see anything other than a classical Gaussian distribution in the velocity PDFs. Based on the Gaussian fits shown in Figure 3.11, the mean normal fluid velocity u_{mean} and velocity fluctuation $\overline{\left(\Delta u^2\right)}^{1/2} = \left(\overline{\left(u - u_{mean}\right)^2}\right)^{1/2}$ can be determined.

In Figure 3.12, we show the mean normal fluid velocity in the fully developed turbulent flow as a function of the heat flux at different temperatures. The dashed lines are the velocities given by equation (1.14). The good agreement suggests that our tracer molecules are entrained by the normal fluid component in the fully-developed turbulent flow. The observed turbulence intensity in the normal fluid, defined as $\overline{\left(\Delta u^2\right)}^{1/2} \big/ u_{mean}$, is shown as a function of heat flux at different temperatures in Figure 3.13(a). This turbulence intensity is much larger than that observed in a classical turbulent channel flow [Davidson2004], which is about 5 %. However, the turbulence

intensity would be smaller if the physically-relevant ratio were to involve not u_{mean} but rather v_{ns}.

Additionally, the observed turbulence intensity only weakly depends on the heat flux shown in Figure 3.13(a). The dashed line denotes the averaged value, and Figure 3.13(b) shows the averaged turbulence intensity as a function of temperature. The reason for this intriguing large and temperature-dependent turbulence intensity is still unknown, which calls for future theoretical and numerical study.
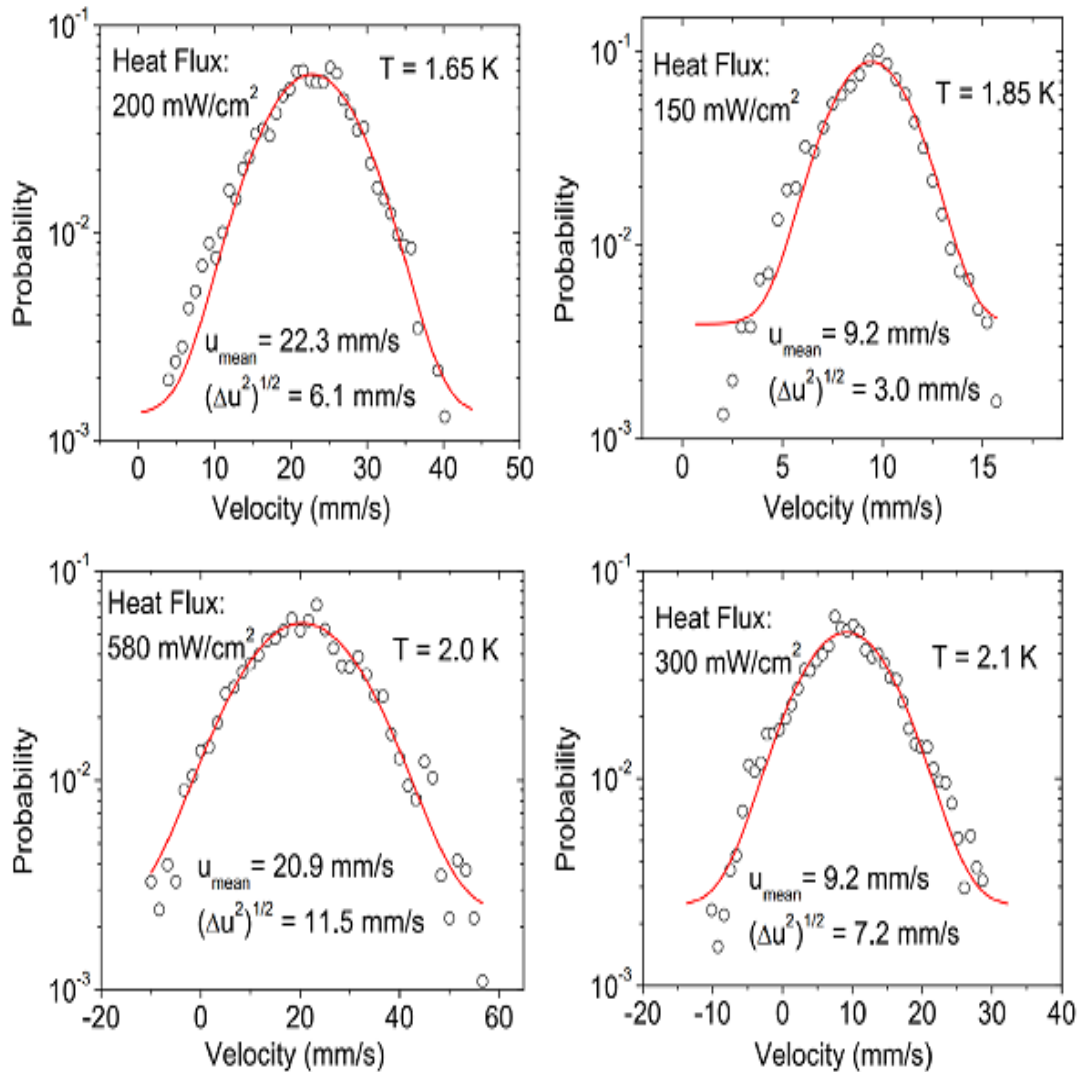
Figure 3.11 The calculated probability distribution of the velocities in turbulent normal fluid in steady state thermal counterflow at temperatures 1.65, 1.85, 2.0 and 2.1 K. The red solid curves represent the Gaussian fits to the data.
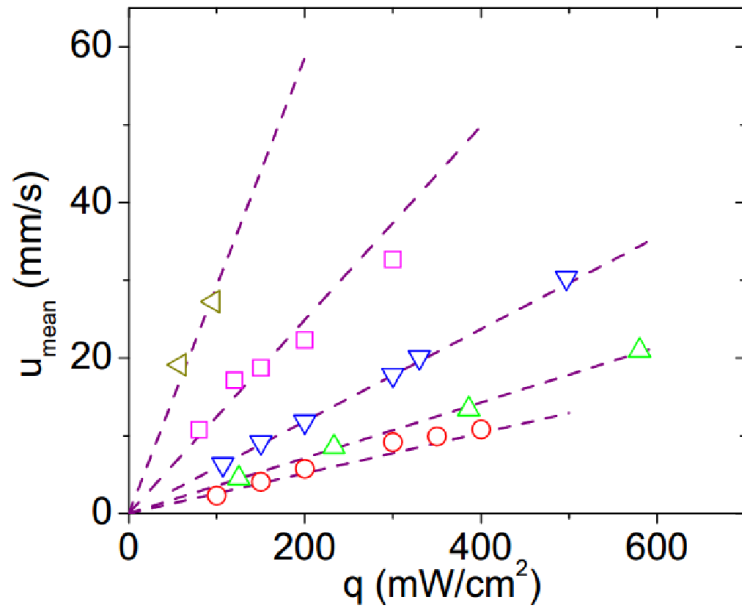
Figure 3.12 Measured normal fluid velocity averaged across the channel compared with expected normal fluid velocity (dashed lines) for temperatures 2.1, 2.0, 1.85, 1.65 and 1.45 K (lines from lowermost to uppermost).
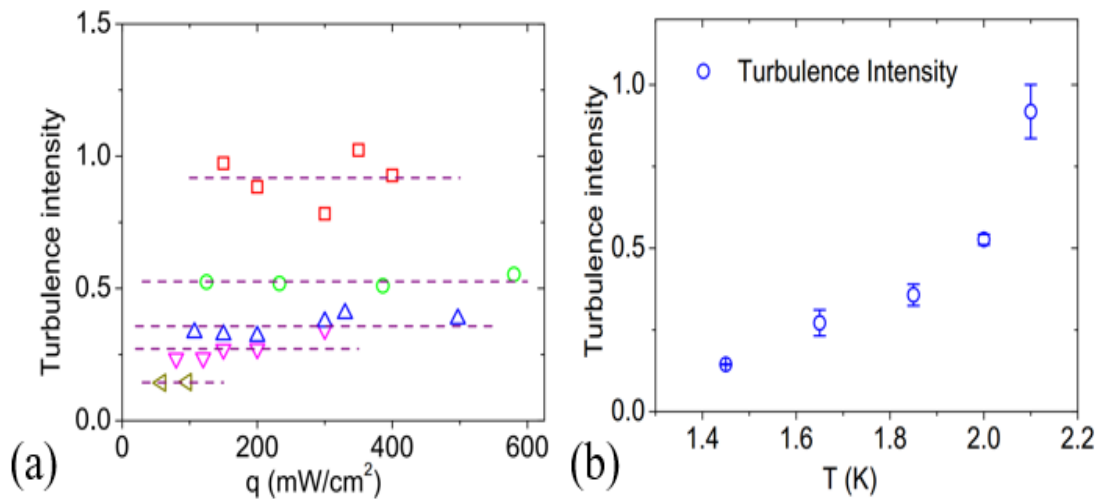
Figure 3.13 (a) Measured turbulence intensity as a function of applied heat flux for temperatures 1.45, 1.65, 1.85, 2.0, and 2.1 K (from bottom to top). The dashed line represents the averaged value. (b) Averaged turbulence intensity as a function of temperature. Error bars indicate the standard deviation.

42

In order to characterize the normal fluid turbulence, we use our observations to obtain some information about the second-order transverse structure function. By subtracting the mean flow velocity, we can calculate the second-order transverse structure function:

$$S_2^\perp(R,r) = \overline{\left\langle (u(R+r/2) - u_{mean}(R+r/2)) - (u(R-r/2) - u_{mean}(R-r/2)) \right\rangle^2}, \qquad (3.3)$$

where $u_{mean}(R+r/2)$ represents the ensemble averaged velocity at location $R+r/2$. It can be shown, further, that if the energy spectrum of turbulence in the cascade-length scale range follows a power law $\widetilde{E}(k) \propto k^{-n}$ with $1 < n < 3$, the second-order structure function also has a power law, with the form $S_2(R,r) \propto r^{n-1}$ [67]. Furthermore, the longitudinal and transverse second order structure functions are related by the equation [67]

$$S_2^\perp(R,r) = S_2^\|(R,r) + \frac{r}{2}\frac{\partial S_2^\|(R,r)}{\partial r}, \qquad (3.4)$$

This equation indicates that if the longitudinal second order structure function has a power law form, the transverse second order structure function should have the same power law form. As a consequence, if the turbulence energy spectrum has a form of $\widetilde{E}(k) \propto k^{-n}$, we can expect to see $S_2^\perp(R,r) \propto r^{n-1}$. Specifically, for a classical homogeneous isotropic turbulence that obeys Kolmogorov scaling ($n = 5/3$), we expect to see $S_2^\perp(R,r) \propto r^{2/3}$ in the inertial range [68].

We begin by analyzing the velocity $u(R+r/2)$ and $u(R-r/2)$ for two segments that are symmetrically located around the channel center axis (case 1) and then perform an ensemble average of 200 single shot images. The result for 330 mW/cm^2 at 1.85 K is shown in Figure 3.14. For $r < \sim 2$ mm, the data points exhibit a power law behavior. The data (red triangles) all fall along the $r^{1.27}$ curve (black dashed line) indicated in Figure 3.14. We also compute $S_2^\perp(R,r)$ by moving the reference location R (shown in Figure 2.13) to a different position along the tracer line and then perform an ensemble average (case 2). The result is shown as the blue circles in Figure 3.14. The data points almost follow the same power law behavior. This suggests that the calculated second-order transverse structure function does not seem to depend on the reference location R.

It is also necessary for us to check the reliability of our data analysis with respect to the number of sample images for averaging. For some cases, shown in Figure 3.9, only 30 image samples are collected initially. For comparison, we take another 200 images in a different run. For

instance, Figure 3.15 shows the averaged mean normal fluid velocity profile and the fluctuation across the channel for heat flux 330 mW/cm^2 at 1.85 K. The averaged profile, with more image samples, is smoother than the one with fewer images for averaging. Overall, the two profiles obtained with two sets of sample images agree very well. The comparison for $S_2^{\perp}(R,r)$ is shown in Figure 3.16, with results that almost overlap with each other. Therefore, a data analysis based on an averaging of 30 images or more should be reliable.
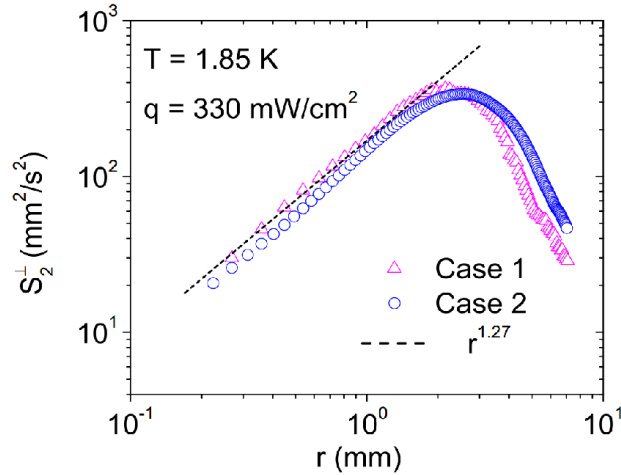
Figure 3.14 The observed second-order transverse structure function of the normal fluid turbulence in steady state counterflow with heat flux 330 mW/cm^2 at 1.85 K. Case 1 and Case 2 are discussed in the text.
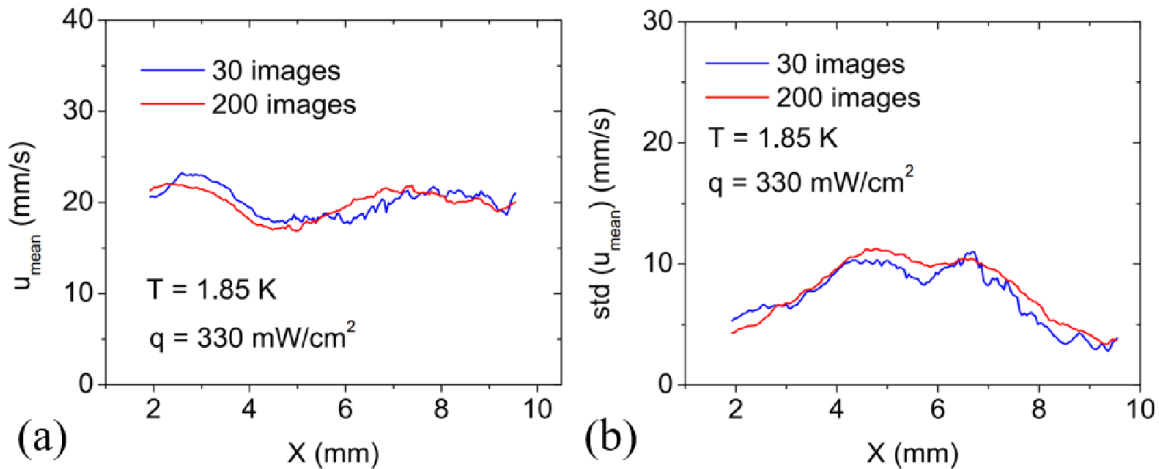
Figure 3.15 (a) Spatial profile of the mean normal fluid velocity obtained from an ensemble of 30 images (red curve) and 200 images (blue curve). (b) Corresponding turbulent fluctuations (standard deviation) across the channel.

44
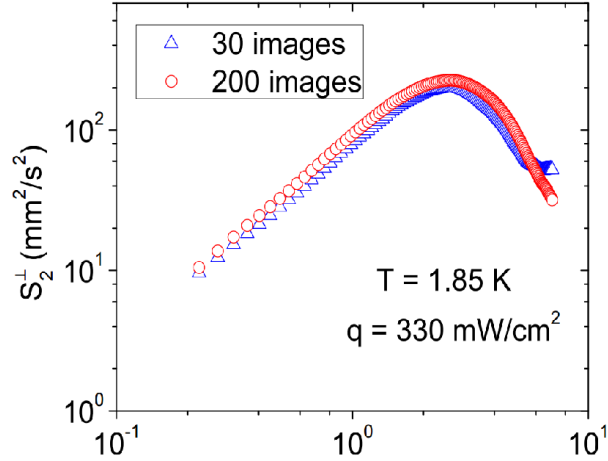
Figure 3.16 $S_2^\perp(R,r)$ obtained from 30 images (blue triangles) and 200 images (red circles). The results are almost overlapping with each other, especially in the cascade range.

We show, in Figure 3.17, the observed $S_2^\perp(R,r)$ for various heat fluxes at 1.85 and 2.10 K. The fitting range starts from around 0.2 mm and the red-dashed line represents the upper boundary. The determined power index n for a known heat flux and temperature (Figure 3.9) is shown in Figure 3.18. The exponent n leads to an energy spectrum $\widetilde{E}(k) \propto k^{-(n+1)}$. The figure shows that the observed energy spectrum of the normal fluid turbulence in thermal counterflow deviates from the Kolmogorov energy spectrum as the heat flux is increased.
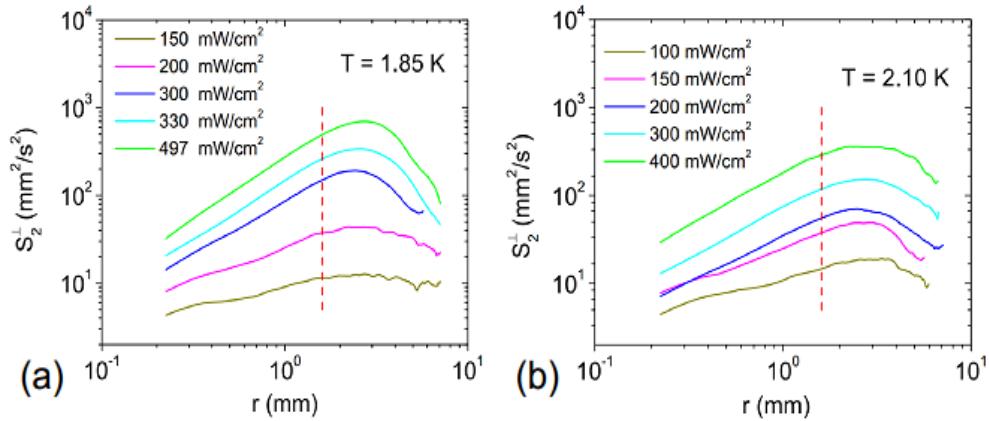
Figure 3.17 (a) The observed second order transverse structure function $S_2^\perp(R,r)$ of the normal fluid turbulence in steady state counterflow at 1.85 K. (b) $S_2^\perp(R,r)$ of the normal fluid turbulence in steady state counterflow at 2.10 K. The dashed line represents the upper limit of the fitting range.

45
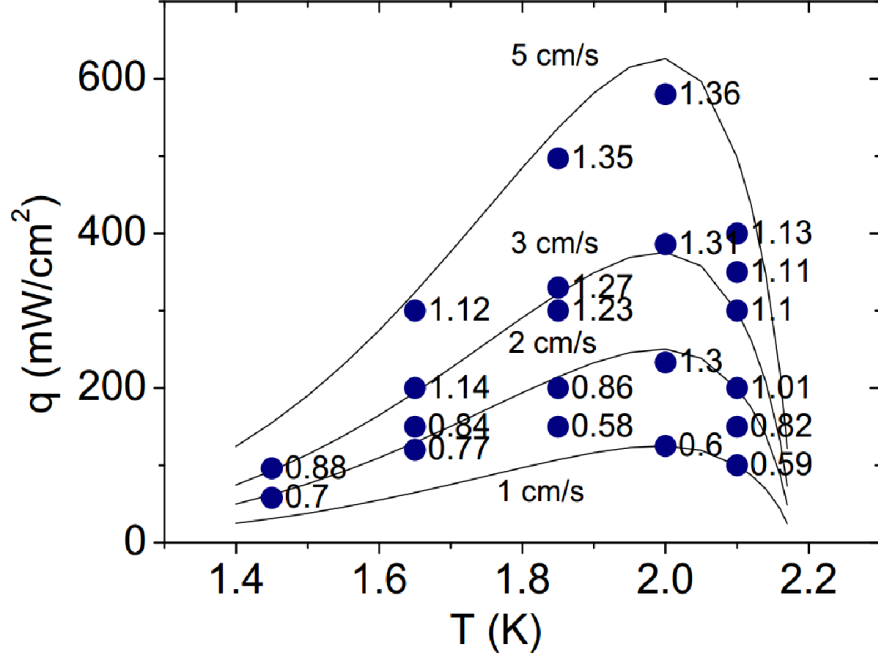
Figure 3.18 The observed power index of $S_2^{\perp}(R,r)$ in a cascade range for known heat fluxes and temperatures. The solid curve represents a constant counterflow velocity.

3.4.2 Discussion

In classical high Reynolds number homogeneous isotropic turbulence, turbulent energy is injected at a large length scale and flows at a rate of ε per unit volume in a Richardson cascade to smaller and smaller length scales until it is dissipated by viscosity in eddies for which the Reynolds number is of order unity. The energy spectrum in such a cascade has, approximately, the Kolmogorov form $\widetilde{E}(k) = C\varepsilon^{2/3}k^{-5/3}$ [68]. As we have explained, in steady state counterflow turbulence, energy is injected on the scale of the vortex line spacing, l, by the mechanism identified by Schwarz. In addition, when the heat flux is high enough and the normal fluid becomes turbulent, energy must be injected on a large scale as well. The only large scale in the problem is the channel size, D, so there must be an injection of energy at both length scales l and D. Energy injected at scale l is confined to the superfluid component and is dissipated on a similar scale by mutual friction. Energy injected at scale D would involve two fluid components. There is a tendency for this energy to flow in a cascade to small scales, but this flow will not be free from dissipation. It has been noted that coupling on all length scales must, to some extent, break down

46

because similar eddies in the two fluid components will be continually pulled apart in counterflow turbulence, which leads to dissipation on all length scales due to mutual friction [69].

Recently, Khomenko et al. [70] investigated counterflow induced decoupling in superfluid turbulence. In a homogeneous and isotropic thermal counterflow, the normal fluid eddies (the blue solid lines) are swept by the normal fluid flow at a mean velocity V_n, and eddies in the superfluid (the red dashed lines) are swept by the superfluid component at a mean velocity V_s. The time required for an eddy to be swept by the counterflow velocity over the distance of the eddy size r' (r' is used to distinguish the eddy size from the separation distance in $S_2^\perp(R,r)$) is defined as "overlapping time", $\tau_{ol} \simeq \dfrac{r'}{v_{ns}}$. As shown in Figure 3.19, the normal fluid velocity is from left to right, and the superfluid is moving in the opposite direction. Time $t = 0$ is set when all turbulent eddies of scales R_1, R_2, and R_3 are overlapping. The time step τ is selected to be $\tau \simeq \dfrac{R_2}{v_{ns}}$. Then, the smallest eddies of scale R_1 overlap at $t = 0$ and are fully separated at $t \pm \tau$, while the largest eddy of scale R_3 are almost overlapping during time step τ. Intermediate scale eddies with size R_2 are partially overlapping over the time step. Besides the overlapping time due to the counterflow velocity, the time τ_{cor} required for the coupling of the two fluid components by mutual friction is estimated as [Vinen2002]

$$\tau_{cor} = \frac{\rho_n}{\alpha \rho \kappa L}, \tag{3.5}$$

where α is temperature-dependent dimensionless mutual friction coefficient.

Khomenko et al.'s detailed analysis has shown that, for most eddies in the relevant range of scales $D < r' < l$, when $\tau_{ol} \ll \tau_{cor}$, the strong decoupling of the two fluid components occurs, which results in effective energy dissipation due to mutual friction and significant suppression of the energy spectrum of the normal fluid turbulence. On the contrary, when $\tau_{ol} \gg \tau_{cor}$, the two fluid components get strongly coupled by mutual friction, leading to a spectrum that is more nearly of the classical Kolmogorov form.

In their theoretical model, a dimensionless "decoupling parameter" $\zeta(k)$ was introduced as the ratio of the coupling time to the overlapping time, which has the expression
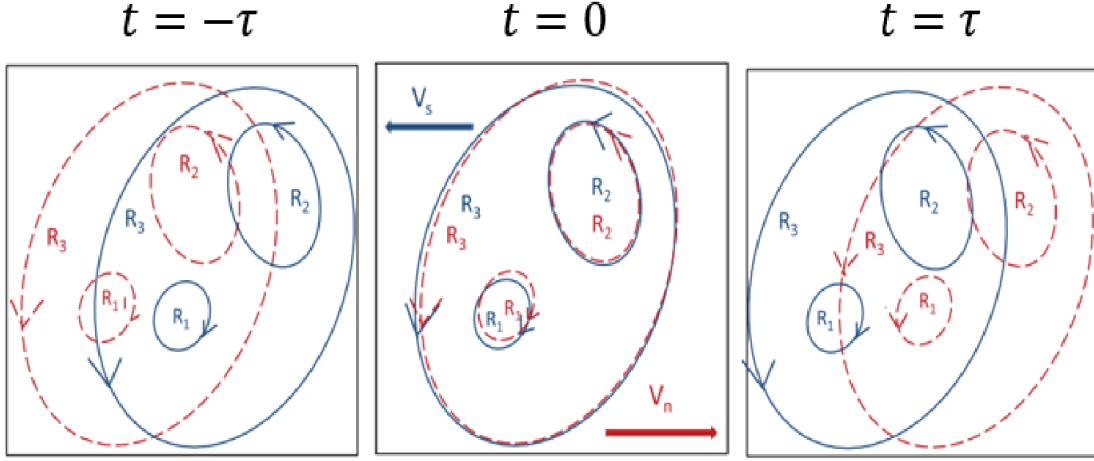
Figure 3.19 Figure reproduced from Ref [70]. Schematic showing the normal fluid eddies of scales R_1, R_2, and R_3 swept by the normal fluid velocity V_n together with quantized vortex tangle (red dashed lines) that are swept by the superfluid component with mean velocity V_s. They are at times $t = -\tau$, $t = 0$ and $t = \tau$. The time step τ is selected to be $\tau \simeq R_2 / v_{ns}$.

$$\zeta(k) \simeq \frac{\tau_{cor}}{\tau_{ol}} \simeq \frac{k}{\alpha \kappa \gamma^2 v_{ns}}, \tag{3.6}$$

where k is the wave number. It is clear that $\zeta(k)$ is inversely proportional to v_{ns} for a given eddy size. We would expect to see stronger coupling between two fluids as the counterflow velocity increases. Especially if the two fluid components are fully coupled, the energy spectrum of the normal fluid turbulence would show a classical Kolmogorov form. However, our second order transverse structure function calculation, shown in Figure 3.16, suggests a different trend. As the heat flux is increased, the determined power index of the second-order transverse structure function deviates more strongly from the Kolmogorov form ($n = 2/3$). The decoupling parameter $\zeta(k)$ can also be determined in our experiment. Since the data points in $S_2^\perp(R,r)$ exhibit a power law behavior on a length scale less than 2 mm, turbulent eddies with size $r' = 1$ mm are selected as an example in our calculation. As shown in Figure 3.20, the power index decreases almost linearly as $\zeta(k)$ increases. The results suggest a strong decoupling between two fluids for $\zeta(k) \ll 1$, in apparent disagreement with the theory. Our observations show that our current understanding of the thermal counterflow remains seriously incomplete, which calls for more experimental, numerical, and theoretical study.

48
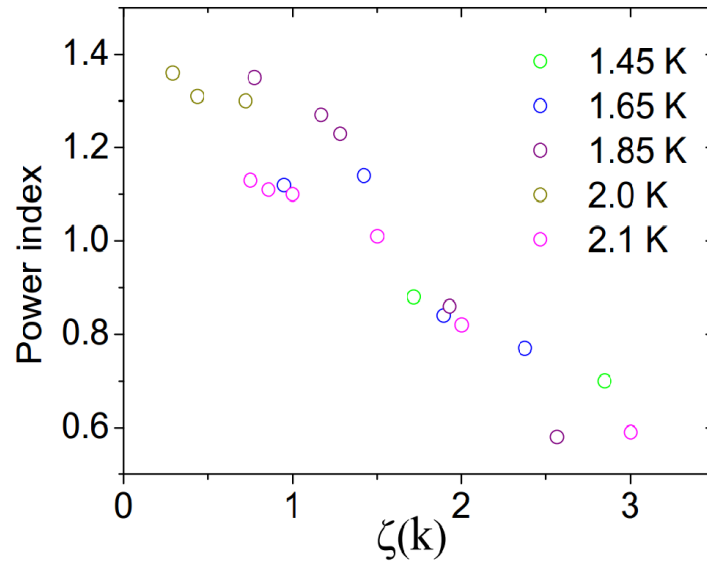
Figure 3.20 The observed power index, at temperatures 1.45, 1.65, 1.85, 2.0 and 2.1 K, as a function of the dimensionless decoupling parameter $\zeta(k)$ based on the turbulent eddies with size $r^{'} = 0.1\ cm$.

CHAPTER 4

DECAY OF COUNTERFLOW TURBULENCE

The Chapter summarizes recent experimental work on the decay of thermal counterflow. Vinen's model predicts $L(t) \propto t^{-1}$ decay behavior after the heater is switched off. However, past observation of vortex line density decay shows an obvious discrepancy with this prediction. We proposed a new phenomenological model based on our flow visualization measurement and vortex line density measurement. This model predicts the $L(t)$ decay behavior that agrees well with our experimental observations.

4.1 Overview

According to Vinen's model (equation (3.1)), when the steady state counterflow velocity v_{ns} is suddenly changed to be zero by switching off the heat current, the equation can be expressed as

$$\frac{dL}{dt} = -\frac{\kappa}{2\pi} \chi_2 L^2 , \tag{4.1}$$

From this equation, one can easily derive that the decay of vortex line density can be described by

$$L = \frac{L_0}{1 + t / \tau_1} , \tag{4.2}$$

where L_0 is the initial vortex line density in steady state thermal counterflow and $\tau_1 = 2\pi / \chi_2 \kappa L_0$. Vinen first studied the decay of counterflow turbulence by measuring the vortex line density as a function of time after switching off the heater. He observed an initial rapid decay in agreement with equation (4.2), followed by a slower decay that cannot be described by Vinen's model [13]. Schwarz and Rozen then studied this problem experimentally and theoretically, and argued that the slow decay regime can be interpreted in terms of a state of coupled turbulence involving not only the quantized vortex tangle, but also random superfluid and normal fluid motion, the whole system decaying in a rate controlled by the normal fluid viscosity [71,72].

Later, Skrbek et al. [73] conducted more systematic experiments on the decay of counterlfow turbulence using second sound attenuation method. Their results are shown in Figure 4.1. It was observed that after the heat current is switched off, the quantized vortex line density decays with

a power law behavior of t^{-1} at short decay times, but subsequently there is a "bump" (or at least a point of inflexion), followed by $t^{-3/2}$ power law behavior. The $t^{-3/2}$ behavior is interpreted as a consequence of the decay of a quasiclassical coupled turbulence with a classical Kolmogorov spectrum [74]. The quasiclassical behavior of He II is due to a strong coupling of the two fluids by mutual friction at length scales greater than the mean separation of the quantized vortex lines [75]. The normal-fluid eddies are on average matched by polarized vortex filaments in the superfluid [76,77]. As a consequence, the coupled fluids behave at large scales like a single-component viscous fluid. At small scales, due to the viscous dissipation in the normal fluid and the discrete vortex-line structure in the superfluid, the flows in the two fluids become decoupled. Mutual friction dissipation sets in at these small scales.

However, the underlying mechanism for the appearance of the bump and the switching to the $t^{-3/2}$ decay remains unknown. Barenghi et al. [78, 79] proposed that the bump is due to depolarization of the vortex tangle after the heater is switched off. Their model suggests that the vortex tangle induced by the thermal counterflow is polarized by the normal fluid perpendicular to the flow direction (flow is along vertical direction in Figure 4.2). A snapshot of the polarized vortex tangle in steady state thermal counterflow is shown on the left in Figure 4.2. Due to the sine square law [18], such polarized quantized vortices that are parallel to the second sound propagation direction do not contribute the excess attenuation. After the heater is off, this polarization gradually decreases and the vortex loops start turning around randomly (right in Figure 4.2). As a consequence, the vortex line density measured by the transverse second sound signal can increase.
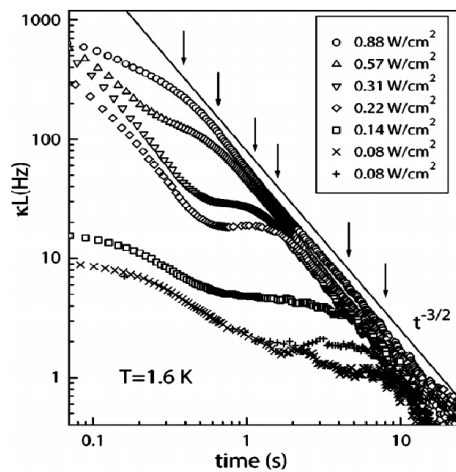
Figure 4.1 Figure reproduced from Ref [73]. The decay of vortex line density in counterflow turbulence at 1.65 K.
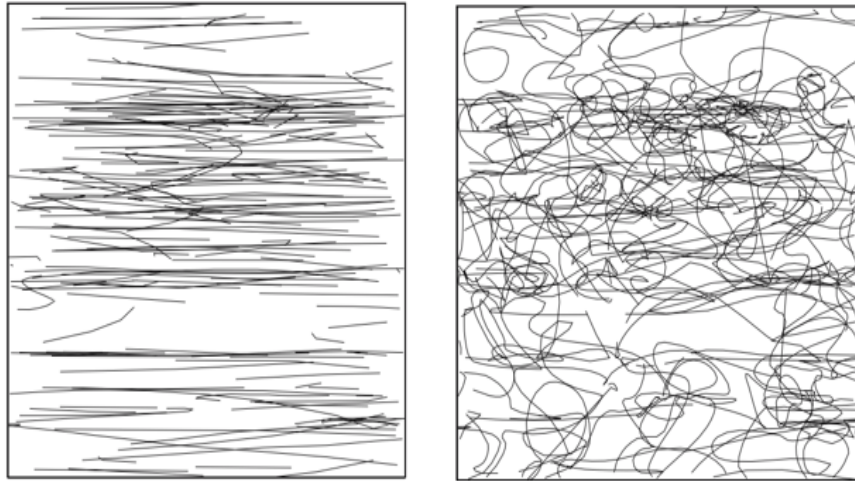
Figure 4.2 Figure reproduced from Ref [78]. Side view of the computed vortex tangle in the steady state (left) and at 0.1 s during the decay stage (right). In steady state thermal counterflow, the vortex lines are polarized perpendicular to the flow direction (flow is along vertical direction). The vortex loops start turning around randomly after the heater is switched off.

The theoretical model proposed by Barenghi et al. does not consider the possible role of the normal fluid turbulence before the heat current is switched off. The bump and $t^{-3/2}$ are thought to be characteristic of all decays of thermal counterflow turbulence, in disagreement with our recent observations, which will be discussed in subsequent sections. A new theoretical model has been proposed to explain the observed complex $L(t)$ behavior, which accounts well for our experimental observations.

4.2 Experimental study

4.2.1 Visualization of the decay of thermal counterflow

In the decay of counterflow turbulence measurement, the experimental setup is the same as that used in steady state thermal counterflow experiment. In a typical experiment, we maintain a steady state counterflow for over 20 s and then switch off the heat current. After a certain decay time, we send in femto-second laser pulses to create the tracer line. The tracer line follows the motion of the normal fluid component with a certain drift time, and is then imaged with imaging laser pulses. Figure 4.3 shows typical images of the He_2^* tracer lines in decaying counterflow

measurement with heat flux 150 mW/cm^2 at 1.65 K. It is obvious that the distortion of the tracer line becomes weaker with time. To resolve small distortion of an excimer line at long decay times, a slightly longer drift time (around $30 \sim 40$ ms) is used. We can reliably resolve the tracer line deformation for the decay time from around 10 ms to 10 s.

For a given heat flux q, we normally repeat the experiment 200 times and analyze the 200 images acquired at every decay time to produce velocity probability functions (PDFs). Typical results for an initial heat flux of $q = 426$ mW/cm^2 at 1.65 K are shown in Figure 4.4. These velocity PDFs can be well fit with Gaussian functions, which allows us to determine the time evolution of both the mean flow velocity u_{mean} and the streamwise root mean square velocity fluctuation Δu. The time taken for u_{mean} to decay to nearly zero is about 100 ms at $q = 426$ mW/cm^2 and shorter at lower heat fluxes. The measured decay of Δu for typical initial heat fluxes is shown in Figure 4.5. We observe that, right after the heater is switched off, the decay of Δu is very slow and nearly flattens off at relatively small decay times. At large decay times, $\Delta u \propto t^{-1}$ and hence the turbulence kinematic energy density $1/2 \Delta u^2 \propto t^{-2}$. This late decay behavior is in accordance with the decay of a quasiclassical turbulence with a Kolmogorov spectrum [74], which will be discussed in Section 4.3.
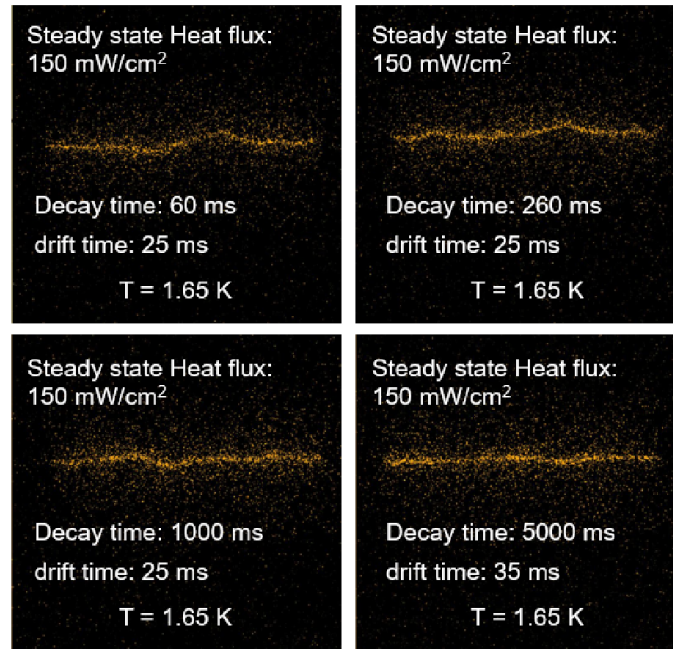
Figure 4.3 Typical images obtained in decaying counterflow at 1.65 K. The steady state heat flux is 150 mW/cm^2.
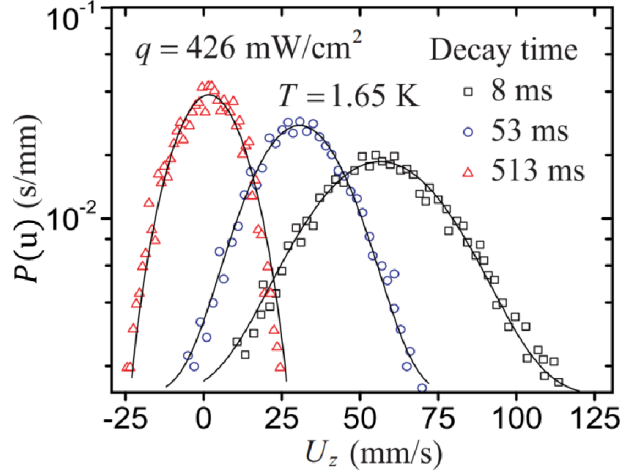
Figure 4.4 Velocity PDFs in decaying counterflow at 1.65 K for a steady state heat flux of 426 mW / cm^2. The solid curves present Gaussian fits to the data.
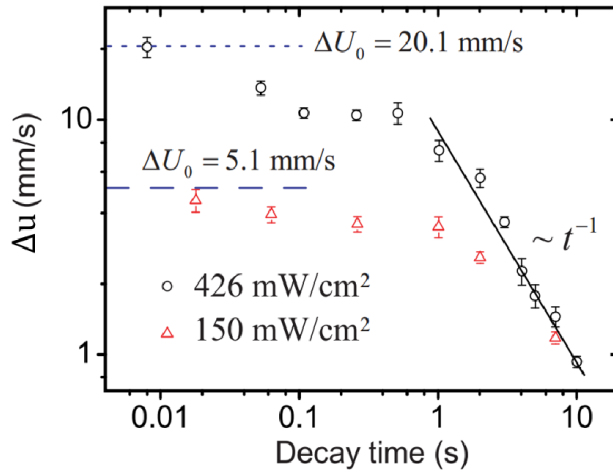
Figure 4.5 Streamwise velocity fluctuation Δu determined from the Gaussian fits of the velocity PDFs. The dotted and the dashed horizontal lines represent the Δu levels in the steady state counterflow.

The energy spectrum of the coupled turbulence can be directly probed in our experiment by calculating the second order transverse structure function $S_2^{\perp}(R,r)$. The time evolution of the calculated $S_2^{\perp}(R,r)$ for initial heat flux 426 mW / cm^2 at 1.65 K is shown in Figure 4.6 (a). We observe that $S_2^{\perp}(R,r) \propto r^n$ below a few millimeters. This exponent n leads to an energy spectrum $\widetilde{E}(k) \propto k^{-(n+1)}$ [68]. The observed variation of n is shown in Figure 4.6 (b), which reveals that the

54
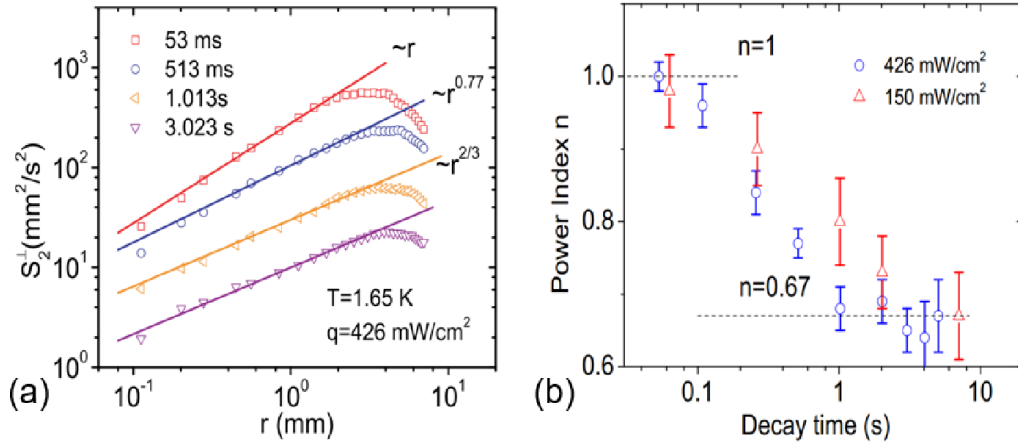
Figure 4.6 (a) The calculated second order transverse structure function at different decay times in decaying counterflow with an initial heat flux of 426 mW/cm^2. (b) Measured exponent n of the second order transverse structure function $S_2^{\perp}(R,r) \propto r^n$.

coupled turbulence evolves from a nonclassical form at small decay times with a spectrum close to that in steady state to a quasiclassical turbulence at large decay times with a Kolmogorov spectrum ($n = 2/3$). Similar behavior of $S_2^{\perp}(R,r)$ are observed at other temperatures.

4.2.2 The observed decay of vortex line density

The vortex line density $L(t)$ in decaying counterflow has been measured using the 2nd sound attenuation method. The way how we determine the vortex line density in steady state thermal counterflow does not work for the decaying counterflow measurement. Since our data acquisition speed is around 4 ms per Hz, a complete spectrum scan over the whole resonance peak regime takes about 4 s. However, the counterflow turbulence decays very fast. In addition, since the 2nd sound velocity is temperature dependent, even a small temperature fluctuation can result in resonance peak shift (typically $1 - 2$ Hz). Our solution is to scan a few Hz (typically ~ 8 Hz) centered around a selected resonance peak during the decay. An example is shown in Figure 4.7(a). Hence, the resonance peak value $\overline{A}$ in equation (2.5) can be reliably measured in every 32 ms. Figure 4.7(b) shows a typical trace of $\overline{A}$ in the decaying counterflow measurement for heat flux 426 mW/cm^2 at 1.65 K. When we turn on the heater current, 2nd sound signal is attenuated due to quantized vortices. After the heater is switched off, the amplitude of the resonance peak reverts

55

to the unattenuated value $\overline{A_0}$ before the heater is on. To determine the unattenuated amplitude of the peak height $\overline{A_0}$ and width Δf_0, we scan over 1000 Hz centered around the resonance peak before and after every decaying counterflow measurement. In order to suppress the noise in measuring vortex line density, we repeat the measurement over 100 times and do the ensemble average.

The typical decay behavior of $L(t)$ at 1.65 K is shown in Figure 4.8. It is observed that, when the normal fluid is turbulent in the initial steady state before the heater is turned off (note: the normal fluid can become turbulent above a threshold heat flux ~ 60 mW/cm^2 at 1.65 K), the decay of $L(t)$ always exhibits three distinct regimes. The first regime occurs at very short decay times where $L(t)$ decays fast and in accordance with Vinen's phenomenological model (equation (3.1)). Subsequently, $L(t)$ grows with time and shows a bump structure. At large decay times, $L(t) \propto t^{-3/2}$. This $L(t)$ decay behavior agrees with past experiments conducted by Skrbek et al. [73]. However, When the initial heat flux is small such that the steady state normal fluid is in laminar flow, the measured vortex line density can be fitted very well with Vinen's form at all decay times. The same vortex line density decay behavior has been observed at other temperatures. Our observations suggest that the appearance of the bump and the $t^{-3/2}$ decay are correlated with the large-scale turbulence in the steady state. Early theories of the bump [71-72, 78-79] are not consistent with this observation.
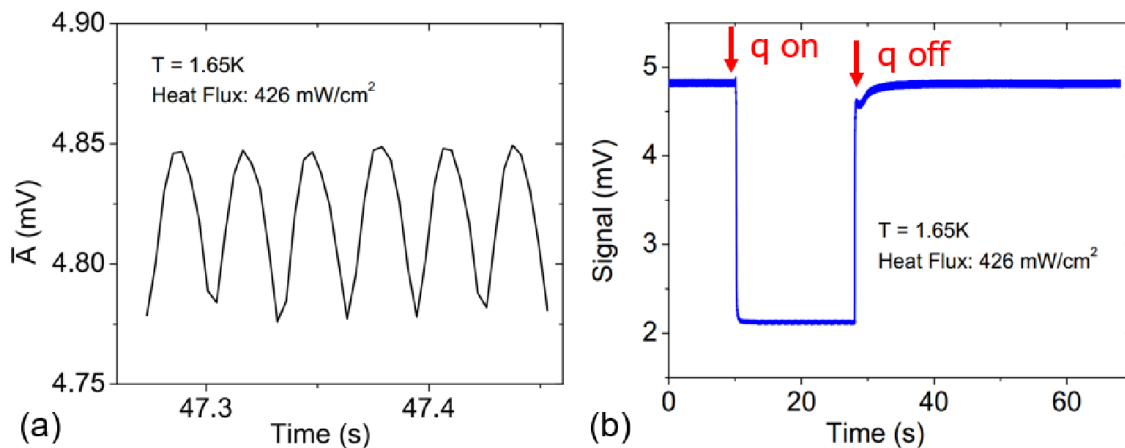
Figure 4.7 (a) Consequent peaks measured in decaying counterflow at 1.65 K. (b) A typical trace showing before and after the heater is on and off. The applied heat flux is 426 mW/cm^2.
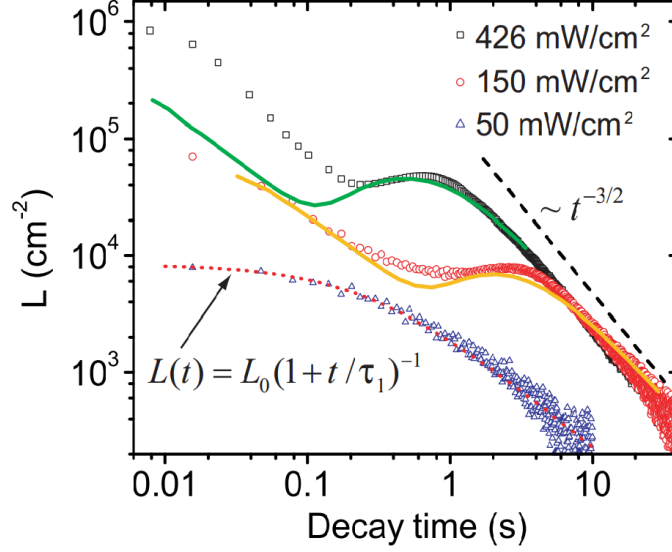
Figure 4.8 Observed decays of vortex line densities for different values of the vortex line density in the steady state at 1.65 K. The solid lines represent the theoretical predictions.

The observed vortex line density decay $L(t) \propto t^{-1}$ allows us to determine the χ_2 values. An example at 1.65 K is shown in Figure 4.9. We plot $L(t)$ in a form, $1/L$ versus t. Equation (4.2) can be re-written as

$$\frac{1}{L} = \frac{1}{L_0} + \frac{\chi_2 \kappa}{2\pi} t . \tag{4.3}$$

Then χ_2 can be determined by using a linear fit of $1/L$ as a function of t. In Figure 4.10, we show the values of χ_2 deduced from $L(t)$ decays as a function of temperature. A theory of χ_2 was proposed by Vinen and Niemela [17]. The value of χ_2 can be estimated as

$$\chi_2 = \frac{\alpha c_2^2}{2} \ln \frac{l}{a_0} , \tag{4.4}$$

where α is dimensionless parameter and can be taken from Ref [52], c_2 depends only on the temperature and can be estimated from the simulations of the steady state thermal counterflow [64], and a_0 is the vortex core parameter. This derivation is based on three assumptions [17]: 1) there is no motion of the normal fluid; 2) the vortex lines form a random tangle; 3) the use of the

57

local induction approximation is justified. The derived values of χ_2 are shown in Figure 4.10. We see that within error bars there is a good agreement with experiment.
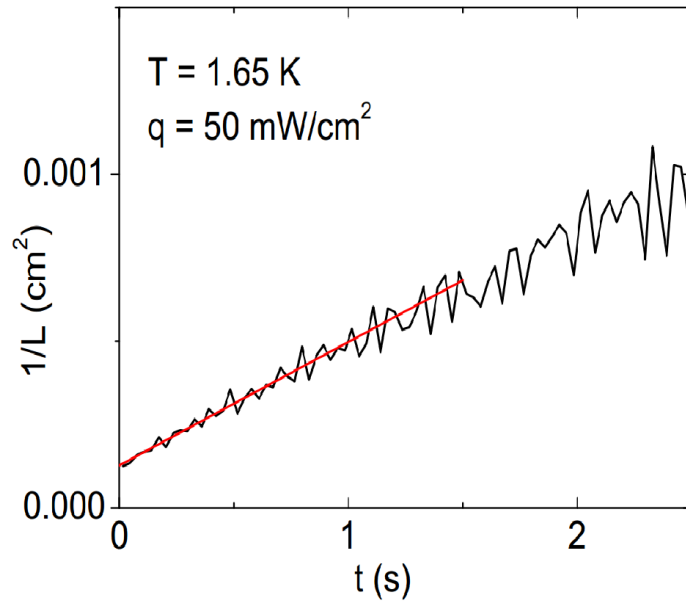
Figure 4.9 $1/L$ as a function of time with initial heat flux 50 mW/cm^2 at 1.65 K. The red line represents a linear fit to the data.
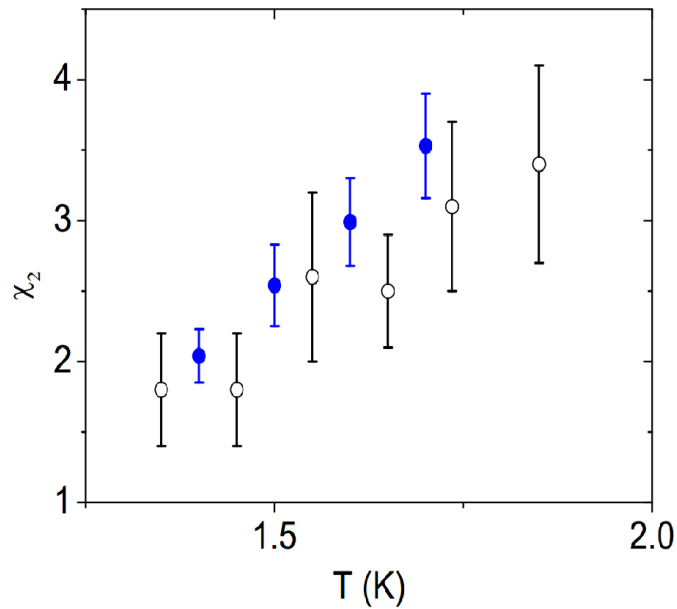
Figure 4.10 The observed (black open circles) and theoretical (blue filled circles) values of χ_2.

4.3 Theoretical model

With the aid of our flow visualization, we are able to reveal that the energy spectrum transition in the coupled turbulence is responsible for the observed bump structure in vortex line density decay. A new theoretical model has been proposed to explain the observed complex $L(t)$ behavior [33].

As we have discussed, energy is injected at both the large-scale D and the small-scale l in steady state thermal counterflow. Very soon after the heat current is switched off, the two fluids become strongly coupled on scales larger than l [17]. The time it takes to establish the coupling can be estimated by using the equation (3.4) and is typically in the range of 1-10 ms in our experiment. By analogy with the energy decay equation for classical turbulence [80], Stalp et al. proposed that the total turbulence kinematic energy per unit He II mass, $E(t)$, decays as [74]

$$\frac{dE}{dt} = -v'(\kappa L)^2 . \tag{4.5}$$

Here v' is an effective kinematic viscosity, which will be discussed in Chapter 5. Approximately, E is composed of two parts, which are E_1 that comes from the flows in the superfluid on scales at or below l associated with individual vortex lines and E_2 that represents the kinematic energy density with large scale flows in the coupled turbulence.

Following the Ref. [81], we can estimate E_1 as

$$E_1 = B(\frac{\rho_s}{\rho})\kappa^2 L , \tag{4.6}$$

where the dimensionless factor $B = \frac{1}{4\pi}\ln(l/a_0)$ is typical about unity. At the meanwhile, E_2 is given by the expression

$$E_2 = (\Delta U)^2 / 2 , \tag{4.7}$$

where ΔU denotes the root mean square velocity fluctuation of the coupled large-scale flows. Combining equation (4.6) and (4.7), equation (4.5) can re-written as

$$\frac{dE}{dt} = B(\frac{\rho_s}{\rho})\kappa^2\frac{dL}{dt} + \frac{dE_2}{dt} = -v'(\kappa L)^2 . \tag{4.8}$$

In order to derive a solution for L in decaying counterflow turbulence, let us first consider that the two fluids are coupled at large-scales (i.e. $2\pi / D < k < 2\pi / l$) with a Kolmogorov energy

59

spectrum ($\widetilde{E}(k) = C\varepsilon^{2/3}k^{-5/3}$). Then the energy transfer rate ε in the cascade regime can be estimated as

$$\varepsilon = \frac{\frac{1}{2}\Delta U^2}{\tau}, \tag{4.9}$$

where $\tau = \dfrac{D}{\Delta U}$ is the eddy turnover time. Then the large-scale turbulence kinematic energy E_2 decays as

$$\frac{dE_2}{dt} = \frac{d(\frac{1}{2}\Delta U^2)}{dt} = \varepsilon = -\frac{(\Delta U)^3}{2D}. \tag{4.10}$$

Therefore,

$$\Delta U = \Delta U_0 (1 + \frac{\Delta U_0 t}{2D})^{-1}, \tag{4.11}$$

where ΔU_0 is the value of ΔU at $t = 0$. It is clear that $E_2 = \frac{1}{2}\Delta U^2 \propto t^{-2}$ for the coupled turbulence with a Kolmogorov energy spectrum. Then the energy decay rate equation (4.8) can be derived as

$$B(\frac{\rho_s}{\rho})\kappa^2 \frac{dL}{dt} - \frac{\Delta U_0^3}{2D}(1 + \frac{\Delta U_0 t}{2D})^{-3} = -v'(\kappa L)^2. \tag{4.12}$$

What if the energy spectrum of the coupled turbulence is not a Kolmogorov form? We can write down an energy spectrum in the form

$$\widetilde{E}(k) = C[\varepsilon(k)]^{2/3} k^{-5/3}, \tag{4.13}$$

in which $\varepsilon(k)$ can be interpreted as a k-dependent energy flux. For instance, if the steady state energy spectrum has a form of k^{-2}, we would expect to see $\varepsilon(k) \propto k^{-1/2}$. This means the rate of energy transfer reaching the small scale l, instead of being equal to that at the integral scale (i.e. $k \sim 2\pi / D$), has fallen by a factor $(l / D)^{1/2}$, which is significantly less than unity.

As shown in Figure 4.6 (a), the establishment of strong coupling does not immediately have much effect on the energy spectrum of the large scale turbulence. However, there is a gradual evolution to a Kolmogorov spectrum in a time of order the turnover time of the largest eddies [82, 83]. The observed evolution of the spectrum shown in Figure 4.7 (b) for two steady state heat

fluxes is consistent with this expectation. Thus, the large-scale energy decay rate increases from nearly zero to $(\Delta U)^3 / 2D$ in a time of order the turnover time $D / \Delta U_0$. Also if we consider the fact that some energy on the large scale is dissipated in the normal fluid, the decay rate of E_2 can be estimated as

$$\frac{dE_2}{dt} = -\beta \frac{\Delta U_0^3}{2D} (1 + \frac{\Delta U_0 t}{2D})^{-3} F(t),\qquad(4.14)$$

where the function $F(t)$ rises smoothly from zero to unity in a time of order the turnover time $D / \Delta U_0$ and $\beta < 1$. It follows that

$$B(\frac{\rho_s}{\rho})\kappa^2 \frac{dL}{dt} - \beta \frac{\Delta U_0^3}{2D} (1 + \frac{\Delta U_0 t}{2D})^{-3} F(t) = -\nu'(\kappa L)^2.\qquad(4.15)$$

A discussion of the precise form of $F(t)$ is outside the scope of this thesis. The results are not very sensitive to this precise form, provided that it serves in effect to delay the transfer of energy from scale D to scale l by a time equal to the turnover time $D / \Delta U_0$. We propose

$$F(t) = \left[1 - \exp(-\frac{\Delta U_0 t}{D})\right]^2,\qquad(4.16)$$

a form that has the required property. A rigorous evaluation of β requires a more detailed theory than is presently available, and we shall therefore follow Ref. [17] and put $\beta = \rho_s / \rho$. Equation (4.15) can then be solved by numerical integration.

To compare the results of this numerical integration with experiment we need values of L_0, U_0 and ν'. L_0 is taken directly from experiment, U_0 is obtained from the observed velocity fluctuations in steady state thermal counterflow. The value of $\nu' = 4.6 \times 10^{-4}\ cm^2 / s$ at 1.65 K can be obtained by equating directly measured rate of decay of the total turbulent energy to $\nu'(\kappa L)^2$, as will be discussed in Chapter 5. With the suggested form of $F(t)$ the predicted decay $L(t)$ is then obtained and can be compared with experimental date as shown in Figure 4.8.

We see that for a steady state heat flux of 150 mW / cm^2 the agreement is satisfactory, especially in view of simplicity of the model. For the larger heat flux of 426 mW / cm^2 the predicted bump appears at a little too early a time, and, more seriously, the predicted line density

at times less than 100 *ms* were too small. However, these discrepancies can be attributed to the effect of a finite thermal time constant on the experimental results. The heat flux in the experimental channel does not fall to zero immediately after the heater is turned off, but decays in a time given by an effective thermal time constant formed from the product of the thermal resistance and thermal capacity of the helium [13,87]. Thus, the $L(t)$ decay is effectively delayed by this time constant. In the present context, this effect is most serious at the largest heat flux, where the non-linear thermal resistivity is highest, and we are confident that it is responsible for the discrepancies to which we have drawn attention.

No bump is predicted if the factor $F(t)$ is omitted; the decay is then monotonic and changes smoothly from the form predicted by Vinen's euqation to the form $t^{-3/2}$ as the decay proceeds. This situation would obtain if the large-scale turbulence were to have a Kolmogorov energy spectrum at all times; initially the decay would then obey Vinen's prediction because the line density would at first be larger than is necessary to dissipate the flux of energy in the Richardson-Kolmogorov cascade. We see then that the physical origin of the bump lies in the fact that energy from the decaying large scale eddies reaches the dissipation scale of order l at a time that is delayed, through the factor $F(t)$, by the turnover time of the large-scale eddies. The time at which the bump appears should be determined by this turnover time. Therefore, as the steady state heat flux is increased, ΔU increases and hence the turnover time $\tau = \dfrac{D}{\Delta U}$ decreases. We have indeed observed that the bump appears at shorter decay times when the heat flux is increased, in agreement with our expectation.

CHAPTER 5

EFFECTIVE KINEMATIC VISCOSITY

We studied the quasiclassical turbulence that emerges in the decay of steady state thermal counterflow in He II above $1\ K$. A reliable determination of effective kinematic viscosity v' requires the measurements of both the total turbulence energy $E(t)$ and the vortex line density $L(t)$, which has never been achieved. In our experiment, we are able to measure $E(t)$ by using our flow visualization technique and $L(t)$ via 2nd sound attenuation. We report the v' values in a wide temperature range determined from a comparison of the time evolution of $E(t)$ and $L(t)$.

5.1 Overview

Above $1\ K$, despite being a two-fluid system with many properties restricted by quantum effects, He II is observed to behave very similarly to classical fluids when a turbulent flow is generated by methods conventionally used in classical fluid research, such as by a towed grid [74] or a rotating propeller [85]. Even in a nonclassical thermal counterflow induced by an applied heat current in He II, it has been revealed that quasiclassical turbulence can emerge during the decay of counterflow after the heat current is switched off, as discussed in Chapter 4. The classical feature of He II above $1\ K$ has brought up the feasibility of using He II in classical turbulence research and for practical model testing. He II has very small kinematic viscosity that allows the generation of flows with high Reynolds numbers that can hardly be achieved with other conventional fluid materials [86]. Various projects have been launched for this purpose [81,87]. For example, the SHREK collaboration has achieved $\mathrm{Re} \sim 6\times10^{7}$ in helium Von Karman flows [87], exceeding the highest Re ever produced using compressed air in the Princeton SuperPipe experiments ($\mathrm{Re} \sim 3.5\times10^{7}$) [88]. The SHREK collaboration is now aiming at achieving $\mathrm{Re} > 10^{8}$ using He II [89]. However, the viscosity that controls the energy dissipation of the quasiclassical turbulence above $1\ K$ is not the normal fluid viscosity but instead an effective kinematic viscosity v' that accounts for both the viscous dissipation in the normal fluid and the mutual friction dissipation at small scales. The precise value of v' is critical in the design of these He II based quasiclassical turbulence experiments. Furthermore, making reliable measurements of the v' values will be

valuable for testing various theories about the dissipation mechanism in He II [17,18,74], which will be fundamentally important in advancing our knowledge of quantum turbulence.

As discussed in Chapter 4, the total turbulence kinetic energy per unit He II mass $E(t)$ in quasiclassical turbulence, decays as

$$\frac{dE}{dt} = \frac{dE_1}{dt} + \frac{dE_2}{dt} = B(\frac{\rho_s}{\rho})\kappa^2 \frac{dL}{dt} + \frac{dE_2}{dt} = -v'(\kappa L)^2 . \tag{5.1}$$

For quasiclassical turbulence in He II, E_2 is much larger than E_1 [75]. Stalp et al. neglected the E_1 contribution at larger decay times in decay of grid turbulence and assumed: (1) the size of the energy containing eddy is saturated by the channel width D; and (2) the coupled turbulence has a classical Kolmogorov energy spectrum that extends to all scales. Based on these two hypotheses, E can be estimated as

$$E(t) = \int_{2\pi/D}^{\infty} C\varepsilon(t)^{2/3} k^{-5/3} dk = \frac{3}{2} C\varepsilon(t)^{2/3} (\frac{2\pi}{D})^{2/3} , \tag{5.2}$$

where $C = 1.5$ is the Kolmogorov constant. Then we can get

$$\varepsilon(t) = \frac{dE}{dt} = C\varepsilon(t)^{-1/3} (\frac{2\pi}{D})^{2/3} \frac{d\varepsilon}{dt} , \tag{5.3}$$

Integrating equation (5.3) leads to

$$\varepsilon \simeq 27C^3 (\frac{2\pi}{D})^2 t^{-3} . \tag{5.4}$$

It follows that

$$E(t) \simeq \frac{27C^3 D^2}{2(2\pi)^2} t^{-2} . \tag{5.5}$$

As a consequence, from equation (5.1) $L(t)$ at large decay times can be derived as [74].

$$L(t) \simeq \frac{D(3C)^{3/2}}{2\pi\kappa\sqrt{v'}} t^{-3/2} . \tag{5.6}$$

These hypotheses are, to some extent, supported by the observed $L(t) \propto t^{-3/2}$ behavior at large decay times in their grid turbulence experiment. The value of v' was then determined by fitting the measured $L(t)$ using equation (5.6) [91,92]. This method was later used by other groups for estimating v' in decaying counterflow and decaying co-flow in a channel [92,93]. Nevertheless, in all these studies the v' values obtained by using equation (5.6) are indeed dubious,

as discussed by Zmeev et al. [41]. There is no evidence showing that the energy containing eddy size must be the same as the channel width D. Although intuitively they should not be too different, any possible difference can result in significant change in the fitted v' values since $v' \propto D^2$ according to equation (5.6). Furthermore, if there is indeed a Kolmogorov spectrum, this spectrum must break down near the cutoff scale D. According to equation (5.1), a reliable determination of v' for quasiclassical turbulence in He II can be made only if one can measure directly both $E_2(t)$ and $L(t)$.

5.2 Determination of the effective kinematic viscosity

In our experiment, we are able to measure $E_2(t)$ by using the tracer-line imaging technique and $L(t)$ via 2nd sound attenuation. To determine the effective kinematic viscosity v', we integrate equation (5.1) from t to infinity on both sides and write the total energy density $E(t)$ as

$$E(t) = B(\frac{\rho_s}{\rho})\kappa^2 L(t) + E_2(t) = v' \int_t^\infty \kappa^2 L^2(t')dt'. \tag{5.7}$$

Here $E_2(t)$ can be evaluated as $E_2(t) = \frac{3}{2}(\Delta u)^2$, assuming that the large-scale turbulence in decaying counterflow is isotropic. This assumption should hold reasonably well, at least at large decay times where the coupled flow shows a Kolmogorov spectrum for isotropic turbulence. As pointed out in Chapter 4, when the heater is turned off, the heat current decays to zero with a thermal time constant (typically less than 100 ms) and the time it takes to establish the coupling between two fluid components in our experiment is around 1-10 ms. Hence, t is selected to be at the large decay times (typically a few seconds), which are much greater than both the thermal time constant and the coupling time.

As presented in Chapter 4, Figure 5.1 summarizes our experimental observations in decaying counterflow at 1.65 K. For both heat fluxes, we observe $L(t) \propto t^{-3/2}$ and $\Delta u \propto t^{-1}$ at large decay times, which is in accordance with the decay of a quasiclassical turbulence with a Kolmogorov spectrum [74]. The total turbulence energy density E can be calculated based on our measured $L(t)$ and Δu by using the expression on the left-hand side of equation (5.7). the results for $q = 426$ mW/cm^2 and 150 mW/cm^2 are shown in Figure 5.2 as circles and triangles, respectively. For

both heat fluxes, the contribution from E_2 dominates. The solid curve and the dashed curve shown in Figure 5.2 are calculated based on the integral on the right-hand side of equation (5.7). To evaluate this integral, we assume that the $t^{-3/2}$ behavior of $L(t)$ continues for decay times beyond the maximum measurement time in our experiment (about 40 s). Due to the fast decay of $L(t)$, the contribution to the integral at very long decay times is negligible. We used a least square fitting method to determine ν' value by requiring that the energy densities calculated with the expressions on either side of equation (5.7) give the best agreement at large decay times. At 1.65 K, $\nu'/\kappa = 0.46$ is obtained.

We made similar measurements in decaying counterflow at other temperatures above 1 K. For a given initial heat flux at other temperatures, we selected two late decay times at which the measured vortex line density shows $t^{-3/2}$ behavior and collect 200 images for each. Adding more data points at late decay times would not significantly increase the accuracy of ν' value. The overall decay behavior of the vortex line density L(t) and the root mean square velocity fluctuation Δu is similar to that at 1.65 K. Figure 5.3 shows total turbulence energy density decay for q = 250 mW/cm^2 at 1.45 K and $q = 300$ mW/cm^2 at 1.85 K. The value of ν' can be evaluated based on the best agreement of the energy densities on either side of equation (5.7).
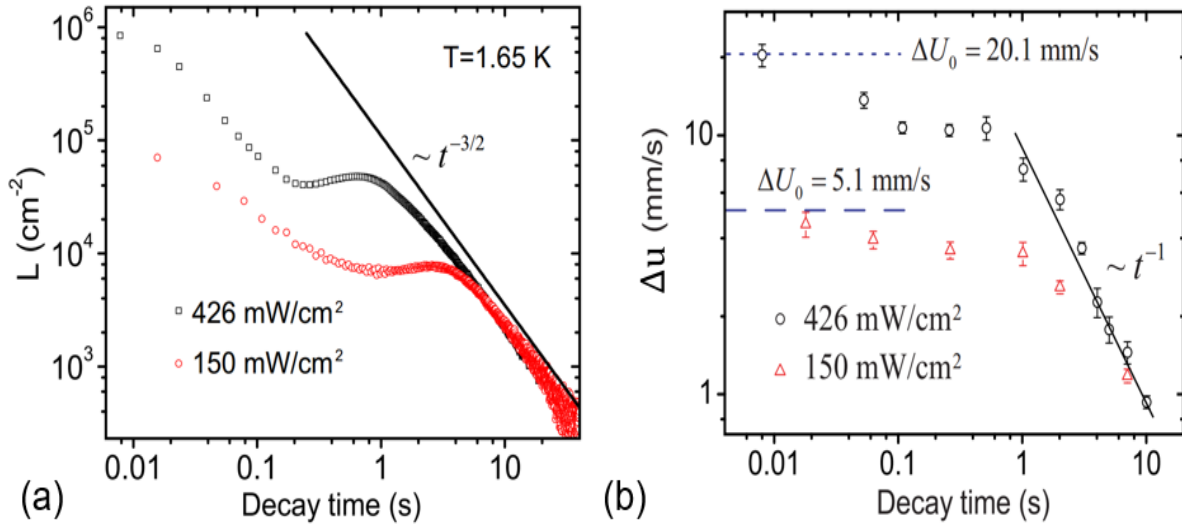
Figure 5.1 (a) The decay of the vortex line density $L(t)$ measured at different initial heat fluxes at 1.65 K. (b) Streamwise velocity fluctuation Δu determined from Gaussian fits of the velocity PDFs.
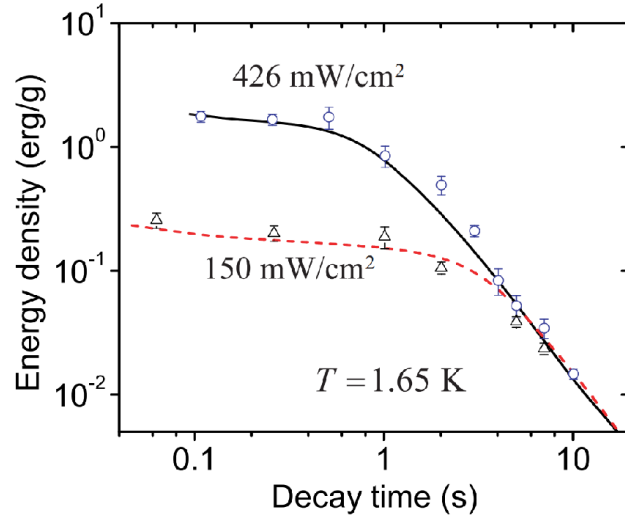
Figure 5.2 The decay of the total turbulence energy density in decaying counterflow turbulence at 1.65 K. The blue circles and black triangles were calculated based on the expression on the left-hand side of equation 5.7. The black solid curve and the red dashed curve represent the results calculated by using the integral on the right-hand side of equation 5.7. The best agreement of the calculated energy density at large decay times was achieved with $v' / \kappa = 0.46$.

(a)

(b)
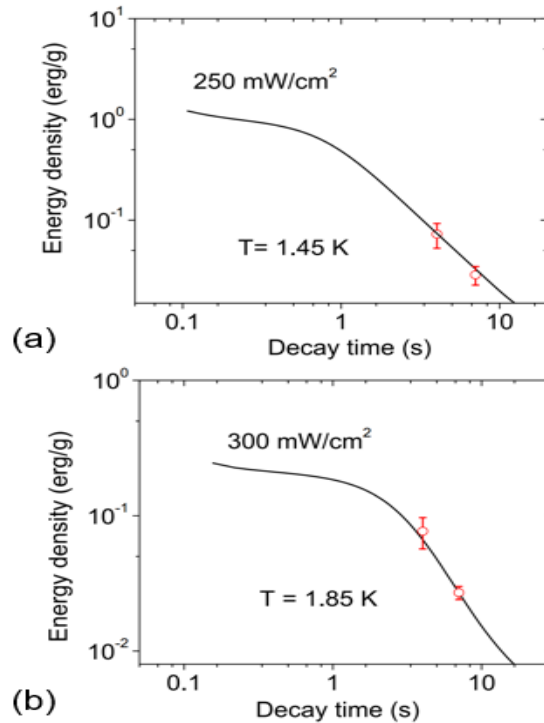
Figure 5.3 (a) The decay of the total turbulence energy density in decaying couterflow turbulence at 1.45 K. The steady state heat flux is 250 mW / cm^2 (b) The decay of the total turbulence energy density with initial heat flux 300 mW / cm^2 at 1.85 K.

67

In Figure 5.4, we show the effective kinematic viscosity ν' obtained at different temperatures (blue triangles). To aid our discussion, we also include in Figure 5.4 the kinematic viscosity ν' calculated with our vortex line density data by using equation (5.6) (black squares), the ν' values obtained by Stalp et al. in the towed grid experiment [90] (red solid circles), and the kinematic viscosity $\nu_n = \mu_n / \rho$ calculated based on the tabulated normal fluid viscosity μ_n [52] (black solid curve). It is clear ν_n that is smaller than ν', which reflects the fact that the dissipation processes in quasiclassical turbulence in He II include not only the normal fluid viscosity but also mutual friction. We note that the values determined by using our new methods appear to be greater than both the values calculated by using the tranditional method via equation (5.6) and those from Stalp et al. This difference may reflect the inherent limitations associated with the hypothesis involved in deriving the equation (5.6). Indeed, one can see clearly in Figure 4.6 (a) that the structure function at large decay times exhibits a peak at a scale smaller than the channel width, indicating the energy containing eddy size being smaller than D. The black squares in Figure 5.4 would appear much lower if a smaller energy-containing eddy size were used in the calculation.
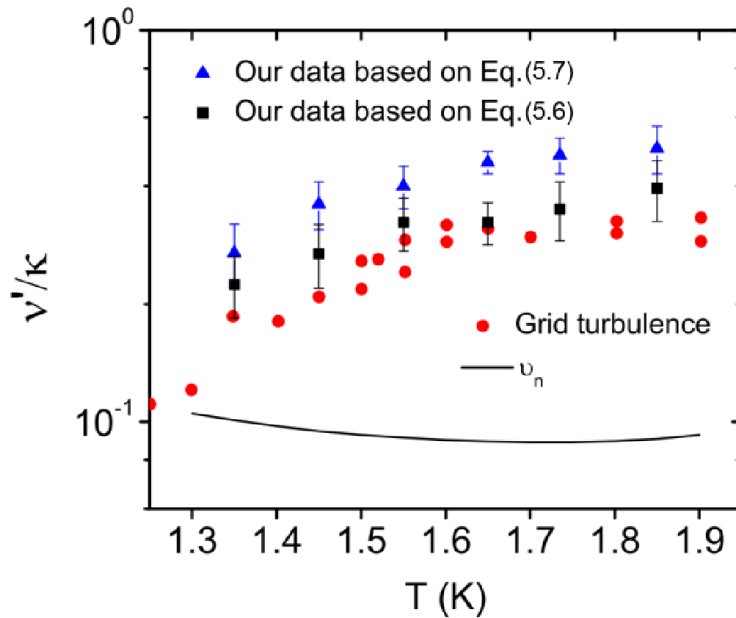
Figure 5.4 Effective kinematic viscosity in units of κ. The blue triangles represent values calculated by using our new method via equation (5.7). The black squares were calculated by using our vortex density data via equation (5.6). The red solid circles represent values obtained by Stalp et al. in the towed grid turbulence experiment [90] that were corrected by Chagovets et al. [92]. The black solid curve is the kinematic viscosity of He II calculated based on the normal fluid viscosity alone [52].

CHAPTER 6

DECAY OF GRID TURBULENCE

In this chapter, we present some preliminary experimental results on the study of the decay of grid turbulence in He II. The goal of this research is to investigate intermittency phenomenon in quantum turbulence generated by mechanical means (i.e. quasiclassical turbulence). Pioneering experiments on turbulent flows generated by two counter-rotating disks suggests that the intermittency is also present in superfluid turbulence [85]. However, this experiment was based on the local pressure fluctuations measurement. This method works only at temperatures where either the normal fluid component or the superfluid component is dominant. On the other hand, theoretical work by Boue et al. [94] suggests that intermittency is enhanced at temperatures when both fluids have comparable fraction. Using flow visualization technique, we are able to investigate intermittency behavior of towed-grid generated turbulence in He II.

6.1 Overview

He II is observed to behave very similarly to classical fluids when a turbulent flow is generated by a towed grid [74] or a rotating propeller [85]. Smith and co-workers [95] first studied the grid generated turbulence in He II by measuring the vortex line density decay via 2nd sound attenuation. The observed decay of the vortex line density from 1 s to 5 s shows $t^{-3/2}$ behavior, indicating quasiclassical turbulence. Later, Stalp et al. [74] improved the experimental technique and extended the decay measurement to around 20 s. They proposed a theoretical model for the decay of homogeneous and isotropic turbulence, which could describe the $L(t)$ data on the decay of grid turbulence as well as the decay of classical turbulence experiment. Their experimental and theoretical studies suggest a deep similarity between superfluid and classical turbulence.

Maurer and Tabeling [85] also investigated the analogies between superfluid and classical turbulence by measuring the energy spectrum of the turbulent flow driven by two counter-rotating disks below and above T_λ. They measured the local pressure fluctuations using a small total-head tube in the turbulent flow. By using Bernoulli theorem, they could estimate the local velocity fluctuations and hence determine the energy spectrum of the superfluid turbulence. The similar Kolmogorov energy spectrum was observed at three different temperatures, 2.3 K, 2.08 K and 1.4

K, which reveals a striking similarity between classical and superfluid turbulence. Their results first suggested that the intermittency is also present in superfluid turbulence. The 1941 theory of Kolmogorov [96] predicts, for high Reynolds number turbulent flow, in the inertial range of scales $\eta \ll r \ll L'$ (L' is the energy input scale and η is the viscous energy dissipation scale), the nth order structure function $S_n(r) \propto r^{\zeta_n^{K41}}$ with $\zeta_n^{K41} = n/3$. Past experiments in classical turbulence has shown that the measured scaling exponents $\zeta_n^{\exp} < \zeta_n^{K41}$ for $n > 3$ and this discrepancy increases with n [97-100]. This behavior is referred to as intermittency, which has attracted many experimental and theoretical efforts in classical turbulence research field [101,102].

Recently, Boue et al. [94] studied the intermittency behavior of superfluid turbulence in He II by using shell model simulations. They simulated the scaling behavior of the superfluid turbulence for different temperatures such that $\rho_n \gg \rho_s$, $\rho_s \approx \rho_n$ and $\rho_n \ll \rho_s$. They discovered that the scaling behavior of superfluid turbulence is practically the same as that in classical turbulence for $\rho_n \gg \rho_s$ and $\rho_n \ll \rho_s$. This behavior agrees with our expectation. When $\rho_n \gg \rho_s$, the portion of the superfluid component is so small that can be neglected and the statistics of superfluid turbulence becomes close to that of classical turbulence. Hence, the scaling exponents of superfluid turbulence and classical turbulence are similar. When $\rho_n \ll \rho_s$, in the absence of negligible viscosity and mutual friction, the kinetic energy in superfluid turbulence should cascade downscale without loss at large scales $R \gg l$. Therefore, one would expect to see similar inertial range behavior of superfluid turbulence and classical turbulence. However, in the range $0.25 \le \rho_n / \rho \le 0.5$, the simulated scaling exponent $\zeta_n^{sim} < \zeta_n^{\exp} < \zeta_n^{K41}$ for $n > 3$. That is to say, the scaling exponent deviates further from Kolmogorov's scaling law when the densities of the normal fluid and superfluid components are comparable and mutual friction becomes important. More recently, Shukla and Pandit extended Boue et al.'s work [103]. Their simulation work also showed the similar scaling exponents for the superfluid turbulence and the classical turbulence for $\rho_n / \rho \le 0.1$ and $\rho_n / \rho \ge 0.75$. Moreover, they found that, when $0.1 < \rho_n / \rho < 0.3$ and $0.4 < \rho_n / \rho < 0.65$, the simulated scaling exponent $\zeta_n^{sim} > \zeta_n^{K41}$. In the range $0.3 < \rho_n / \rho < 0.4$, $\zeta_n^{sim} \simeq \zeta_n^{K41}$. Their simulation results show a disagreement with theoretical prediction of Boue and co-workers [94].

Motivated by the predicted no-classical scaling exponent in the superfluid turbulence, we plan to investigate intermittency behavior of towed grid generated turbulence in He II. Recently, some preliminary experimental results have been obtained.

6.2 Experimental setup

A new grid towing system has been built for this experiment. Figure 6.1(a) is a schematic showing the experimental setup. A bellows with a 1.25 *cm* diameter stainless steel rod installed inside is mounted on the top of the cryostat. The extended and compressed length of the bellows are around 43 *cm* and 10 *cm*, respectively. One end of the rod goes into the helium bath and connects with a grid support structure made by four thin stainless steel wires that will not disturb the flow. The schematic of the grid used in our experiment is shown in Figure 6.1(b). The size of the grid is 9.2 *mm* $\times$ 9.2 *mm* and the thickness is about 0.6 *mm*. The mesh size is around 1.27 *mm*. The other end of the rod is attached to a cable that is linked to a computer controlled stepper motor. The motor provides the force to pull the grid at a constant velocity from the bottom to the top in the follow channel. The maximum grid speed we can achieve in our experiment is approximately 1 *m / s*. Thus, the grid can be towed by the stepper motor along the flow channel, which allows us to study the decay in the resulting turbulent flow.

Constant towing speed is very important in this experiment. The towing system was tested with dummy weights (~ 20 lbs.) prior to installation with the cryostat. We record the movement of the towing system with dummy weights via a video and then plot its position as a function of time, which is illustrated in Figure 6.2. One frame corresponds to 0.04 s. The movement is found to be almost linear and its deviation is negligible.

The experimental procedure for the decay of grid turbulence is similar to that used in counterflow turbulence measurement. In a typical tracer line imaging experiment, the grid is stopped at the top of the channel, and a baseline image is first collected in a static flow to be used as a reference. Then the grid is lowered to the bottom of the channel. After waiting for ~ 2 mins, the grid is pulled by the towing system through the visualization regime with a constant velocity. When the grid gets close to the top, we slow down and stop the grid. Time zero is set when the grid passes the position of the baseline. After a certain decay time, we send in femtosecond laser
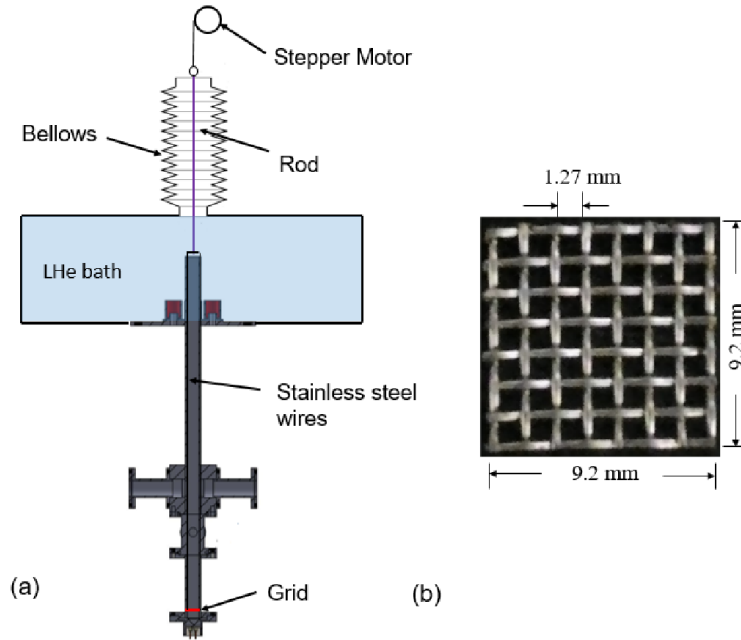
Figure 6.1 (a) A schematic showing the experimental setup for a towed grid turbulence. (b) The size of grid used in the experiment.
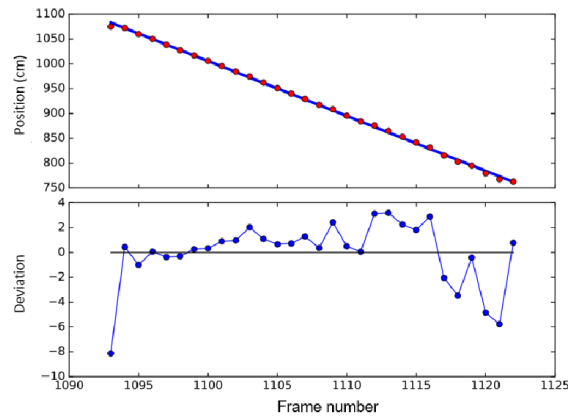
Figure 6.2 The observed movement of the towing system loaded by dummy weights. One frame corresponds to 0.04 s. The solid line on the top is a linear fit to the data. The bottom graph shows deviation of the observed position from the linear fit.

pulses to generate a tracer line which can be imaged by 905 nm imaging laser pulses. Figure 6.3 shows typical tracer line images obtained at different decay times with grid towing speed $V_g = 30$ cm/s at 1.65 K. The distortion of the tracer line becomes weaker with time, like in the decay of thermal counterflow experiment.
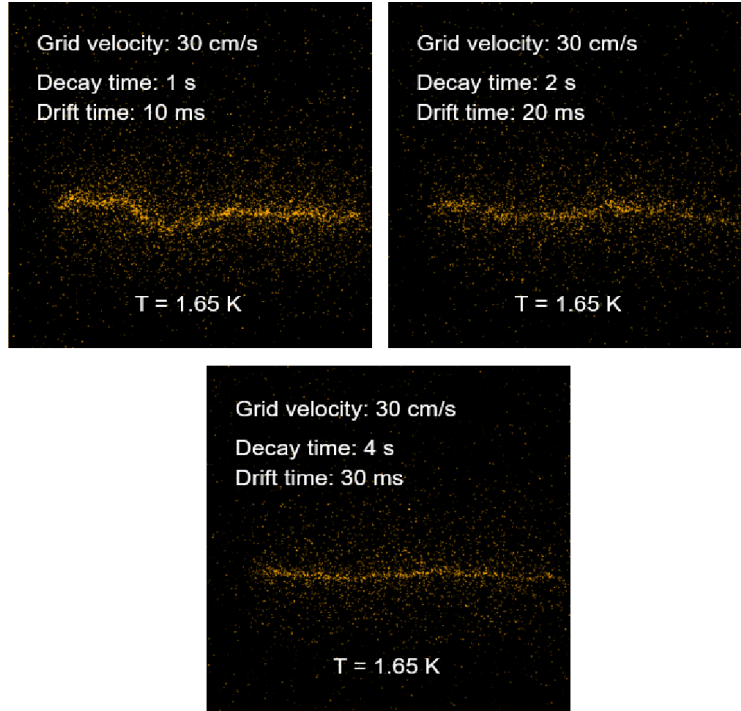
Figure 6.3 Typical tracer line images obtained at different decay times in the decay of grid turbulence at 1.65 K. The grid velocity is 30 cm/s.

Second sound attenuation method is also used to probe the vortex line density in the decay of grid turbulence. When the grid is stopped at the top of the channel, a complete resonance peak measurement is conducted to determine the unattenuated amplitude of the peak height $\overline{A_0}$ and width Δf_0 in equation (2.5). Then we lower the grid to the bottom of the channel and wait for ~ 2 mins. The second sound data acquisition is triggered when we start pulling the grid through the flow channel. Using the same method as implemented in the decay of thermal counterflow experiment (see Section 4.2.2), we can record resonance peak value $\overline{A}$ as a function of decay time. Subsequently, repeating the measurement 100 times allows us to suppress the noise in measuring the vortex line density.

6.3 Preliminary results

We first made flow visualization measurements in the decay of grid turbulence. The experiments were conducted at temperatures 1.45, 1.65, 1.85, 2.0 and 2.15 K. The grid was towed

at a velocity of $V_g = 30$ cm/s over roughly 15 cm. The typical drift time is 10 - 30 ms and over 100 single shot images are collected at decay times 1 s, 2 s and 4 s. Spatial profiles of the flow velocity can be obtained based on an ensemble average of 100 tracer line images. Figure 6.4 shows an example at 1.65 K (results are similar at other temperatures). A large mean flow is observed at 1 s decay time, which is most likely caused by the slight asymmetry of the grid support structure. At 4 s decay time, the spatial profile of the mean flow velocity is almost flat across the channel. The velocity fluctuation decreases as the decay time increases, and its profile becomes more or less flat at 2 s and 4 s decay times. The measured decay of Δu at different temperatures is shown in Figure 6.5. We observe that Δu is almost proportional to t^{-1}, which is consistent with the decay of a quasiclassical turbulence with a Kolmogorov spectrum [74].

We calculated the second order transverse structure to examine the energy spectrum in the decay of grid turbulence. The time evolution of the calculated $S_2^{\perp}(R,r)$ at 1.65 K is shown in Figure 6.6. We observe that, $S_2^{\perp}(R,r)$ in the decay of grid turbulence is qualitatively similar to the results obtained in the decaying counterflow experiment. The determined power index of $S_2^{\perp}(R,r)$ decreases as the decay time increases. Around 4 s into the decay, the observed $S_2^{\perp}(R,r)$ shows the classical Kolmogorov form ($n = 2/3$). The results at other temperatures are similar. Figure 6.7 shows the observed $S_2^{\perp}(R,r)$ for 4 s decay at other temperatures. The results all exhibit $r^{2/3}$ power law behavior (the black solid line), indicating a quasiclassical turbulence with a Kolmogorov energy spectrum [68].
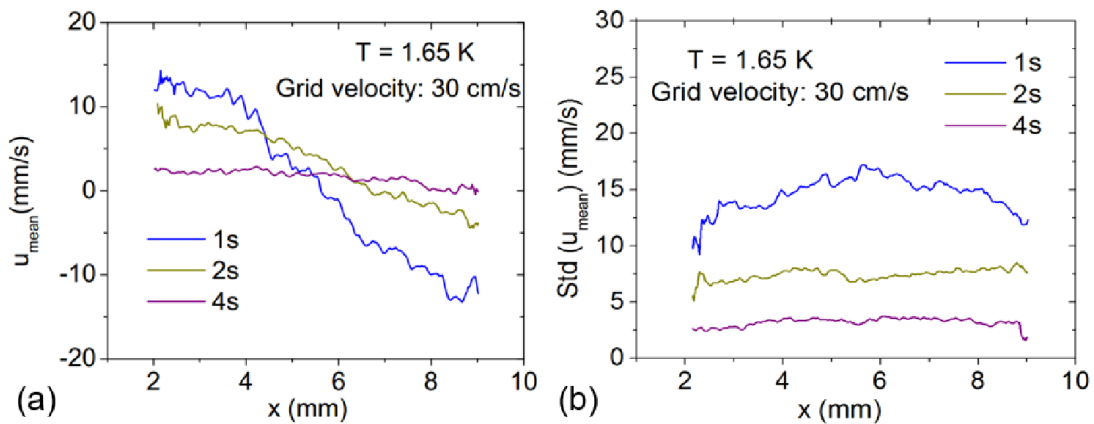
Figure 6.4 Spatial profile of the mean normal fluid velocity and turbulent fluctuations at decay times 1 s, 2 s and 4 s for 1.65 K, $V_g = 30$ cm/s.
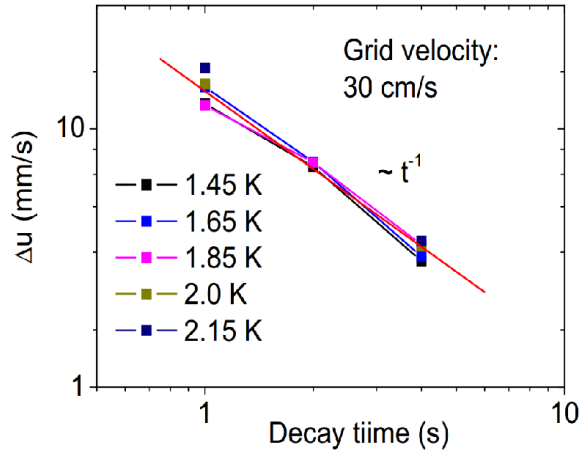
Figure 6.5 Streamwise velocity fluctuation as a function of decay time at temperatures 1.45, 1.65, 1.85, 2.0 and 2.15 K. The red solid line represents a power-law form of $\Delta u \propto t^{-1}$.
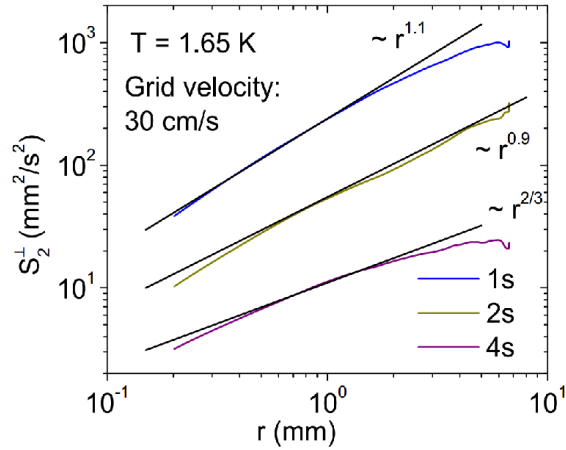
Figure 6.6 $S_2^{\perp}(R,r)$ at different decay times in the decay of grid turbulence at 1.65 K.

We also conducted a preliminary $L(t)$ measurement in the decay of grid turbulence. However, the grid is rather disruptive to the second sound measurement and the quality of the resonance peaks is not optimal. Accurate estimation of the resonance peak width and the background noise is very challenging. These uncertainties can affect the magnitude of the vortex line density. But the overall behavior of the observed $L(t)$ should be reliable. The decay of $L(t)$ at 1.65 K is shown in Figure 6.8. At large decay times, $L(t) \propto t^{-3/2}$, which agrees with Stalp et al.'s observation [74].
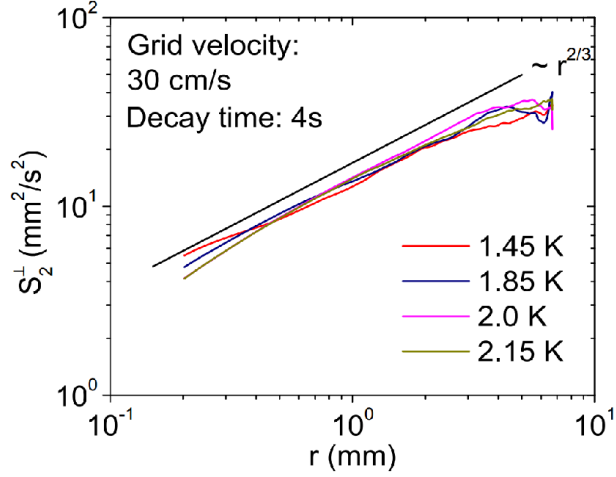
Figure 6.7 $S_2^\perp(R,r)$ for 4 s decay at temperatures 1.45, 1.85, 2.0 and 2.15 K.
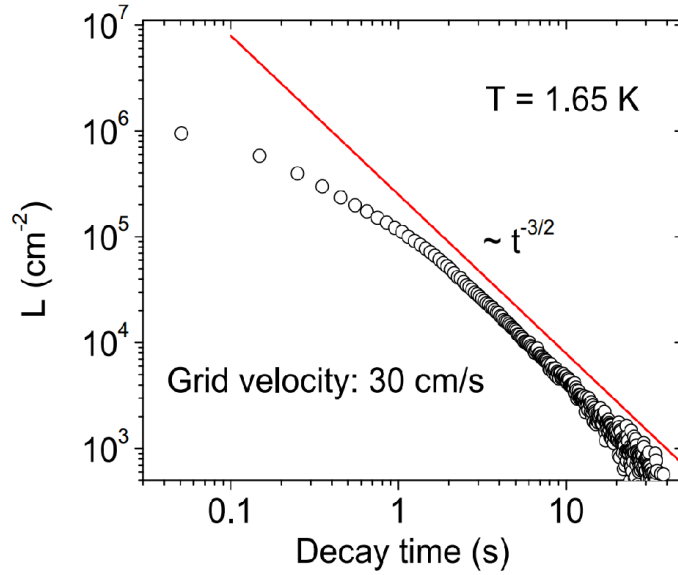
Figure 6.8 The decay of vortex line density $L(t)$ measured for $V_g = 30$ cm/s at 1.65 K.

6.4 Discussion

We have used our observations to investigate the intermittency behavior in superfluid turbulence. The visualization data at 4 s decay time is chosen because at this point both the observed $S_2^\perp(R,r)$ and measured $L(t)$ decay have indicated the quasiclassical behavior of He II. Following Benzie et al. [104], we use the extended self-similarity

$$S_n(r) = S_3(r)^{\zeta_n/\zeta_3^{K41}}. \tag{6.1}$$

Here ζ_n/ζ_3^{K41} could be determined by using a linear fit of log-log plot of equation (6.1). An example at 1.65 K is shown in Figure 6.9. The $S_1(r)$ is represented by the lowest curve and the exponent n (from 1 to 7) increases from the bottom to the top. The range between the two red dashed lines is selected to be fitted by a linear function. In our estimation, we set $\zeta_3^{K41} = 1$ and hence can determine ζ_n for each exponent n.

In order to see how ζ_n deviates from $\zeta_n^{K41} = n/3$, we plot $\zeta_n - n/3$ as a function of n at different temperatures (shown in Figure 6.10). The error bars are obtained from variation estimation of the linear regression parameters. As one can see, at 2.15 K when $\rho_n/\rho = 0.87$, $\zeta_n > \zeta_n^{K41}$ and $\zeta_n \simeq \zeta_n^{K41}$ at 2.0 K ($\rho_n/\rho = 0.55$). At other temperatures, our preliminary results show a clear deviation from Kolmogorov's scaling and the strongest deviation occurs at 1.85 K when $\rho_n/\rho = 0.36$. More systematic measurements are required to have a better understanding of the intermittency behavior of superfluid turbulence in He II, which is scheduled for the future.
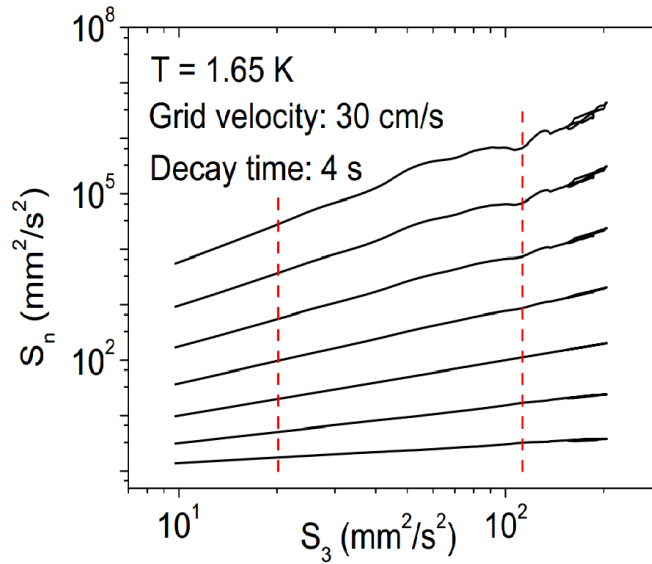
Figure 6.9 Illustration of the extended self-similarity at 1.65 K [103]. The $S_1(r)$ is represented by the lowest line and the n (from 1 to 7) increases from the bottom to the top. The range between the two red dashed lines is selected to be fitted by a linear function.
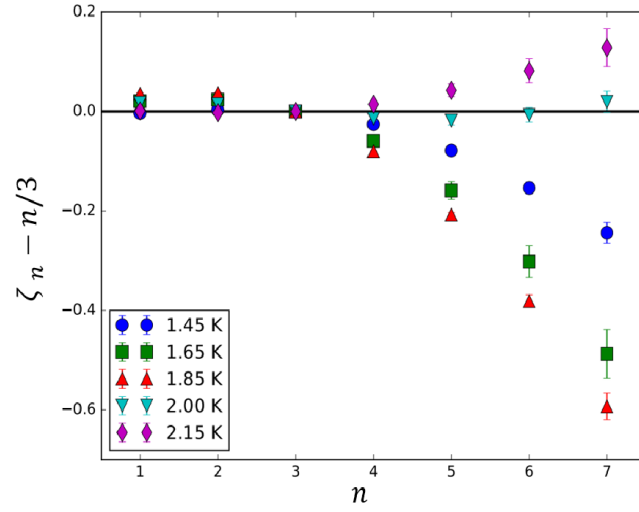
Figure 6.10 Deviation of the exponent of the nth order structure function ζ_n from the non-intermittent $n/3$ at different temperatures.

CHAPTER 7

CONCLUSIONS AND FUTURE WORK

7.1 Conclusions

This thesis mainly focuses on the visualization study of thermal counterflow turbulence in superfluid ^{4}He. 2nd sound attenuation measurement is also implemented to investigate the behavior of the vortex line density. Some preliminary experimental results of the towed turbulence are presented. Our study has revealed some interesting aspects of thermal counterflow turbulence in He II. The major findings of the present study are summarized below:

1. A novel flow visualization technique in He II based on the generation and imaging of thin lines of metastable He_2^* tracer molecules has been developed [29]. These molecular tracers are created via femtosecond-laser field ionization of helium atoms and can be imaged using a laser-induced fluorescence technique. That the tracer molecules can follow the motion of the normal fluid component has been confirmed in our experiment [30].

2. In steady state thermal counterflow, it has been observed that, at relatively small velocities, where the superfluid is already turbulent, the flow of the normal fluid remains laminar, but with a distorted velocity profile, while at a higher velocity there is a transition to turbulence [31]. Our suspicion is that the quantized vortices could accumulate near the channel wall in that heat flux regime, and therefore more strongly affect the tail part of the tracer line.

3. The observed turbulence intensity of the normal fluid component in steady state thermal counterflow is much larger than that observed in classical turbulent channel flow. This intriguing large turbulence intensity appears to be weakly dependent on velocity and primarily controlled by the temperature [30].

4. The form of the second order transverse structure function of the normal fluid turbulence in steady state thermal counterflow differs from that found in classical turbulence [31]. The results of our systematic visualization studies suggest that the energy spectrum of the normal

fluid turbulence deviates more strongly from the classical form as the heat flux increases (See Figure 3.18).

5.   With the aid of our flow visualization, we have elucidated that the energy spectrum transition of the normal fluid turbulence in the decay of He II counterflow is responsible for the observed complex L(t) behavior. A theoretical model regarding the vortex line density decay has been developed, which accounts well for the experimental observations [33].

6.   Combing the recently developed flow visualization technique and second sound attenuation, we have been able to measure the effective kinematic viscosity for the decay of quasiclassical turbulence in He II in a wide temperature range [32].

7.2 Future work

As described in Chapter 6, we obtained some preliminary experimental results on the decay of grid turbulence in He II and studied the intermittency behavior of superfluid turbulence. However, only one grid towing velocity and three different decay times are tested. In order to carefully study the intermittent behavior, systematic measurements of the flow visualization at different grid velocities at various decay times are needed in the future. At the meanwhile, a more reliable second sound attenuation measurement will allow us to determine the effective kinematic viscosity for decaying grid turbulence.

Besides, our current understanding about the energy spectrum of normal fluid turbulence is based on the calculation of second order transverse structure function. In turbulence research, it is often desirable to have the capability of measuring not only the transverse structure functions but also the longitudinal structure functions. To determine the longitudinal structure functions, we then need to make simultaneous velocity measurements at two locations aligned along the streamwise direction. This can be done with a setup shown schematically in Figure 7.1. The output of the femtosecond laser can be divided into two beams using a beam splitter. The two beams are then focused into the flow channel to create two parallel lines of He_2^* tracers. One of the two beams is reflected on a mirror mounted on a translation stage such that the separation r between the two beams can be continuously adjusted. The two tracer lines produced in the channel can be followed and imaged simultaneously. Based on the displacements of the two tracer lines, one can then

correlate the velocities along the stream direction and calculate the velocities along the streamwise direction and calculate the longitudinal structure functions as $S_n^{\parallel} = \overline{\left(u_1 - u_2\right)^n}$ (see Figure 7.1).

Indeed, this optical setup allows the determination of both longitudinal and transverse structure functions for displacements in the direction of the mean flow. It is worthwhile to note that since the maximum output pulsed energy of our femtosecond laser system is 4 mJ, much greater than the energy needed to ionize helium atoms (slightly below 60 μJ), the laser beam can be divided into multiple beams to create more complicated tracer-line patterns such as multiple parallel lines, crosses, or grid structures. Quantitative measurement of the vorticity field and complex flow field parameters can be made possible.
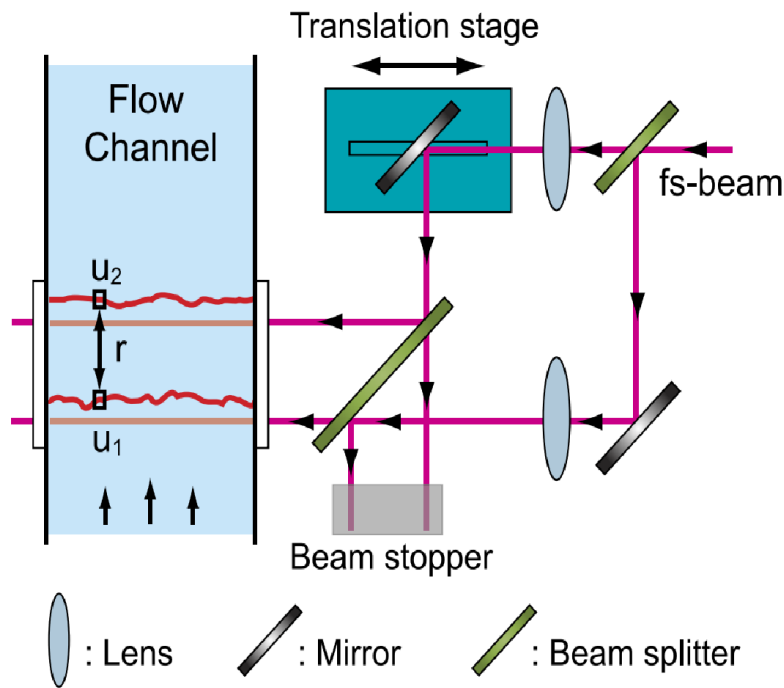
Figure 7.1 A Schematic diagram showing the optical setup for generating two parallel He_2^* tracer lines in a flow channel.

REFERENCES

[1] D. van Delft, Physics Today 61, 36–42 (2008).

[2] W. Keesom and J. van den Ende, Proceedings Koninklijke Akademie van Wetenschappen te Amsterdam 33, 243–254 (1930).

[3] J. McLennan, et al., Philosophical Magazine 14, 161–167 (1932).

[4] F. London, Phys. Rev. 54, 947–954 (1938).

[5] L. Tisza Comptes rendus hebdomadaires des sances de l'Acadmie des Sciences 207, 1186–1189 (1938).

[6] S. Balibar, J. Low Temp. Phys. 146, 441–470 (2007).

[7] S. W. Van Sciver. Helium cryogenics. Springer, New York:USA, 2nd edition, 2012.

[8] M.F. Kessler, et al., Astron Astrophys, 315, L27-L31 (1996).

[9] D.R. Tilley and J. Tilley, Superfluidity and Superconductivity (1986).

[10] D. V. Osborne, Proc. Phys. Soc. A63, 909 (1950).

[11] R. P. Feynman, Progress in Low Temperature Physics vol. 1, ed. C. J. Gorter (1955).

[12] W.F. Vinen, Proc. R. Soc. Lond. A 243, 400 (1958).

[13] W. F. Vinen, Proc. R. Soc. Lond. A 240, 114 (1957). W. F. Vinen, Proc. R. Soc. Lond. A 240, 128 (1957). W. F. Vinen, Proc. R. Soc. Lond. A 242, 493 (1957).

[14] L. D. Landau and E. M. Lifshitz, Fluid Mechanics (Pergamon Press, Oxford, UK, 1987).

[15] W. Guo, et al., Phys. Rev. Lett., 105, 045301 (2010).

[16] L. Skrbek, et al., Phys.: Condens. Matter, 11, 7761 (1999).

[17] W.F. Vinen and J.J. Niemela, J. Low Temp. Phys., 126, 167-231 (2002).

[18] L. Skrbek and K. R. Sreenivasan, Phys. Fluids24, 011301 (2012).

[19] W. Guo, et al., Proc. Natl. Acad. Sci., 111, 4653 (2014).

[20] M. E. Hayden et al., Phys. Rev. Lett. 93, 105302 (2004).

[21] Guo W, et al., Phys Rev B 79(5):054515 (2009).

[22] S.W. Van Sciver, et al., J. Low Temp. Phys. 148, 225-233 (2007).

[23] T. Zhang and S.W. Van Sciver, Nat. Phys. 1, 36-38 (2005).

[24] G.P. Bewley, et al., Nature, 441, 588 (2006).

[25] M.S. Paoletti, et al., J. Phys. Soc. Jap. 77, 111007 (2008).

[26] Chagovets TV and S.W. Van Sciver, Phys Fluids 23(10):107102 (2011).

[27] M. La Mantia and L. Skrbek, EPL 106, 46002 (2014).

[28] M. La Mantia and L. Skrbek, Phys. Rev. B 90, 014519 (2014).

[29] J. Gao, et al., Rev. Sci. Instrum. 86, 093904 (2015).

[30] J. Gao, et al., J. Low Temp. Phys., (2016).

[31] A. Marakov, et al., Phys. Rev. B 91, 094503 (2015).

[32] J. Gao, et al., Phys. Rev. B 94, 094502 (2016).

[33] J. Gao, et al., JETP Letters, 103, 732 (2016).

[34] W.S. Dennis, et al., Phys. Rev. Lett. 23, 1083 (1969).

[35] J.C. Hill, et al., Phys. Rev. Lett. 26, 1213 (1971).

[36] A. V. Benderskii, et al., J. Chem. Phys. 110, 1542 (1999).

[37] P. C. Hill, Phys. Rev. A 40, 5006 (1989).

[38] D.N. McKinsey, et al., Phys. Rev. A 59, 200 (1999).

[39] A.V. Benderskii, et al., J. Chem. Phys. 117, 2101 (2002).

[40] Y. A. Sergeev and C. F. Barenghi, J. Low Temp. Physics 157, 429 (2009).

[41] D.E. Zmeev, et al., Phys. Rev. Lett., 110, 175303 (2013).

[42] D.N. McKinsey, et al. , Phys. Rev. Lett. 95, 111101 (2005).

[43] W. G. Rellergert, et al., Phys. Rev. Lett. 100, 025301 (2008).

[44] W.G. Rellergert, Ph.D. thesis, Yale University (2008).

[45] SPFIRE ACE-35F system from Spectra Physics Company. Specifications can be found online (http://www. Spectra-physics.com/products/ultrafast-lasers/).

[46] S. A. Self, Appl. Opt. 22, 658 (1983).

[47] Lasers and laser-related equipment. Test methods for laser beam widths, divergence angles and beam propagation ratios, ISO 11146-2:2005 (E) (accessed May 24, 2014).

[48] J.W. Keto, et al., Phys Rev A 10, 872-886 (1974).

[49] L.S. Challis and R. A. Sherlock, J. Phys. C 3, 1193 (1970).

[50] A. Noullez, et al., 339, 287–304 (1997).

[51] S. Babuin, et al., Phys. Rev. B 86, 134515 (2012).

[52] R. J. Donnelly and C. F. Barenghi1, J. Phys. Chem. Ref. Data 27,1217(1998).

[53] KW Schwarz, Phys. Rev. B 38, 2398 (1988).

[54] K. P. Martin and J. T. Tough, Phys. Rev. B 27, 2788 (1983).

[55] P. E. Dimotakis and J. E. Broadwell, Phys. Fluids 16, 1787 (1973).

[56] C. E. Chase, Phys. Rev. 127, 361 (1962).

[57] D. F. Brewer and D. O. Edwards, Proc. R. Soc. London Ser. A 251, 247 (1959); Philos. Mag. 6, 775 (1961); 6, 1173 (1961); 7, 721 (1962); J. Low Temp. Phys. 43, 327 (1981).

[58] V. P. Peshkov, et al., 41, 1427 (1961) [Sov. Phys. — JETP 14, 1019 (1962)].

[59] K.W. Schwarz, Phys. Rev. B 38, 2398 (1988).

[60] D. J. Melotte and C. F. Barenghi, Phys. Rev. Lett. 80, 4181 (1998).

[61] M. Spiga and G. L. Morino, Int. Comm. Heat Mass Transfer. 21,469(1994).

[62] R. G. K. M. Aarts and A. T. A. M. de Waele, Phys. Rev. B 50, 10069 (1994).

[63] A. W. Baggaley and S. Laizet, Phys. Fluids 25, 115101 (2013).

[64] S. Yui and M. Tsubota, Phys. Rev. B 91, 184504 (2015).

[65] D. Khomenko, et al., J. Low Temp. Phys., (2016).

[66] L. Galantucci, et al., Phys. Rev. B 92, 174530 (2015).

[67] P. A. Davidson, Turbulence: An Introduction for Scientists and Engineers (Oxford University Press, United Kingdom, 2004).

[68] U. Frisch, Turbulence (Cambridge University Press, 1995).

[69] W. F. Vinen, J. Low Temp. Phys. 175, 305 (2014).

[70] D. Khomenko, et al., Phys. Rev. B 93, 014516 (2016).

[71] K. W. Schwarz and J. R. Rozen, Phys. Rev. Lett. 66, 1898 (1991).

[72] K. W. Schwarz and J. R. Rozen, Phys. Rev. B44, 7563 (1991).

[73] L. Skrbek, et al., Phys. Rev. E67, 047302 (2003).

[74] S. R. Stalp, et al., Phys. Rev. Lett.82, 4831 (1999).

[75] W. F. Vinen, Phys. Rev. B 61,1410 (2000).

[76] C. F. Barenghi, et al., Phys. Fluids9,2631(1997).

[77] A. W. Baggaley, et al., Europhys. Lett.98, 26002 (2012).

[78] C. F. Barenghi and L. Skrbek, J. Low Temp. Phys., 146, 5 (2007).

[79] C. F. Barenghi, et al., Phys. Rev. E74, 026309 (2006).

[80] O. Henze, Turbulence, 2nd ed. (McGraw-Hill, New York, 1975).

[81] R. J. Donnelly, Quantized Vortices in Helium II (Cambridge University Press, Cambridge, 1991).

[82] C. E. Leith, Phys. Fluids 10, 1409 (1967).

[83] L. Boue, et al., Phys. Rev. B91, 144501 (2015).

[84] A. V. Gordeev, et al., J. Low Temp. Phys. 138, 649 (2005).

[85] J. Maurer and P. Tabeling, Europhys. Lett.43,29(1998)

[86] L. Skrbek, et al., J. Phys.: Condens. Matter 11,7761(1999).

[87] B. Saint-Michel, et al., Phys. Fluids26, 125109 (2014).

[88] M.V. Zagarola and A.J. Smits, Phys. Rev. Lett., **78**, 239-242 (1997).

[89] C. Baudet, P. Bonnay, et al., 14th European Turbulence Conference, 1–4 Sept. (2013).

[90] S. R. Stalp, et al., Phys. Fluids14,1377(2002).

[91] J. J. Niemela, et al., J. Low Temp. Phys.138,537(2005).

[92] T. V. Chagovets, et al., Phys.Rev.E76, 027301(2007).

[93] S. Babuin, et al., Phys. Rev. B 92, 184503(2015).

[94] L. Boue, et al., Phys. Rev. Lett. 110, 014502 (2013).

[95] M. R. Smith, et al., Phys. Rev. Lett.71, 2583 (1993).

[96] A. N. Kolmogorov, Dokl. Akad. Nauk. SSSR32, 16 (1941).

[97] F. Anselmet, et al., J. Fluid Mech.140, 63–89 (1984)

[98] J. Maurer, et al., Europhys. Lett.26, 31–36 (1994)

[99] A. Arneodo, et al., Europhys. Lett.34, 411–416 (1996)

[100] K.R. Sreenivasan and R.A. Antonia, Annu. Rev. Fluid Mech.29, 435–472 (1997)

[101] K.R. Sreenivasan and B. Dhruva, Prog. Theor. Phys. Suppl.130, 103–120 (1998)

[102] V. L'vov and I. Procaccia, Phys. World9, 35–40 (1996)

[103] V. Shukla and R. Pandit, Phys. Rev. E 94, 043101 (2016)

[104] R. Benzi, et al., Phys. Rev. E 48 (1), R29–R32 (1993)

BIOGRAPHICAL SKETCH

Jian Gao grew up in Wangjiang, China where he graduated high school in 2008. He earned his Bachelor's degree in Engineering Mechanics from Hohai University in 2012. After that, he joined Florida State University in Fall 2012 to purse his Ph.D. degree. His Ph.D. research, conducted in Cryogenics Research Group at National High Magnetic Field Laboratory, mainly focuses on visualization study of thermal counterflow turbulence in superfluid ^{4}He.

Publications

1. **J. Gao,** W. Guo, W.F. Vinen, S. Yui and M. Tsubota, "Dissipation in quantum turbulence in superfluid 4He", submitted to Phys. Rev. B., (2017)

2. **J. Gao**, E. Varga, W. Guo, and W.F. Vinen, "Statistical measurement of counterflow turbulence in superfluid helium-4 using He$_2$ tracer-line tracing technique", J. Low Temp. Phys., (2016)

3. **J. Gao**, W. Guo and W.F. Vinen, "Determination of the effective kinematic viscosity for the decay of quasiclassical turbulence in superfluid 4He", Phys. Rev. B 94, 094502 (2016)

4. **J. Gao**, W. Guo, V.S. L'vov, A. Pomyalov, L. Skrbek, E. Varga and W.F. Vinen, "The decay of counterflow turbulence in superfluid 4He", JETP Letters, 103, 732 (2016)

5. **J. Gao,** A. Marakov, W. Guo, B.T. Pawlowski, S.W. Van Sciver, G.G. Ihas, D.N. Mckinsey and W.F. Vinen, "Producing and Imaging a Thin Line of He2 Tracer Molecules in Helium-4", Rev. Sci. Instrum, 86, 093904 (2015)

6. A. Marakov, **J. Gao,** W. Guo, B.T. Pawlowski, S.W. Van Sciver, G.G. Ihas, D.N. Mckinsey and W.F. Vinen, "Visualization of the normal fluid turbulence in counterflowing superfluid 4He", Phys. Rev. B 91, 094503 (2015)